

Carnegie Mellon University

CARNEGIE INSTITUTE OF TECHNOLOGY

THESIS

SUBMITTED IN PARTIAL FULFILLMENT OF THE REQUIREMENTS

FOR THE DEGREE OF Doctor of Philosophy

TITLE Determination of Charge Concentration in Surfactant-Doped
Nonpolar Liquids

PRESENTED BY Benjamin Yezer

ACCEPTED BY THE DEPARTMENT OF

Chemical Engineering

DENNIS PRIEVE	4/15/16
_____ DENNIS PRIEVE, CO-ADVISOR	_____ DATE
PAUL SIDES	4/15/16
_____ PAUL SIDES, CO-ADVISOR	_____ DATE
ADITYA KHAIR	4/15/16
_____ ADITYA KHAIR, CO-ADVISOR	_____ DATE
LORENZ BIEGLER	4/15/16
_____ LORENZ BIEGLER, DEPARTMENT HEAD	_____ DATE

APPROVED BY THE COLLEGE COUNCIL

VIJAYAKUMAR BHAGAVATULA	4/15/16
_____ DEAN	_____ DATE

**Determination of Charge Concentration in Surfactant-Doped
Nonpolar Liquids**

Submitted in partial fulfillment of the requirements for

the degree of

Doctor of Philosophy

in

Chemical Engineering

Benjamin A. Yezer

B.S., Chemical Engineering, University of Rochester

Carnegie Mellon University
Pittsburgh, PA

May, 2016

ACKNOWLEDGEMENTS

I would like to express my sincere thanks and gratitude to by advisors Aditya Khair, Dennis Prieve, and Paul Sides for their invaluable insights, guidance, and support throughout my four years and nine months at Carnegie Mellon University. Their continued interest and engagement in my work helped me to become a more creative, thoughtful, and knowledgeable researcher. Their ability to share their individual expertise in a respectful and cooperative manner profoundly influenced my research in a positive manner.

I would also like to thank the members of my thesis committee – Bob Tilton, Jim Schneider, and Sara Majetich -for thoughtful comments, critiques, and suggestions. In particular, Jim Schneider's participation in many research discussions and sharing his knowledge of surfactant chemistry was instrumental to many aspects of my work. I am especially grateful to Jim Schneider for collaborating with my advisors me on several master's and undergraduate projects.

I gratefully acknowledge financial support for my thesis from the Dow Chemical Company. I especially want to thank Ben Freireich, Karl Jacob and Adam Grzesiak for their input and thoughtful monthly discussions.

My time at Carnegie Mellon was particularly enjoyable thanks to a great group of friends and coworkers. I thank all the members of the Khair, Sides, and

Prieve research groups that I have overlapped with: Chris Wirth, Reza Rock, Gang Xu, Stephanie Malone, Keyi Xu, Yuan Fang, Sixue Cheng, Xiaoyu Liang, Emily Carvalho, Michelle Smyk, Daniel Hong, Ridge Walker, Xi Chen, Denise Dowling, Sarah Feicht, Javier Lanauze, Rob Stout, Nick Chisholm, Toni Bechtel, and Alex Frankel. I thank the other complex fluids engineering faculty students that participated in our monthly discussions in our studies of nonpolar liquids including Lynn Walker, Shelley Anna, James Schneider, Blake Bleier, Chris Nelson, and Sharon Vuong. I also thank Stephen Spagnol, John Goldman, Pat Boyer, and John Riley for sharing many laughs over the years.

A special thanks goes to my family, especially Renee Raffini, Mark Whipple, Tony Yezer, Caroline Yezer, Claire Yezer, and Stefano deFeo for all of their support over the years. Your encouragement and faith in me helped me get through the highs and lows of graduate school. Thanks also goes to my father and mother-in-law Tony and Lorraine DeFilippo. Their sincere kindness and generosity made my time in Pittsburgh a wonderful experience. I will be forever grateful to all of you.

The last, but certainly not the least, thanks goes to my lovely wife Andrea. With her, I can always find joy and happiness no matter the situation. I know that in the future we will look back on my time at CMU with fond memories.

ABSTRACT

The technique of impedance spectroscopy was used in a thin cell (10 μm) to infer conductivity, permittivity and the differential double-layer capacitance of solutions of dodecane doped with oil soluble commercial surfactants. Solutions of OLOA 11000[®] [poly(isobutylene succinimide)] in dodecane were fit to an equivalent circuit model having four elements including a constant-phase element representing the double-layer capacitance. Using Gouy-Chapman theory for small zeta potentials and assuming univalent charge carriers, the double-layer capacitances were converted into charge carrier concentration. The impedance of dodecane doped with sorbitan trioleate (Span 85[®]), sorbitan monooleate (Span 80[®]) and sorbitan monolaurate (Span 20[®]) was also measured in a thin cell. Nyquist plots of all three surfactants showed the high frequency semicircle characteristic of parallel resistance and capacitance but often exhibited a second semicircle at low frequencies which was attributed to charge adsorption and desorption. The adsorption rate constants were independent of surfactant concentration while the desorption rate constants were proportional to the surfactant concentration.

The surfactants AOT[®], OLOA 11000[®], Span 85[®], Span 80[®], and Span 20[®] all increased the conductivity of dodecane. Phase analysis light scattering was used to find the hydrodynamic diameter of the micelles formed by the surfactants. For each surfactant the measured conductivity increased linearly with

concentration above the critical micelle concentration (CMC). The molar conductivity of the different surfactants increased exponentially with the estimated diameter of the polar core of the surfactants.

An apparatus and a method for determining the zeta potential of planar solids in contact with nonpolar liquids are described and values of the zeta potential are provided. The motor rotated the disk-shaped sample at several thousand rpm. A glassy carbon electrode with a circular exposed end was near the sample at its axis and a second glassy carbon electrode was far from the sample. Rotating the sample generated streaming potential as measured by an electrometer. The zeta potential of ITO coated glass was shown to have a magnitude smaller than 25 mV in solutions of OLOA 11000[®] in dodecane. The measured zeta potential of ITO justifies the assumption of small zeta potentials made in the theory used to fit the impedance data.

TABLE OF CONTENTS

ACKNOWLEDGEMENTS.....	ii
ABSTRACT.....	iv
TABLE OF CONTENTS.....	vi
LIST OF TABLES	ix
LIST OF FIGURES	x

CHAPTER 1 INTRODUCTION AND BACKGROUND TO NONPOLAR LIQUIDS..... 1

1.1 Introduction.....	1
1.2 References	10

CHAPTER 2 USE OF IMPEDANCE SPECTROSCOPY TO DETERMINE DOUBLE-LAYER CAPACITANCE IN DOPED NONPOLAR LIQUIDS . 14

2.1 Introduction.....	14
2.2 Materials and methods	18
2.3 Theory	21
2.3.1 Primitive 2-Element Circuit Model	21
2.3.2 5-Element Circuit Model.....	25
2.3.3 Constant-Phase Element Model	28
2.3.4 Determination of the equivalent circuit parameters.....	29
2.3.5 5-Element Circuit	30
2.3.6 Circuit with CPE	31
2.4 Results	33
2.4.1. Linearity of the response	33
2.4.2 Determination of equivalent circuit elements.....	37
2.4.3 The effect of varying concentration	42
2.4.4 Fluid properties found from equivalent circuit elements.....	43
2.5 Discussion.....	50
2.5.1 The CPE Model.....	53
2.5.2 EIS and a thin cell	56
2.5.3 The time constants of a polarized cell	57
2.6 Conclusions	57
2.7 Acknowledgement	58
2.8 References	58

CHAPTER 3 DETERMINATION OF CHARGE CARRIER CONCENTRATION IN DOPED NONPOLAR LIQUIDS BY IMPEDANCE SPECTROSCOPY IN THE PRESENCE OF CHARGE ADSORPTION 62

3.1 Introduction.....	62
3.2 Theory	65
3.2.1 Transport Model	66
3.2.2 The Equivalent Circuit Model	72
3.2.3 Constant Phase Elements.....	76
3.3 Materials and Methods.....	78
3.4 Results and Discussion.....	79
3.4.1 Contrasting spectra of OLOA 11000® and Span 80® in Dodecane	79
3.4.2 EIS spectra and adsorption	81
3.4.3 Impedance spectra of Span 85	90
3.4.4 Complications in thin cell EIS with adsorption	91
3.4.5 Conductivities.....	97
3.4.6 Debye lengths, charge concentrations, diffusion coefficients	99
3.4.7 Adsorption and desorption parameters	104
3.4.8. Implications for the origin of charge in solutions involving Span surfactants	107
3.4.9 Comparison to a potentiostatic experiment	109
3.5 Conclusions	111
3.6 Acknowledgement	113
3.7 References	113
3.8 Appendix: A physical circumstance leading to a CPE.....	116

CHAPTER 4 INCREASE IN CONDUCTIVITY WITH MICELLE SIZE OF SURFACTANT SOLUTIONS IN DODECANE 118

4.1 Introduction.....	118
4.2 Theory	119
4.3 Materials and Methods.....	121
4.3.1 Solution Preparation- Common Oil Soluble Surfactants	121
4.3.2 Phase analysis light scattering	122
4.3.3 Impedance spectroscopy.....	122
4.3.4 Less common nonionic surfactants	123
4.3.4 Nonaqueous Conductivity Meter.....	123
4.4 Results and Discussion.....	123
4.4.1 Light Scattering of Micelles	123
4.4.2 Conductivity of Surfactants in Dodecane	126
4.4.3 Ionic Strength	128
4.4.4 Molar Conductivity and Micelle Size.....	129
4.4.5 Charge Concentration and Micelle Size	132
4.4.6 Results from Tergitol NP-4® and Triton X-15®	134
4.5 Conclusions	137
4.6 Acknowledgement	139
4.7 References	139

CHAPTER 5 DETERMINATION OF THE ZETA POTENTIAL OF PLANAR SOLIDS IN NONPOLAR LIQUIDS 142

5.1 Introduction.....	142
5.1.1 Charge on solids in nonpolar media	143
5.1.2 The rotating disk.....	145
5.1.3 Application to nonpolar liquids	147
5.2 Experiments.....	148
5.2.1 Apparatus	148
5.2.2 Materials.....	149
5.2.3 Method	149
5.2.4. Electrophoretic mobility measurements	150
5.3 Results	150
5.3.1 Glassy carbon sensors	150
5.3.2 Substitution of an electrometer for the nanovoltmeter	154
5.3.3 Effect of rotation rate	156
5.3.4 Effect of sensor location.....	157
5.3.5 Adsorption of oppositely charged particles	159
5.4 Discussion.....	160
5.4.1 The streaming potential	161
5.4.2 The shape of the signal	163
5.4.3 Zeta potential of silica particles and fused silica	167
5.4.4 Zeta potentials of tested samples and surfactants	169
5.5 Conclusions	171
5.6 Acknowledgement	172
5.7 References	172
 CHAPTER 6 CONCLUSIONS AND FUTURE DIRECTIONS	 175
6.1 Conclusions	175
6.2 References	180

LIST OF TABLES

Table 1.1 Common commercial surfactants used in nonpolar liquids	9
Table 3.1. Comparison of best fit parameters from three different models.	86
Table 4.1. Results from phase analysis light scattering of micelles in dodecane	126
Table 4.2. Molar Conductivity and Charge Carriers per surfactant molecule	130
Table 5.1. Zeta potential of ITO coated glass surface in dodecane doped with different surfactants	171

LIST OF FIGURES

Figure 2.1. Schematic of the fluid cell.	20
Figure 2.2. Two electronic circuit analogs used to model the EIS response.	24
Figure 2.3. Waveforms of current (red) and potential (black) with 5% OLOA 11000 [®] in dodecane at 1 Hz.	35
Figure 2.4. Bode plots of the real (a) and imaginary (b) parts of the impedance obtained for a sample of 0.1% weight OLOA 11000 [®] in dodecane at potential amplitudes ranging from 10 mV to 1 V rms.	36
Figure 2.5. Impedance spectra for 10wt% OLOA 11000(a) and for 0.1wt% OLOA 11000 [®] (b).	38
Figure 2.6. Nyquist plot of impedance spectra for 0.1wt% OLOA 11000.	40
Figure 2.7. Phase angles calculated from 0.1wt% experimental data	41
Figure 2.8. Bode plots of (a) the real part and (b) the frequency times the imaginary part of the impedance at various concentrations of OLOA 11000 [®] in dodecane.	42
Figure 2.9. The conductivity of OLOA 11000 [®] in dodecane.	44
Figure 2.10. The dielectric constant of OLOA 11000 [®] in dodecane.	45
Figure 2.11. Comparison of Debye lengths inferred from impedance spectroscopy and TIRM measurements	46
Figure 2.12. The concentration of charge carriers in dodecane	47
Figure 2.13. The diffusion coefficient of charge carriers	49
Figure 2.14: The hydrodynamic diameter of 0.1% weight OLOA 11000 [®] in dodecane found by phase analysis light scattering.	50
Figure 3.1. A sketch of the domain and coordinate of the thin fluid cell.	67
Figure 3.2. Equivalent circuit used to fit impedance data.	73
Figure 3.3. Schematic of the thin fluid cell for impedance spectroscopy measurements.	79

- Figure 3.4. Nyquist plot comparing the impedance spectra of 1.0% wt. OLOA 11000[®] in dodecane (filled circles)[17] and 1.1% wt. (19.5 mM) Span 80[®] in dodecane (open blue squares). 81
- Figure 3.5. Comparison of various models (curves) with experimental data (symbols). 85
- Figure 3.6. Nyquist plot (a) and Bode plot (b) of the impedance and the best fit CPE model for 10.5 mM Span 20. 87
- Figure 3.7. Nyquist plot (a) and Bode plot (b) of the impedance and the best fit CPE model for 10.0 mM Span 85. 88
- Figure 3.8. Nyquist plot (a) and Bode plot (b) of the impedance and the best fit CPE model for 48.9 mM Span 85. 89
- Figure 3.9. Ratio of the real part (a) and imaginary part (b) of the impedance calculated from the circuit model to the transport model versus frequency for various ratios of the gap distance, L , to the Debye length λ_D . 93
- Figure 3.10. Operational diagram for thin cell impedance spectroscopy with charge adsorption. 96
- Figure 3.11. Conductivity of Span 20[®] (red circles), Span 80[®] (blue squares) and Span 85[®] (green triangles) in dodecane. 98
- Figure 3.12. Debye lengths of Span 20[®] (red circles), Span 80[®] (blue squares), and Span 85[®] (green triangles). 99
- Figure 3.13. Bulk charge concentration of Span 20[®] (circles), Span 80[®] (squares), and Span 85[®] (triangles) in dodecane. 102
- Figure 3.14. Diffusion coefficients of charge carriers of Span 20[®] (red circles), Span 80[®] (blue squares), and Span 85[®] (green triangles) in dodecane plotted on a log-log scale. 103
- Figure 3.15. The charge adsorption rate constant, k_a , is plotted versus surfactant concentration for Span 20[®] (red circles), Span 80[®] (blue squares), and Span 85[®] (green triangles) in dodecane. 104
- Figure 3.16. Desorption rate constants versus surfactant concentration for Span 20[®] (circles) and Span 80[®] (squares) in dodecane. 107
- Figure 3.17. Possible schematic of charge adsorption mechanism between surfactant at the electrode-liquid interface and micelles in the bulk. 109

Figure 3.18. Potentiostatic data for 0.1% Span 80® in dodecane.	111
Figure 4.1. Phase analysis light scattering data of surfactants in dodecane.	125
Figure 4.2. Conductivity measurements obtained from impedance spectroscopy versus surfactant concentration in mM.	127
Figure 4.3. Charge concentrations of different surfactants in dodecane measured with impedance spectroscopy with a 10 µm thin cell.	129
Figure 4.4. Molar conductivity versus hydrodynamic micelle diameter measured from phase analysis light scattering.	131
Figure 4.5. Molar conductivity of the surfactant solutions versus the estimated Diameter of the polar core found by subtracting the hydrodynamic diameter by 2 tail lengths.	132
Figure 4.6. Charge carriers per surfactant versus hydrodynamic diameter measured with phase analysis light scattering of 10 mM solutions in dodecane.	133
Figure 4.7. Charge carriers per surfactant using versus the estimated hydrated core diameter.	134
Figure 4.8. Conductivity measurements made with a DT-700 nonaqueous conductivity meter. Solutions of Span 85® (black circles), Triton X-15® (red triangles), Tergitol NP-4® (green squares), Tergitol TMN-3® (yellow diamonds), Tergitol 15-S-3® (blue triangles) in dodecane.	136
Figure 4.9. Average hydrodynamic diameters of micelles found from phase analysis light scattering versus concentration of surfactant in dodecane.	137
Figure 5.1. The rotating disk approach to streaming potential measurement.	146
Figure 5.2. Streaming potential near a mica surface in dilute KCl solution.	147
Figure 5.3. Streaming potential (blue circles) measurement of mica in deionized water with a 4000 RPM square wave rotation rate (black curve) applied with the standard procedure used for aqueous solutions adjusting glassy carbon electrodes for the Ag/AgCl sensors.	152
Figure 5.4. A) Mica in 0.5% wt. AOT® in dodecane measured with glassy carbon electrodes connected to a nanovoltmeter. B) Mica in 0.5% wt. AOT® in dodecane measured with glassy carbon electrodes connected to an electrometer.	153

- Figure 5.5. Mica in 0.5% wt. AOT[®] in dodecane measured with glassy carbon electrodes, an electrometer, and a long 10 minute rotation time plotted on the right axis. 155
- Figure 5.6. Mica in 0.5% wt. AOT[®] in dodecane at 4000 RPM (black), 3000 RPM (red), 2000 RPM (green), and 1000 RPM (yellow). 156
- Figure 5.7. A) Schematic of potential and current lines near a positive rotating disk as calculated in[6]. B) Data using the method for nonpolar liquids with sensor at axis and disk edge with 0.5% AOT[®] dodecane. 158
- Figure 5.8. Mica in 1.5% AOT[®] dodecane, 4000 RPM with a positively charged bare surface (blue curve) and with negatively charged carbon black particles added to the solution (red curve). 159
- Figure 5.9. Rotation rate dependence of mica in 0.5% wt and 10% wt. AOT[®]. 161
- Figure 5.10. A schematic of the equivalent circuit of the apparatus. 165
- Figure 5.11. The fraction of change remaining in the potential versus time is shown on a semilog-y plot for mica surface in 1.5%wt AOT[®] in dodecane. 166
- Figure 5.12. Time constant of the streaming potential decay versus conductivity. 167
- Figure 5.13. Comparison between electrophoretic mobility of silica particles and a fused silica surface. 169
- Figure 5.14. Zeta potential of glass coated with a conductive ITO layer. 170

Chapter 1 Introduction and background to nonpolar liquids

1.1 Introduction

The stability of particle suspensions is vitally important to many industrial applications and is one of the most studied topics of colloid science.[1] The vast majority of work in this area is focused on particles in aqueous solvents.

Electrostatic interactions in aqueous media are often used to control particle stability. Free charges are abundant in aqueous media and promote electrostatic stability by yielding charge to solid surfaces and form diffuse clouds of charge around a charged surface that enhances electrostatic repulsion.[2] Nonpolar solvents, such as alkanes and other hydrocarbons, are non-aqueous fluids characterized by a low dielectric constant (~ 2) compared to water (~ 80).

Following Coulomb's law, the low permittivity of nonpolar solvents gives rise to long range electrostatic attraction that is unfavorable for the formation of free charges.[3] The low concentration of free charge in nonpolar liquids result in very low electrical conductivities. In pure n-hexane the electrical conductivity is only 10^{-13} S/m; by contrast, the conductivity of deionized water is greater than 10^{-6} S/m.[4]

Despite the high energetic barrier to charge dissociation, charges can be formed in nonpolar liquids. In the 1950s Klinkenberg and Van der Minne found that amphiphilic surfactants can raise the conductivity of highly purified hydrocarbons and reduce the risk of explosions from electrostatic discharge for the petroleum industry.[5] Additionally, surfactant “dopants” like those listed in Table 1.1 can facilitate charge on particles leading to electrostatic stabilization in nonpolar liquids.[1, 3, 6-14] In addition to the petroleum industry, charges in nonpolar liquids can be used for other applications including lithographic printing[15], electrophoretic ink[16-18], and engine oils oil.[8-10] While these technologies are well established, the underlying mechanisms for the formation of charge in solution and on surfaces are not yet well understood.

Surfactant molecules aggregate in nonpolar media to form aggregate structures called micelles or sometimes referred to as “inverse micelles”. [19-22] The polar heads of the surfactant form the core of the micelle and the hydrophobic tails extend into the nonpolar solvent. Inverse micelles may range in size from 1-50 nm in diameter. Inverse micelles are large enough to sequester charge in the polar core of the micelle and serve as the “charge carriers” in nonpolar liquids.[22-26] For weak electrolytes in water the charge concentration increases with the square root of the added electrolyte concentration.[27, 28] In nonpolar liquids, however, many investigators have shown that when micelles are present the charge carrier concentration of nonpolar media is directly proportional to the

concentration of surfactant.[23, 29-34] Various charge formation mechanisms have been proposed to account for this proportionality. Charge fluctuation, disproportionation, and ion-pair dissociation are three prevalent mechanisms for the formation of charge that are currently debated.[3, 20, 28, 30, 35-38] Further characterization of the charge carriers is needed in order to properly understand the charge formation mechanisms and the relationship between the surfactant structure and the charge carriers in solution.

The electrical conductivity of a solution is a fairly simple measurement, however the conductivity depends on both the charge concentration and the mobility of the charge carrying species. A conductivity measurement alone is not enough to determine the charge concentration due to the coupling with mobility. Some researchers have developed independent measurements of either the charge concentration or the Debye length in addition to measuring conductivity. The Debye length is the characteristic screening length of the electrical double layer and is inversely proportional to the square root of the ionic strength. Some of these measurement approaches require suspended particles such as Total Internal Reflection Microscopy (TIRM)[23], radial distribution functions of suspended particles[32, 39], and particle pair interactions.[33] While these techniques are effective, they can only be used to make measurements on stable systems. Another method for measuring the Debye length is with a Surface Forces Apparatus (SFA).[40, 41] Additionally, a polarization cell can be used to apply a

DC voltage to a doped nonpolar fluid and fit the resulting current decay to a double layer capacitance to estimate the Debye length.[18, 22-26, 36, 42-45] Using these techniques the mobility of the charge carriers can then be calculated from the measured conductivity charge concentrations providing information on the size, and concentration of the charge carriers that arise from a particular surfactant.

The work presented in this thesis describes the development of experimental techniques to characterize charge in surfactant doped nonpolar liquids, and their interactions with solid surfaces. In addition to establishing characterization techniques this effort attempts to provide valuable insights on the behavior of charge carriers in surfactant doped nonpolar liquids interact at electrode interfaces, the surfactant and micelle properties that can best predict the charge carrier concentration, and the zeta potential that arises on flat surfaces.

In chapter 2 (published previously) [46] we present the use of impedance spectroscopy to study charge properties of surfactant doped nonpolar liquid. Solutions of the commercial surfactant OLOA 11000[®] in dodecane were studied using impedance spectroscopy in a 10 μm fluid cell for dopant concentrations between 0.1 and 10% by weight. A low amplitude oscillatory voltage is applied to the fluid cell over a range of frequencies and the current is measured. The relationship between the measured current and the applied voltage at each frequency is recorded as the impedance, which characterizes the complex

resistance of the cell. The impedance is fit with an equivalent circuit having four elements including a fluid resistance and a constant-phase element representing the double-layer capacitance. The fluid resistance is attributed to the conductivity of the solutions. The Gouy-Chapman theory for the double layer capacitance is applied under the assumptions that the zeta potential of the Indium Tin Oxide (ITO) coated slides glass slides is small compared to the thermal voltage and the charge carriers are univalent. The measured double-layer capacitances are used to determine the Debye length and then converted to the charge carrier concentration. The measured conductivity is divided by the independently measured charge carrier concentration to infer the hydrodynamic diameters for the charged micelles.

In chapter 3 (previously published) [47] the thin cell impedance spectroscopy technique is applied to a series of nonionic surfactants in dodecane, Span 85[®], Span 80[®], and Span 20[®] listed in Table 1.1.

The impedance measured from 10 mHz to 100 kHz is qualitatively different for these solutions than the measured impedance of the OLOA 11000[®] solutions discussed in chapter 2. At low frequencies an additional local maximum is observed in the imaginary part of the impedance that is attributed to charge adsorption and desorption. A model accounting for the charge adsorption and desorption in addition to the double layer capacitance is fit to the measured

impedance to determine the conductivity, charge concentration, the kinetic parameters of charge adsorption and desorption.

In chapter 4 (in preparation for submission) the charge carrier properties and micelle sizes of five common commercial surfactants in dodecane are compared. The surfactants, AOT[®], OLOA 11000[®], Span 85[®], Span 80[®], and Span 20[®] (structures shown in Table 1.1) all form micelles at concentrations above the critical micelle concentration (CMC) and increase the electrical conductivity of dodecane. The molar conductivity and charge concentration of each surfactant measured with impedance spectroscopy using the methods presented in chapters 2 and 3 are compared. The hydrodynamic diameter of the micelles formed by the surfactants is measured with Phase Analysis Light Scattering (PALS). The diameter of the polar core of the micelles is estimated as the hydrodynamic diameter less twice the tail length of the surfactant. The molar conductivity of the different surfactants increases exponentially with the estimated diameter of the polar core. Unlike aqueous solutions, the larger charge carrier structures provide the largest conductivity. The exponential correlation is rationalized by posing that the number of charge carriers per micelle exponentially decreases with the ratio of the Bjerrum length to the diameter of the polar core of the micelles as suggested by the charge fluctuation model. The surprising result suggests that the size of the polar core of the micelle is a critical property in determining the charge concentration in surfactant doped nonpolar liquids.

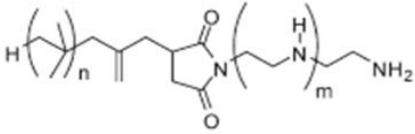
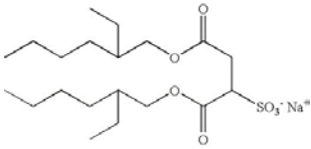
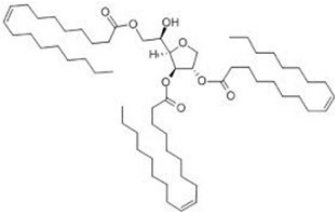
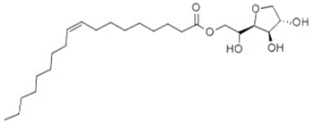
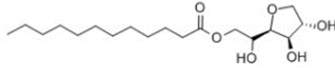
Chapter 5 (in preparation for submission) presents a novel technique to study the interactions between surfactants in nonpolar liquids and solid surfaces. The author presents an apparatus and a method for determining the zeta potential of planar solids in contact with surfactant doped nonpolar liquids. Streaming potential is produced by rotating disk-shaped mica, fused silica, and glass coated ITO samples in surfactant-doped dodecane. A glassy carbon electrode near the sample at its axis measures the streaming potential with respect to a second glassy carbon electrode far from the sample. Upon rotating the disk in solution, the measured potential changes rapidly before asymptotically approaching a steady value over a timescale from fractions of a second to seconds. The measured potential difference between a static disk and a rotating disk is proportional to the $3/2$ power of the rotation rate, which agrees with the theory of streaming potential for the rotating disk. Other tests are presented to confirm that the difference between the potential before rotation and its asymptotic value during rotating is the streaming potential arising due to the shear flow next to the charged surface. The zeta potentials of the flat surface sample is calculated from the measured streaming potential. The zeta potentials of various surfaces in dodecane doped with surfactant is presented. The zeta potential of a fused silica surface in dodecane doped with OLOA 11000[®] varies between -5 mV to -40 mV depending on the surfactant concentration agreeing qualitatively with zeta determined from electrophoretic mobility measurements of silica particles.

This apparatus and method is ideal for measuring the zeta potential of the ITO coated glass slides used as electrodes in the previous chapters. All of the Debye lengths presented in this thesis were determined from impedance spectroscopy measurements of the double layer capacitance assuming that the zeta potential “native” to the ITO coated glass is small compared to the thermal voltage. This assumption is confirmed by independently determining the zeta potential on the surface by measuring the streaming potential. The magnitude of the zeta potential of ITO coated glass is smaller than 25 mV (the thermal voltage at room temperature) in solutions of OLOA 11000[®], AOT[®], and Span 20[®] in dodecane, which means that the diffuse layer capacitance near the ITO equals the permittivity divided by the Debye length, to a good approximation.

Finally, Chapter 6 offers some conclusions and directions for future research to better understand the nature of charge in surfactant doped nonpolar fluids.

The chapters that follow were written as self-contained papers and can be read in any order. There is also a certain amount of repetition in the introductory sections of each chapter.

Table 1.1 Common commercial surfactants known to add charge in nonpolar liquids and studied in this work

<p>OLOA 11000[®] Polyisobutylene succinimide</p>		<p>nonionic</p>
<p>Aerosol-OT[®] (AOT[®]) Sodium dioctylsulfosuccinate</p>		<p>anionic</p>
<p>Span 85[®] Sorbitan trioleate</p>		<p>nonionic</p>
<p>Span 80[®] Sorbitan monooleate</p>		<p>nonionic</p>
<p>Span 20[®] Sorbitan monolaurate</p>		<p>nonionic</p>

1.2 References

1. Lyklema, J., *Principles of interactions in non-aqueous electrolyte solutions*. Current Opinion in Colloid & Interface Science, 2013. **18**(2): p. 116-128.
2. Berg, J.C., *An Introduction to Interfaces and Colloids: The Bridge to Nanoscience*. 2010, Singapore: World Scientific Publishing.
3. Morrison, I.D., *Electrical charges in nonaqueous media*. Colloids and Surfaces A: Physicochemical and Engineering Aspects, 1993. **71**: p. 1-37.
4. Scaife, W.G., The natural electrical conductivity of organic liquids subjected to hydrostatic pressures. J. Phys. D: Appl. Phys., 1974. **7**: p. 647-652.
5. *Electrostatics in the Petroleum Industry: The Prevention of Explosion Hazards*. . 1958: Elsevier.
6. Chen, W.J., *Stabilization and electrostatic deposition of aqueous and non-aqueous polymeric colloids*. PhD Thesis, 1988.
7. Poovarodom, S. and J.C. Berg, Effect of particle and surfactant acid-base properties on charging of colloids in apolar media. J Colloid Interface Sci, 2010. **346**(2): p. 370-7.
8. Pugh, R.J. and F.M. Fowkes, The Dispersibility and Stability of Carbon Black in Media of Low Dielectric Constant. 2 Sedimentation Volume of Concentrated Dispersions, Adsorption and Surface Calorimetry Studies. Colloids and Surfaces, 1984. **9**: p. 33-46.
9. Pugh, R.J. and F.M. Fowkes, The Dispersibility and Stability of Coal Particles in Hydrocarbon Media with a Polyisobutene Succinamide Dispersing Agent. Colloids and Surfaces, 1984. **11**: p. 423-427.
10. Pugh, R.J., T. Matsunaga, and F.M. Fowkes, The Dispersibility and Stability of Carbon Black in Media of Low Dielectric Constant. 1, Electrostatic and Steric Contributions to Colloidal Stability. Colloids and Surfaces, 1983. **7**: p. 183-207.
11. Gacek, M., et al., Effects of trace water on charging of silica particles dispersed in a nonpolar medium. Langmuir, 2012. **28**(31): p. 11633-8.

12. Gacek, M., G. Brooks, and J.C. Berg, *Characterization of mineral oxide charging in apolar media*. Langmuir, 2012. **28**(5): p. 3032-6.
13. Gacek, M.M. and J.C. Berg, Investigation of surfactant mediated acid-base charging of mineral oxide particles dispersed in apolar systems. Langmuir, 2012. **28**(51): p. 17841-5.
14. Poovarodom, S., S. Poovarodom, and J.C. Berg, *Effect of alkyl functionalization on charging of colloidal silica in apolar media*. J Colloid Interface Sci, 2010. **351**(2): p. 415-20.
15. Gacek, M.M. and J.C. Berg, Effect of synergists on organic pigment particle charging in apolar media. Electrophoresis, 2014. **35**: p. 1766-1772.
16. Smith, G.N. and J. Eastoe, *Controlling colloid charge in nonpolar liquids with surfactants*. Phys Chem Chem Phys, 2013. **15**(2): p. 424-39.
17. Novotny, V., *Applications of Nonaqueous Colloids*. Colloids and Surfaces, 1987. **24**: p. 361-375.
18. Parent, M.E., et al., Influence of surfactant structure on reverse micelle size and charge for nonpolar electrophoretic inks. Langmuir, 2011. **27**(19): p. 11845-51.
19. Eicke, H.F., *Surfactants in nonpolar solvents: Aggregation and Micellization*. Topics in Current Chemistry, 1980. **87**: p. 85-145.
20. Eicke, H.F., M. Borkovec, and B. Das-Gupta, *Conductivity of Water-in-Oil Microemulsions: A Quantitative Charge Fluctuation Model*. Journal of Physical Chemistry, 1989. **93**: p. 314-317.
21. Eicke, H.F. and H. Christen, *Is Water Critical to the Formation of Micelles in Apolar Media?* Helvetica Chimica Acta, 1978. **61**(6): p. 2258-2263.
22. Beunis, F., et al., Micellization and adsorption of surfactant in a nonpolar liquid in micrometer scale geometries. Applied Physics Letters, 2010. **97**(18): p. 181912.
23. Prieve, D.C., et al., Two Independent Measurements of Debye Lengths in Doped Nonpolar Liquids. Langmuir 2008. **24**: p. 1120-1132.

24. Beunis, F., et al., Inverse micelles as charge carriers in nonpolar liquids: Characterization with current measurements. *Current Opinion in Colloid & Interface Science*, 2013. **18**(2): p. 129-136.
25. Beunis, F., et al., *Electric charging of inverse micelles in a nonpolar liquid with surfactant*. *Colloids and Surfaces A: Physicochemical and Engineering Aspects*, 2014. **440**: p. 10-19.
26. Beunis, F., et al., *Dynamics of charge transport in planar devices*. *Physical Review E*, 2008. **78**.
27. Fu, R. and D.C. Prieve, Electrical Charges in Nonaqueous Solutions I: Acetone-Water Mixtures as Model Polar Solvents. *Langmuir*, 2007. **23**: p. 8048-8052.
28. Dukhin, A.S., Properties of electrolytic solutions: Dissociation, fluctuation and disproportionation models for ionization of surfactant solutions in low- and non-polar liquids. *JCIS manuscript*, 2012.
29. Dukhin, A.S. and P.J. Goetz, How non-ionic "electrically neutral" surfactants enhance electrical conductivity and ion stability in non-polar liquids. *Journal of Electroanalytical Chemistry*, 2006(588): p. 44-50.
30. Guo, Q., V. Singh, and S.H. Behrens, *Electric charging in nonpolar liquids because of nonionizable surfactants*. *Langmuir*, 2010. **26**(5): p. 3203-7.
31. Schmidt, J., et al., Conductivity in nonpolar media: experimental and numerical studies on sodium AOT-hexadecane, lecithin-hexadecane and aluminum(III)-3,5-diisopropyl salicylate-hexadecane systems. *J Colloid Interface Sci*, 2012. **386**(1): p. 240-51.
32. Hsu, M.F.D., E. R.; Weitz, D. A., *Charge Stabilization in Nonpolar Solvents*. *Langmuir*, 2005. **21**: p. 4881-4887.
33. Sainis, S.K., et al., Electrostatic Interactions of Colloidal Particles in Nonpolar Solvents: Role of Surface Chemistry and Charge Control Agents. *Langmuir*, 2008. **24**: p. 1160-1164.
34. Roberts, G.S., et al., Electrostatic Charging of Nonpolar Colloids by Reverse Micelles. *Langmuir*, 2008. **24**: p. 6530-6541.
35. Bombard, A.J. and A. Dukhin, *Ionization of a Nonpolar Liquid with an Alcohol*. *Langmuir*, 2014.

36. Strubbe, F., et al., *Generation current of charged micelles in nonaqueous liquids: measurements and simulations*. Journal of Colloid and Interface Science, 2006. **300**(1): p. 396-403.
37. Hall, D.G., *Conductivity of Microemulsions: An Improved Charge Fluctuation Model*. Journal of Physical Chemistry, 1990. **94**: p. 429-430.
38. Michor, E.L. and J.C. Berg, Extension to the charge fluctuation model for the prediction of the conductivity of apolar, reverse micellar systems. Langmuir, 2012. **28**(45): p. 15751-5.
39. Espinosa, C.E., et al., Particle charging and charge screening in nonpolar dispersions with nonionic surfactants. Langmuir, 2010. **26**(22): p. 16941-8.
40. Briscoe, W.H. and R.G. Horn, Electrical double layer interactions in a non-polar liquid measured with a modified surface force apparatus. 2004: p. 147-151.
41. Briscoe, W.H. and R.G. Horn, Direct Measurement of Surface Forces Due to Charging of Solids Immersed in a Nonpolar Liquid. Langmuir, 2002. **18**: p. 3945-3956.
42. Beunis, F., et al., *Power-law transient charge transport in a nonpolar liquid*. Applied Physics Letters, 2007. **90**(18): p. 182103.
43. Marescaux, M., et al., Impact of diffusion layers in strong electrolytes on the transient current. Physical Review E, 2009. **79**(1).
44. Kim, J., et al., Ionic Conduction and Electrode Polarization in a Doped Nonpolar Liquid. Langmuir, 2005. **21**: p. 8620-8629.
45. Kornilovitch, P. and Y. Jeon, *Transient electrophoretic current in a nonpolar solvent*. Journal of Applied Physics, 2011. **109**(6): p. 064509.
46. Yezer, B.A., et al., Use of electrochemical impedance spectroscopy to determine double-layer capacitance in doped nonpolar liquids. Journal of Colloid and Interface Science, 2015. **449**: p. 2-12.
47. Yezer, B.A., et al., Determination of charge carrier concentration in doped nonpolar liquids by impedance spectroscopy in the presence of charge adsorption. Journal of Colloid and Interface Science, 2016. **469**: p. 325-337.

Chapter 2

Use of impedance spectroscopy to determine double-layer capacitance in doped nonpolar liquids

2.1 Introduction

Nonpolar liquids like alkanes are good insulators. Nonetheless the presence of as little as one part-per-billion of certain chemicals can cause electrical effects.[1] For example, pumping of highly refined hydrocarbons led to explosions in refineries, whose cause was found to be sparks produced by very large streaming potentials needed to neutralize small streaming currents arising from trace charges on metal pipe walls.[1] To prevent these explosions, Klinkenberg & van der Minne[1] recommend the addition of a dopant to raise the conductivity to at least 50 pS/m which lowers any streaming potential by orders of magnitude. This extremely low conductivity (distilled de-ionized water has a conductivity 10^5 times higher) can be achieved with the addition of as little as 20 $\mu\text{mol}/\text{m}^3$ of the particular dopant recommended by them.

Dopants are frequently added to oils either to raise the conductivity or to generate charges at interfaces. For example, the OLOA 11000[®] used in this study is routinely added to motor oil to control soot formation in internal combustion engines.[2] Dopants are also added to dispersions of pigments in oils for use in

electrophoretic display technology.[3] In this example, the opposite charge on black and white pigment particles plays an essential role by linking the black or white status of any pixel to the polarity of an applied electric field. Many other applications of charges in nonpolar liquids are described in two excellent reviews by Novotny[4] and Morrison.[2]

Dopants are usually surfactants, molecules containing a polar head group connected to one or more nonpolar tails. For example, the main ingredient in OLOA 11000[®] is poly(isobutylene) succinimide while Aerosol-OT[®] (AOT) is dioctyl sodium sulfosuccinate. The head group of AOT[®] contains an ionic group which is most likely involved in the formation of charge carriers or surface charge. However ionic head groups are not required. For example, Span 85[®] (sorbitan oleate) is a nonionic surfactant; yet Behrens *et al.*[5, 6] found that both solution conductivity and solid-liquid charge density increase when Span 85[®] is added to a nonpolar liquid. The dopants aggregate to reverse micelle structures that may consist of 5-100 molecules and likely serve as charge carriers.[2] The mechanism for charge formation is not revealed but it might simply arise from ionic contaminants present in the solvent and dopant.

Knowledge about the concentration of charge carriers as a function of the total concentration of surfactant is very useful to screen potential mechanisms for charge formation. The most commonly measured property is conductivity which depends both of the number of charge carriers as well as their mobility (size).

Most past studies of charge formation have relied on dynamic light scattering [7, 8] or fitted simulations [9-11] to infer the hydrodynamic radius; carrier mobility is calculated from Stokes law. Then measurements of conductivity can be used to deduce the concentration of carriers. Unfortunately most of the commercial surfactants are highly polydisperse mixtures which produce a wide range of micelle sizes. Light scattering detects all micelles whereas our earlier results suggest that only the largest micelles are charged.[12] Using the average micelle size (from light scattering) to infer charge carrier concentration from conductivity can lead to significant errors.

In this manuscript, we explore what electrochemical impedance spectroscopy (EIS) reveals about doped nonpolar liquids. In impedance spectroscopy, low-amplitude sinusoidal oscillations in applied voltage difference are applied and the resulting sinusoidal oscillations in current are measured for a wide range of frequencies. This procedure avoids large, hard-to-measure “spikes” in current which result when a step-change in voltage is made at the start of potentiostatic experiments used in most past studies.[9-11]

Previous studies of nonpolar fluids with impedance spectroscopy inferred the conductivity from the high-frequency portion of the spectra.[7, 13, 14] Here, we show that the electric permittivity of the solution can also be obtained. The main novelty of this contribution, however, is obtaining the double-layer capacitance from the moderate- to low-frequency portion of the spectra. When the electrode-

fluid interface is not significantly charged (in the absence of any applied voltage), the double-layer capacitance is simply related (by the Gouy-Chapman theory) to the Debye length which, in turn is related to ionic strength of the bulk solution. To the extent that the charge carriers can be assumed to be univalent, the ionic strength is equal to the concentration of charge carriers.

At high concentrations of the dopant OLOA, we find that double-layer capacitance can be represented well in the impedance spectrum by a simple electrical capacitor. At low concentrations of the dopant and at low frequencies, however, a simple capacitor does not fit the spectra well. Instead a constant-phase element (CPE) must be used in order to obtain reasonable fit of the spectra. CPE's are commonly used in fitting electrochemical impedance spectra.[15, 16] They arise when the RC time constant of the double-layer is nonuniform over the surface of the electrode.

Debye lengths obtained by fitting the impedance spectra using a CPE are in good agreement with Debye lengths obtained by measuring force-versus-distance with TIRM in a similar doped nonpolar liquid.[12] Having the charge carrier concentration inferred from Debye lengths, we translated the measured conductivities into a hydrodynamic size for charge carriers. As in our past work,[12] this size inferred from conductivity is much larger than the hydrodynamic size inferred from dynamic light scattering. This disparity can be reconciled if only the largest micelles of the dopant are charged.

2.2 Materials and methods

OLOA 11000[®] (Chevron Oronite Co) was used as received and mixed with anhydrous dodecane (99+%, Sigma-Aldrich). The OLOA 11000[®] is a commercial additive consisting of a substantial fraction of poly(isobutylene succinimide) (PIBS) dispersed in mineral oil. The PIBS had an average molecular weight of 1200 g/mol.[17] The PIBS molecule contains a nonpolar polyisobutylene tail connected to a polar succinimide head group.[17] The mixtures were not dried and the humidity was not controlled. All solutions of OLOA 11000[®] in dodecane were stored in a desiccator when not directly in use. All solutions are reported as weight percent. The hydrodynamic diameter of the reverse micelles was measured by Phase Analysis Light Scattering (PALS) using a Malvern ZetaSizer Nano ZSP (Malvern Instruments, Malvern, UK).

A schematic diagram of the thin cell appears in Figure b. Pillars, in the form of microscopic particles, separated the electrodes of the cell used in these experiments. Silica particles 8 micrometers in diameter (Cospheric, Santa Barbara, CA) were added to solutions of OLOA 11000[®] in dodecane at a particle concentration of 1 mg/mL. The particles established a gap between the cell's electrodes and were assumed to be electrically inert by their dielectric nature and dilute presence. In each experiment, fifteen microliters of the dodecane containing surfactant and spacer particles was deposited onto a glass microscope slide coated with a 100-nm-thick indium tin oxide (ITO) layer (Sigma-Aldrich)

using a 25 microliter gas-tight syringe (Hamilton Co). A second ITO coated slide was aligned on top of the fluid to complete the parallel plate polarization cell. Capillary forces held the cell together without the use of adhesives. The fluid filled a distinct area of the cell that varied with each assembly; the area of the fluid layer was measured with image analysis using Image J software (NIH). The gap between the plates was calculated for each cell by dividing the area of the liquid film into the known added volume. Electrical leads were attached to the ITO-coated side of the glass with conductive silver epoxy (MG Chemicals). The cell was shorted until the open-circuit voltage was lower than 10 mV. After each measurement the cell was disassembled and the electrodes were rinsed three times with hexane (98+% Alpha Aesar).

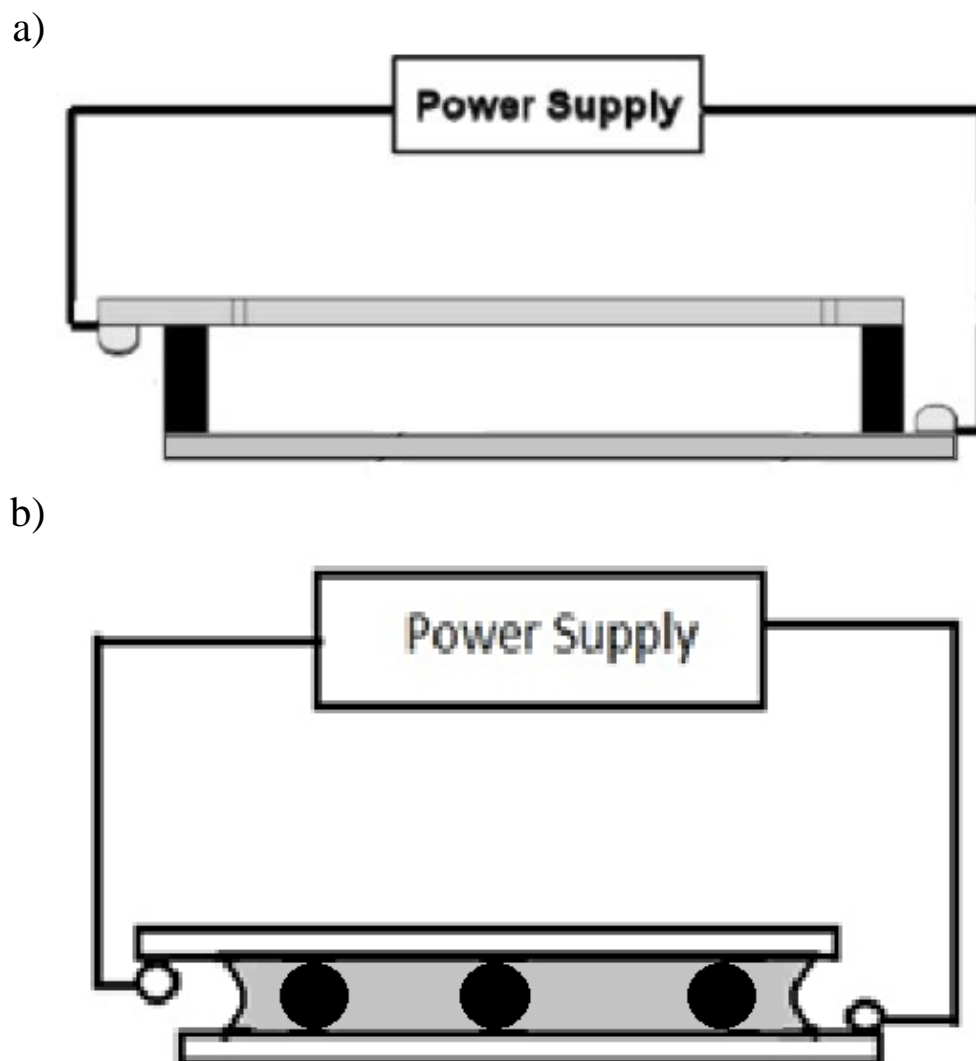


Figure 2.1. Schematic of the fluid cell. Two glass microscope slides coated with ITO were separated by a 1mm thick polycarbonate gasket and fluid is injected through holes in the top slide (a) used in previous work.[12] A thin fluid cell (b) is separated by 8 μm diameter silica microspheres as spacer particles. Fluid was placed on the bottom slide before the top slide is applied and held together by capillary forces. The slides had dimensions of 2.5 cm by 7.6 cm.

Electrochemical impedance spectroscopy (EIS) frequency sweeps were performed with the fluid cell connected to a potentiostat (Princeton Applied Research VersaSTAT 3). The instrument applied a 10mV root mean squared (RMS) potential across the cell at frequencies decreasing from 100 kHz to 1Hz

collecting 10 points per decade while maintaining a 0V DC bias. The impedance was calculated at each frequency after a measurement delay time of 0.1 seconds using a single sine technique with a frequency analyzer using discrete Fourier transforms. The measured impedance was averaged over 10 periods before the cell impedance was reported for a particular frequency.

In tests for linearity, a function generator (Agilent 33120A) sent a single frequency sinusoid to a Princeton Applied Research Model 173 potentiostat connected to the cell. The current was monitored with an Agilent 54624A oscilloscope.

2. 3 Theory

The theory of EIS is well-established, but in most cases the theory is applied to the potential difference between a working electrode, the electrode of interest, and a reference electrode.[15] Here the potentiostat is connected across the cell terminals; the reference electrode terminal on the potentiostat is short-circuited to the terminal of the counter electrode. In view of this difference, we briefly derive the equations used to convert the measured current and specified voltage to the parameters of equivalent circuits and to intrinsic quantities.

2.3.1 Primitive 2-Element Circuit Model

Current passing through the circuitry outside the fluid cell can either accumulate opposite charges on the two plates (if the fluid has a nonzero

conductivity) or some of the external current can pass through the fluid. Denote these two contributions to the total current as $I_C(t)$ and $I_R(t)$, respectively. The current flowing through fluid requires a potential drop $V(t)$ between the plates which satisfies Ohm's law,

$$I_R(t) = \frac{V(t)}{R_f}, \quad (2.1)$$

where

$$R_f = \frac{d}{A_f K} \quad (2.2)$$

is the resistance, K is the conductivity of the fluid, d is the distance between the two plates and A_f is the area of the two plates wet by the fluid. The portion of the current accumulating at the plates satisfies Ohm's law for capacitors,

$$I_C(t) = C_c \frac{dV}{dt}, \quad (2.3)$$

where

$$C_c = \frac{\epsilon_f A_f + \epsilon_0 A_0}{d} \quad (2.4)$$

is the capacitance, ϵ_f and ϵ_0 are the permittivities of the liquid and air held between the plates and A_0 is the remaining area of the ITO electrode not wet by the liquid. In writing the net capacitance as the sum, we are treating the liquid- and air-filled regions between the two plates as two capacitors acting in parallel, which is reasonable as long as the potential on either plate is uniform across its

entire area $A_f + A_0$. Taking the total current $I(t)$ through the external circuit to be the sum of (2.1) and (2.3), one obtains

$$I(t) = I_R(t) + I_C(t), \quad (2.5)$$

which means that the capacitor and resistor act in parallel (see Figure 2.2a).

In EIS, a sinusoidally varying voltage $V(t)$ is applied and the resulting periodic current $I(t)$ is measured. The solution to (2.1) - (2.5) can most easily be obtained by representing the sinusoidally varying voltage and current by complex exponentials,

$$\tilde{V}(t) = V_0 e^{-i\omega t} \quad \text{and} \quad \tilde{I}(t) = I_0 e^{-i\omega t}, \quad (2.6)$$

where ω is the angular frequency and V_0 and I_0 represent the amplitudes of the oscillating signals (which might be complex quantities). The tilde (\sim) was added to distinguish the complex time-dependent quantities (\tilde{V} and \tilde{I}) from their real parts (V and I). Substituting (2.6) into (2.1) - (2.5) and solving yields

$$\tilde{I}(t) = \frac{\tilde{V}(t)}{Z}$$

where

$$Z = \left[R_f^{-1} + \left(\frac{i}{\omega C_c} \right)^{-1} \right]^{-1} \quad (2.7)$$

is the complex impedance. The product $R_f C_c$ is a convenient characteristic time-constant for this circuit; we define this product as the timescale for charging the cell τ_c and use it to scale frequency:

$$\Omega = \omega R_f C_c \quad (2.8)$$

then the real and imaginary parts of the impedance are given by

$$\frac{\text{Re}(Z)}{R_f} = \frac{1}{1+\Omega^2} \quad \text{and} \quad \frac{\text{Im}(Z)}{R_f} = \frac{\Omega}{1+\Omega^2}. \quad (2.9)$$

The real and imaginary parts are equal for $\Omega = 1$ which corresponds to $\omega = 1/\tau_c$.

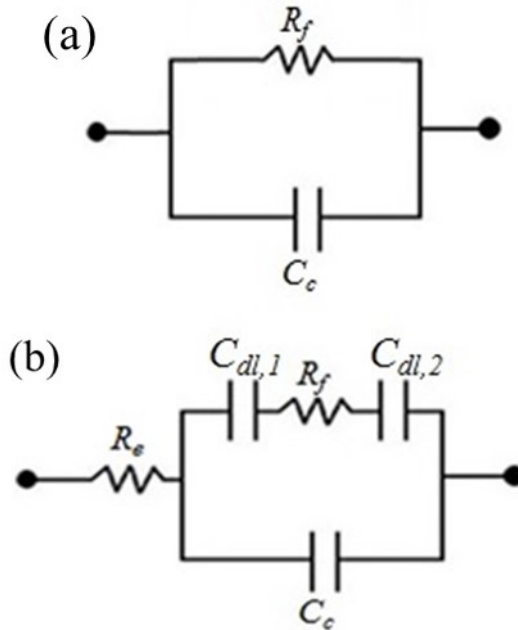


Figure 2.2. Two electronic circuit analogs used to model the EIS response.

2.3.2 5-Element Circuit Model

Electrons flow in the circuitry outside the cell, but ions or charged micelles carry the current inside the cell. By imposing (2.5), we are assuming that all of the current through the liquid $I_R(t)$ contributes to the total current $I(t)$ measured externally (rather than accumulate as a net charge at the electrode). In conventional electrochemical systems, Faradaic (redox) reactions might transform electronic charge carriers into ionic charge carriers at the rate prescribed by $I_R(t)$; however, we do not expect Faradaic charge transfer in these nonpolar fluids. Without Faradaic reactions, (2.5) can still hold if electrons and ions both accumulate on opposite sides of the interface at the rate prescribed by $I_R(t)$. If the rates of accumulation of charge from electrons and charge from ions have opposite signs, the net accumulation of charge on either plate is zero for this portion $I_R(t)$ of the total current $I(t)$; of course, the current associated with the capacitor $I_C(t)$ still accumulates a net charge having opposite signs on either plate.

The 2-element model requires that the accumulation of electrons and ions at a rate given by $I_R(t)$ to occur in layers of zero thickness. Zero-thickness layers at the interface are often assumed when describing the distribution of free charges in a good conductor like a metal. Nonpolar fluids, however, are poor conductors containing ionic charge carriers of both signs, a consequence of which is that the layer next to either plate in which ions accumulate is expected to have a nonzero

thickness. According to the Gouy-Chapman model,[18] ions accumulate next to a charged plate in a layer whose thickness scales with the Debye length,

$$\lambda_D = \sqrt{\frac{\epsilon_f k_B T}{2e^2 n_0}} \quad (2.10)$$

where k_B is Boltzmann's constant, T is absolute temperature, e is the charge on one proton and n_0 is the ionic strength (number per volume) of an electrically neutral bulk solution assumed to exist outside the layer. For example, the Debye lengths determined in experiments described herein varied between 30 nm and 500 nm, depending on the concentration of surfactant added to the nonpolar liquid. This is small compared to the electrode separation d but not always negligible.

In the Gouy-Chapman model, a potential drop (denoted by ζ) arises across this diffuse layer of ions. If the diffuse layer bears an integrated net charge per unit area of σ_d , its relationship to ζ is[18]

$$\sigma_d = -\sqrt{8n_0 \epsilon_f k_B T} \sinh\left(\frac{e\zeta}{2k_B T}\right)$$

for a 1-1 electrolyte. In order to accumulate more charges in this layer, the voltage drop across it must change, just like a capacitor. The differential capacitance C_{dl} is

$$\frac{C_{dl}}{A_f} = -\frac{d\sigma_d}{d\zeta} = \frac{\varepsilon_f}{\lambda_D} \cosh\left(\frac{e\zeta}{2k_B T}\right) \approx \frac{\varepsilon_f}{\lambda_D} \quad (2.11)$$

where the negative sign was inserted above because the sign of charge density σ_d is opposite to the sign of ζ . The final equation above applies when $|\zeta| \ll k_B T/e$.

Thus, in the absence of Faradaic reactions, all of the current $I_R(t)$ must accumulate in diffuse layers, one on each electrode. This is analogous to adding two capacitors C_{dl} in series with the resistor R_f . In Figure 2.2b we also add a fifth element, a small resistor R_e , to represent the impedance of the external circuit, which will be evident at very high frequencies. The corresponding overall impedance is

$$Z = R_e + \left[\left(R_f + \frac{2i}{\omega C_{dl}} \right)^{-1} + \left(\frac{i}{\omega C_c} \right)^{-1} \right]^{-1} \quad (2.12)$$

and the real and imaginary parts of the impedance are

$$\text{Re}(Z) = R_e + \frac{R_f}{1 + 4c + 4c^2 + \Omega^2} \quad (2.13)$$

and

$$\text{Im}(Z) = \frac{(2c + 4c^2)\Omega^{-1} + \Omega}{1 + 4c + 4c^2 + \Omega^2} R_f \quad (2.14)$$

where

$$c = \frac{C_c}{C_{dl}}. \quad (2.15)$$

For large frequencies ($\Omega \gg 2c$ or $R_f C_{dl} \omega \gg 2$), the impedance of the 5-element model [given by (2.13) and (2.14)] becomes equivalent to the impedance of the 2-element model [given by (2.9)], provided the resistance R_e is also added to the latter.

2.3.3 Constant-Phase Element Model

In the limit of very low frequencies, (2.13) predicts that $\text{Re}(Z)$ is $O(\omega^0)$ while (2.14) predicts that $\text{Im}(Z)$ is $O(\omega^{-1})$, which suggests that the cell should behave like a resistor and capacitor in series. But — instead of reaching a plateau in $\text{Re}(Z)$ as $\omega \rightarrow 0$ — our data typically display a slow monotonic increase with no evidence of a plateau (see Figure 2.5). This type of discrepancy has been widely reported in the EIS literature.[15, 19-21] The usual treatment[15] is to replace the double-layer capacitor — which corresponds to the impedance $2i/\omega C_{dl}$ in (2.12) — by a constant-phase element (CPE):

$$Z_{CPE} = Q^{-1} \left(\frac{i}{\omega} \right)^\alpha = \left[\cos\left(\frac{\pi\alpha}{2}\right) + i \sin\left(\frac{\pi\alpha}{2}\right) \right] Q^{-1} \omega^{-\alpha} = Q^{-1} \omega^{-\alpha} \exp\left(\frac{i\pi\alpha}{2}\right) \quad (2.16)$$

where $0 < \alpha < 1$. In the special case of $\alpha=1$, the real part of Z_{CPE} vanishes and the imaginary part corresponds to the impedance of a capacitor with $Q = C_{dl}/2$. For $0 < \alpha < 1$, both real and imaginary parts of Z_{CPE} are positive and increase like $\omega^{-\alpha}$ as $\omega \rightarrow 0$. This affords the possibility of fitting data like those in Figure 2.5. When

Z_{CPE} is expressed in polar form, the phase angle $\pi\alpha/2$ is independent of ω , which is why this form is called a “constant-phase element.”

The new version of (2.12) is

$$Z = R_e + \left[\left(R_f + Z_{CPE} \right)^{-1} + \left(\frac{i}{\omega C_c} \right)^{-1} \right]^{-1} \quad (2.17)$$

Determining the real and imaginary parts of this expression is straightforward but tedious. Once the values of the parameters Q and α are determined by fitting, the double-layer capacitance can be calculated from [19]

$$C_{dl} = 2 \left(Q R_f^{1-\alpha} \right)^{1/\alpha}. \quad (2.18)$$

The factor of two was added to the above expression because our circuit (see Figure 2.2b) consists of two capacitors in series. In the special case where $\alpha=1$, (2.18) leads to $Q = C_{dl}/2$.

2.3.4 Determination of the equivalent circuit parameters

We will compare parameters inferred from two different equivalent circuits whose impedances are given by (2.12) and (2.17). The determination of parameters is somewhat different in the two cases as we will now show.

2.3.5 5-Element Circuit

We first attempt to convert measurements of frequency-dependent $\text{Re}(Z)$ and $\text{Im}(Z)$ into values for C_c , C_{dl} , R_f and R_e by linear regression of experimental data to asymptotic forms of (2.13) and (2.14) which are linear if plotted correctly:

$$\lim_{\omega \rightarrow \infty} \text{Re}(Z) = R_e + \frac{1}{R_f C_c^2} \omega^{-2} + O(\omega^{-4}) \quad (2.19)$$

$$\lim_{\omega \rightarrow 0} \text{Re}(Z) = \frac{R_f}{a} + \left(\frac{R_f C_c}{a} \right)^2 R_f \omega^2 + O(\omega^4) \quad (2.20)$$

$$\lim_{\omega \rightarrow \infty} \omega \text{Im}(Z) = \frac{1}{C_c} - \frac{1+2c}{R_f^2 C_c^3} \omega^{-2} + O(\omega^{-4}) \quad (2.21)$$

$$\lim_{\omega \rightarrow 0} \omega \text{Im}(Z) = \frac{2}{C_{dl} + 2C_c} + \frac{R_f^2 C_c}{(1+2c)^3} \omega^2 + O(\omega^4) \quad (2.22)$$

where $a = 1+4c+4c^2$ and c is defined by (2.15). In (2.20) we have neglected R_e (about 100Ω) compared to R_f (at least $50 \text{ k}\Omega$). Thus the y-intercepts of $\text{Re}(Z)$ and $\text{Im}(Z)$, plotted versus ω^{-2} , should yield values for R_e and C_c . Once C_c is known, the y-intercept of $\omega \text{Im}(Z)$ plotted versus ω^2 can be used to infer C_{dl} . Then c and a can be calculated and the y-intercept of $\omega \text{Im}(Z)$ plotted versus ω^2 can be used to infer R_f .

2.3.6 Circuit with CPE

The analogs to (2.19) and (2.21) when the impedance is given by (2.17) are

$$\lim_{\omega \rightarrow \infty} \operatorname{Re}(Z) = R_e + \frac{1}{R_f C_c^2} \omega^{-2} - \frac{\cos\left(\frac{\pi\alpha}{2}\right)}{R_f^2 C_c^2 Q} \omega^{-2-\alpha} + O\left(\omega^{-2-2\alpha}\right)$$

$$\lim_{\omega \rightarrow \infty} \omega \operatorname{Im}(Z) = \frac{1}{C_c} - \frac{\sin\left(\frac{\pi\alpha}{2}\right)}{R_f^2 C_c^2 Q} \omega^{-1-\alpha} - \frac{1}{R_f^2 C_c^3} \omega^{-2} + O\left(\omega^{-1-2\alpha}\right)$$

As a check, in the special case $\alpha=1$, we note that $\sin(\pi\alpha/2) = 1$, $\cos(\pi\alpha/2) = 0$ and $Q = C_{dl}/2$. Then these high-frequency asymptotes reduce to (2.19) and (2.21).

When α is nearly unity, we can still infer R_e and C_c from the y-intercepts of the high-frequency behavior as in the 5-element model.

The corresponding low-frequency asymptotes are

$$\lim_{\omega \rightarrow 0} \operatorname{Re}(Z) = \frac{\cos\left(\frac{\pi\alpha}{2}\right)}{Q} \omega^{-\alpha} - \frac{C_c \sin(\pi\alpha)}{Q^2} \omega^{1-2\alpha} + R_f + \dots \quad (2.23)$$

$$\lim_{\omega \rightarrow 0} \operatorname{Im}(Z) = \frac{\sin\left(\frac{\pi\alpha}{2}\right)}{Q} \omega^{-\alpha} + \frac{C_c \cos(\pi\alpha)}{Q^2} \omega^{1-2\alpha} + O\left(\omega^{1-\alpha}\right) \quad (2.24)$$

where the ordering of terms shown above assumes that $1/2 < \alpha < 1$. Truncating

after the leading term leaves $Z \rightarrow Z_{CPE}$. Then α can be inferred from the slope of the low-frequency “tail” of a Nyquist plot of $\text{Im}(Z)$ vs $\text{Re}(Z)$; this slope is:

$$\frac{d \text{Im}(Z)}{d \text{Re}(Z)} = \frac{d \text{Im}(Z)/d\omega}{d \text{Re}(Z)/d\omega} = \tan\left(\frac{\pi\alpha}{2}\right) \quad (2.25)$$

For $\alpha=1$ this slope is infinite which is consistent with (2.19) and (2.21): $\text{Re}(Z)$ becomes independent of frequency as $\omega \rightarrow 0$ (giving zero in the denominator) whereas $\text{Im}(Z)$ still depends on frequency in this limit.

The lowest-order term in (2.23) is no longer the one containing R_f [as in (2.20)] so another method must be used to infer R_f . We choose to fit the Nyquist plot at large frequencies. The experimentally observed semicircular shape is predicted by the much simpler 2-element model (2.9); in that model the diameter of the circle is R_f and its center is located at $(R_f/2, 0)$. Also the top of the semicircle corresponds to a frequency of $\Omega = 1$ or $\omega = (R_f C_c)^{-1}$. While the left-half of our experimental Nyquist plots are nearly circular, the right-half is usually distorted. Thus we choose R_f as the best-fitting diameter of the left quarter-circle of the Nyquist plot.

This leaves Q . While the low-frequency behavior of the imaginary part depends mainly on the value of Q , the two leading terms of (2.24) have nearly the same order (at least for α near to but less than unity). This complicates inferring the value of Q from (2.24). Instead, we choose to fit the phase angle of Z given

by (2.17) as a function of frequency. In particular, we chose Q as that value which minimizes the sum of the squares of the errors between the phase angles calculated from the experimentally measured impedance at each frequency and the corresponding phase angles calculated from (2.17) at the same frequencies. Since both real and imaginary parts of Z are always positive, this phase angle θ is computed simply from

$$\tan[\theta(\omega)] = \frac{\text{Im}[Z(\omega)]}{\text{Re}[Z(\omega)]}. \quad (2.26)$$

2.4 Results

2.4.1. Linearity of the response

The equivalent-circuit models of impedance represented by (2.7) and (2.12) represent linear relationships between voltage and current. While a linear response is expected if the amplitude of the applied voltage is small enough, for larger applied voltages, nonlinearities can arise if the amount of charge passed during one cycle causes variations in either the double-layer capacitance C_{dl} or the fluid resistance R_f . Such nonlinear behavior has been predicted by Freire *et al.*[22]

We checked the linearity of the response at the extremes of frequency and voltage. The current at the minimum frequency appears in Figure 2.3 for a solution of 5% OLOA 11000[®] in dodecane and sinusoidal voltages with two

different amplitudes. As expected for a linear response to a sinusoidally varying voltage, the current was also sinusoidal when the amplitude was 50 mV RMS; however, the current was periodic but not a sinusoid for 1 V RMS, which is one manifestation of a nonlinear response. Another manifestation of a nonlinear response is amplitude-dependence in the impedance spectrum; Figure 2.4 represents experiments in which a dilute solution was polarized by sinusoids of increasing amplitude. At polarizations smaller than the thermal voltage, the amplitude had no effect on either the real or imaginary parts of the impedance as expected from linear theory. In order to avoid these issues and assure linearity for the purpose of analysis, the amplitude of all impedance spectroscopy experiments was 10 mV RMS and the frequency was no smaller than 0.1 Hz.

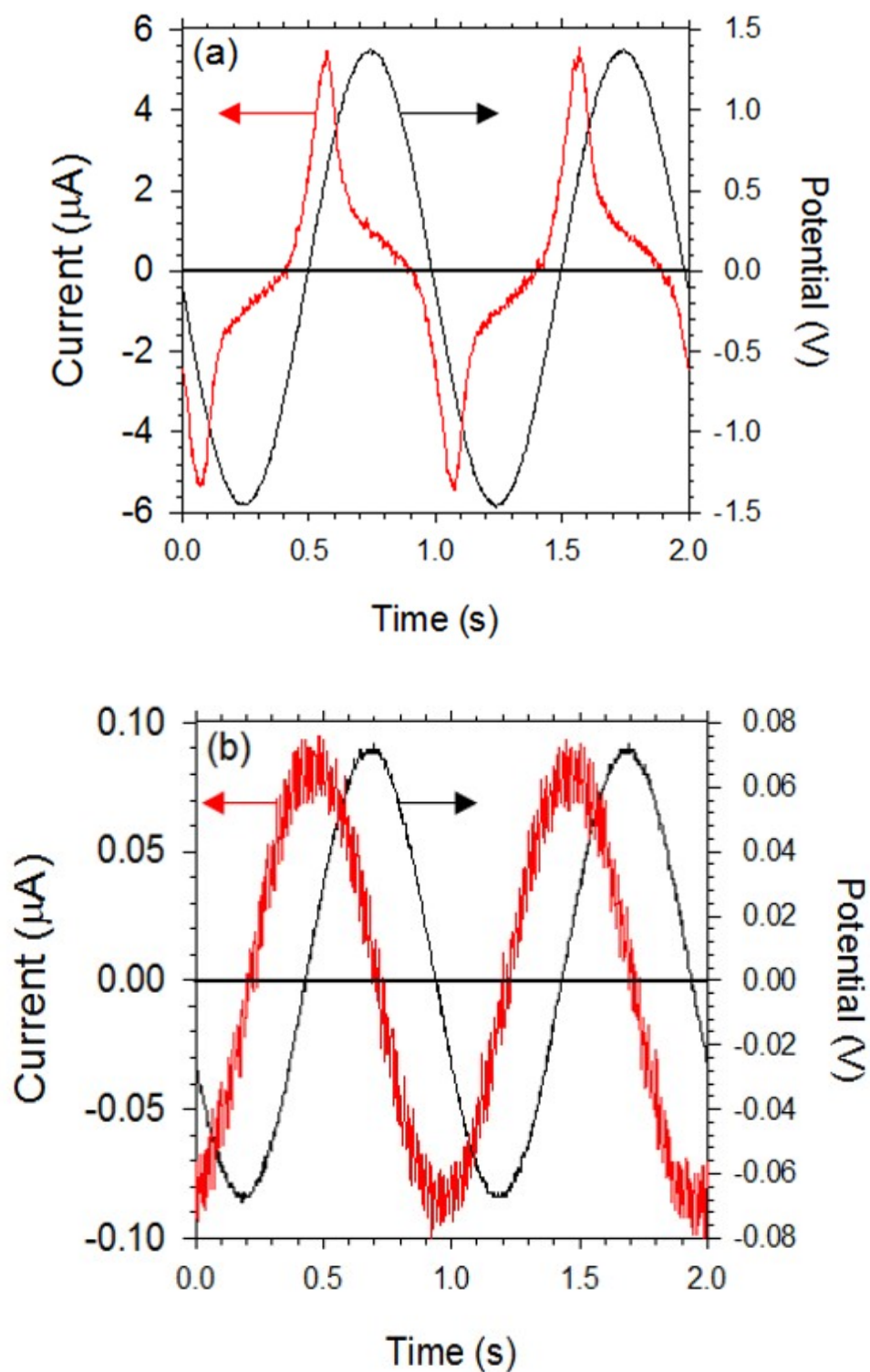


Figure 2.3. Waveforms of current (red) and potential (black) obtained with an oscilloscope in a cell filled with 5% OLOA 11000[®] in dodecane at a frequency of 1 Hz and amplitude of (a) 1 V RMS and (b) 50 mV RMS. The nonsinusoidal current waveform seen in (a) indicates nonlinear response.

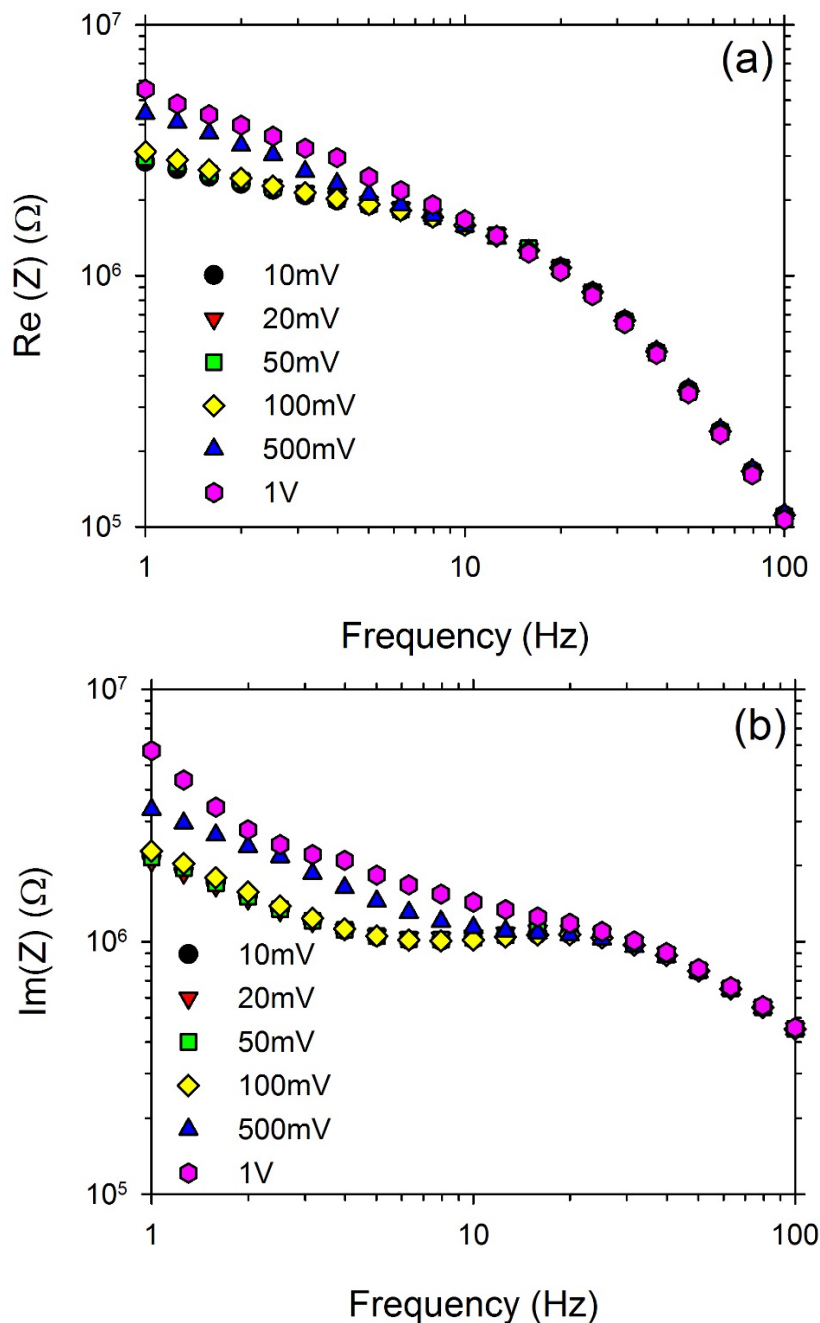


Figure 2.4. Bode plots of the real (a) and imaginary (b) parts of the impedance obtained for a sample of 0.1% weight OLOA 11000[®] in dodecane at potential amplitudes ranging from 10 mV to 1 V rms. For amplitudes below about 50 mV, the impedance is independent of amplitude, which is characteristic of a linear response.

2.4.2 Determination of equivalent circuit elements

According to the asymptotic analysis summarized by (2.19) – (2.22), the asymptotes at high and low frequencies are simply related to the four parameters of the five-element model given by (2.12). These asymptotes and their associated significance are summarized by the annotated horizontal dashed lines in the sample Bode plots in Figure 2.5. In particular, R_e and C_c are directly given by the high-frequency asymptotes of the real and imaginary parts, respectively. Once C_c has been determined, the low-frequency asymptote of the imaginary part yields C_{dl} . Knowing C_c and C_{dl} , we can calculate their ratio α ; then the low-frequency asymptote of the real part yields R_f . Thus we determined $R_e = 124 \, \Omega$, $C_c = 3.61 \, \text{nF}$, $C_{dl} = 540 \, \text{nF}$ and $R_f = 55.6 \, \text{k}\Omega$ for the 10wt% OLOA.

Using these values of the four parameters to calculate the impedance spectra from (2.13) and (2.14) yields the red curves in Figure 2.5. The fit is good over the entire range of frequencies for the 10wt% OLOA, but significant deviations are evident in both low-frequency asymptotes for 0.1wt% OLOA. Indeed the real part of the impedance appears to increase continuously as $\omega \rightarrow 0$ rather than reach a plateau as predicted by (2.20). This was the motivation to turn to the constant-phase element model frequently employed in the analysis of electrochemical impedance spectra.

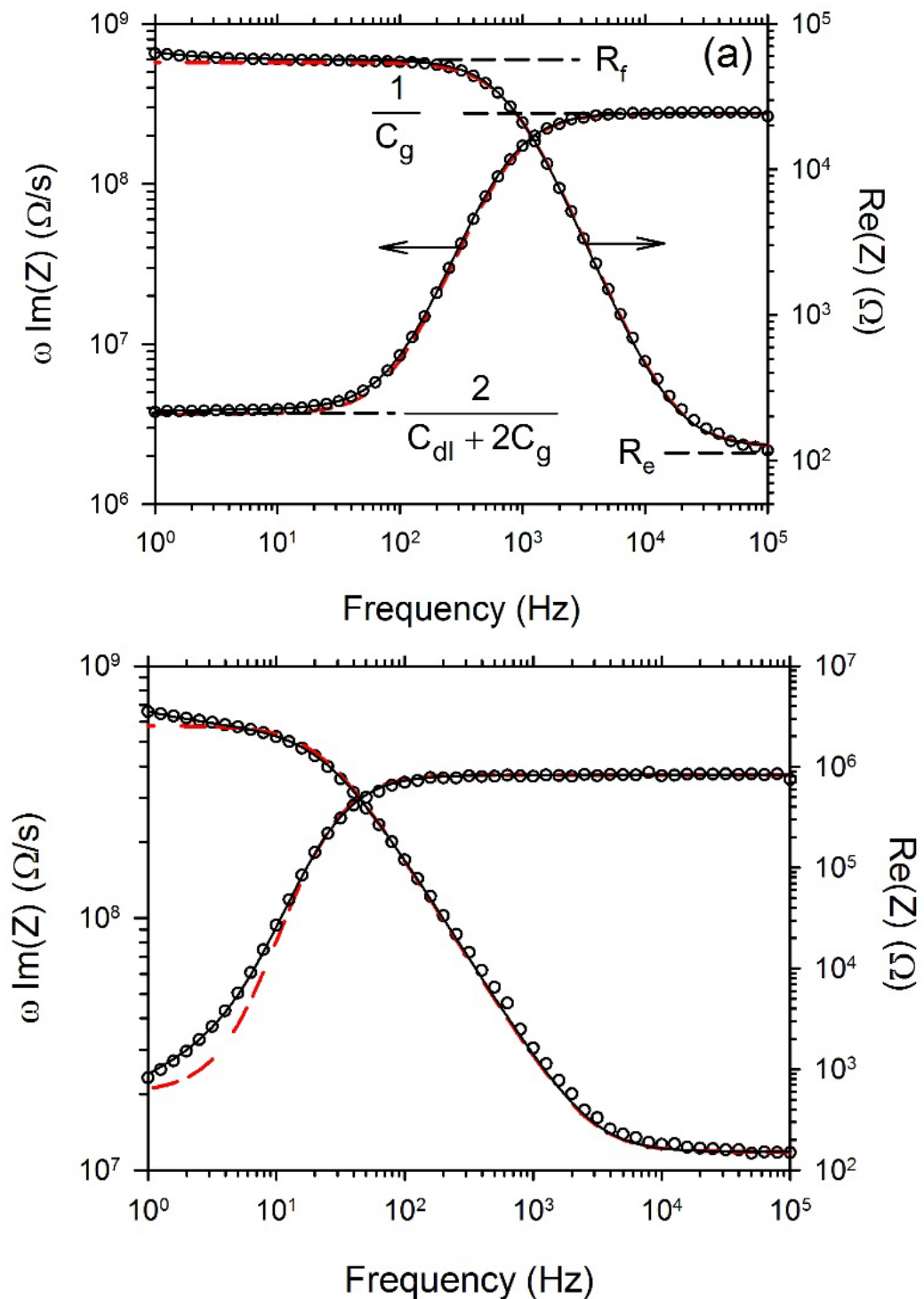


Figure 2.5. Impedance spectra for 10wt% OLOA 11000(a) and for 0.1wt% OLOA 11000[®] (b). Horizontal dashed lines denote asymptotes expected from the 5-element circuit model of Figure 2.2b. Points represent experimental data, dashed red curve is best-fitting 5-element model and solid black curve is best-fitting CPE model.

The constant-phase element model is represented by (2.16) and (2.17). Instead of a single parameter C_{dl} representing the double-layer capacitance, the constant-phase element Z_{CPE} (which replaces it) contains two parameters Q and α . We first determined α using a Nyquist plot like that shown in Figure 2.6. According to (2.25), in the limit of low frequencies (where the real part is largest), the Nyquist plot should become linear with a slope which depends solely on the parameter α . The data points of Figure 2.6 for large real parts do seem to approach a straight line. Thus α was determined to be 0.79 for 0.1wt% OLOA.

Since $\text{Re}(Z)$ does not approach a plateau at low frequency in Figure 2.5b, we cannot reliably use (2.20) to infer R_f . However, we note that the left-half [i.e. frequencies larger than $(R_f C_c)-1$] of the Nyquist plot shown in Figure 2.6 resembles a quarter circle, as expected from the simpler two-element model of (2.9). According to the 2-element model, the diameter of the quarter circle is simply R_f . Thus R_f was determined to be 2.74 M Ω for the 0.1wt% OLOA.

The only remaining parameter is Q which was obtained from a least-squares fit of the CPE model (2.17) to the experimental phase angle data calculated from (2.26) and shown as the points in Figure 2.7. The value of C_{dl} is then calculated from (2.18) as 93 nF. With all the parameters now evaluated, we can use the CPE model to predict the black curves in Figure 2.5 through Figure 2.7. With C_{dl} and R_f known, we can also use the 5-element model to predict the red curves in Figure 2.5 through Figure 2.7. Clearly, the CPE model gives a better fit than the 5-

element model in all cases. So we will use parameters determined by fitting this model to infer the fluid properties below.

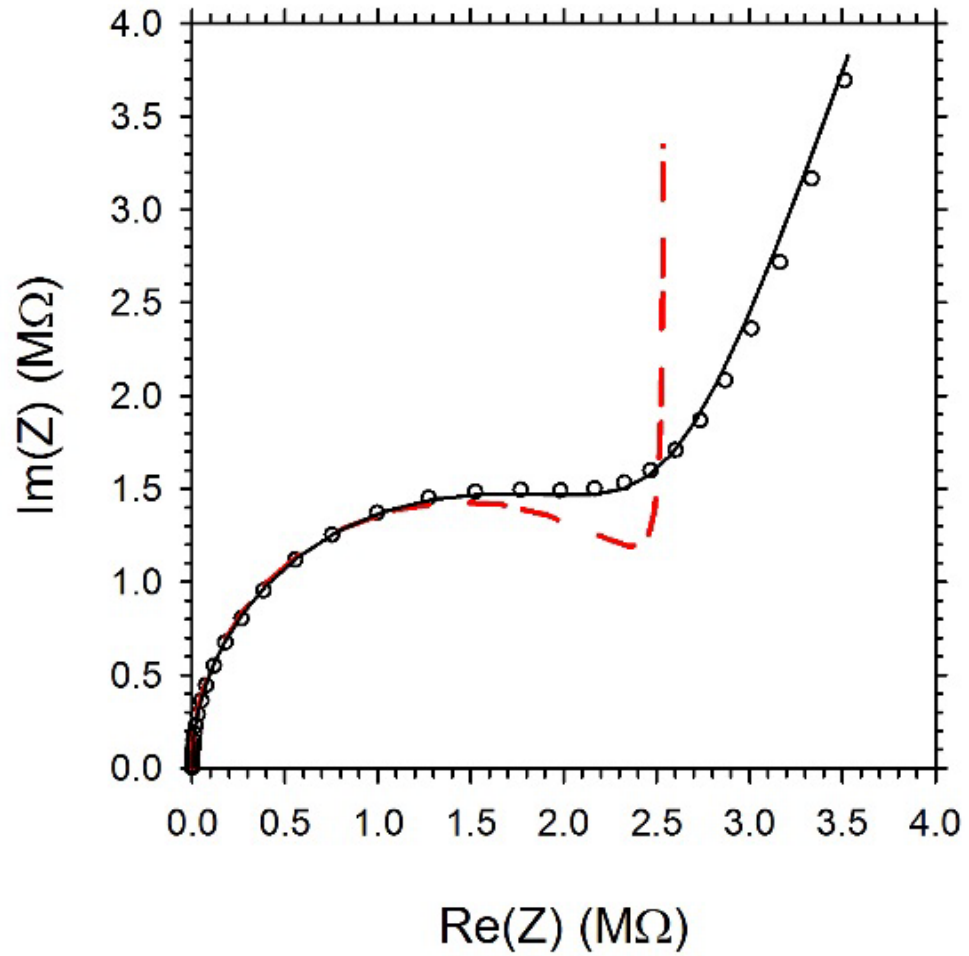


Figure 2.6. Nyquist plot of impedance spectra for 0.1wt% OLOA 11000. Points represent experimental data, dashed red curve is the best-fitting 5-element model and the solid black curve is best-fitting CPE model. The slope of the black dashed line is used to estimate α from (2.25).

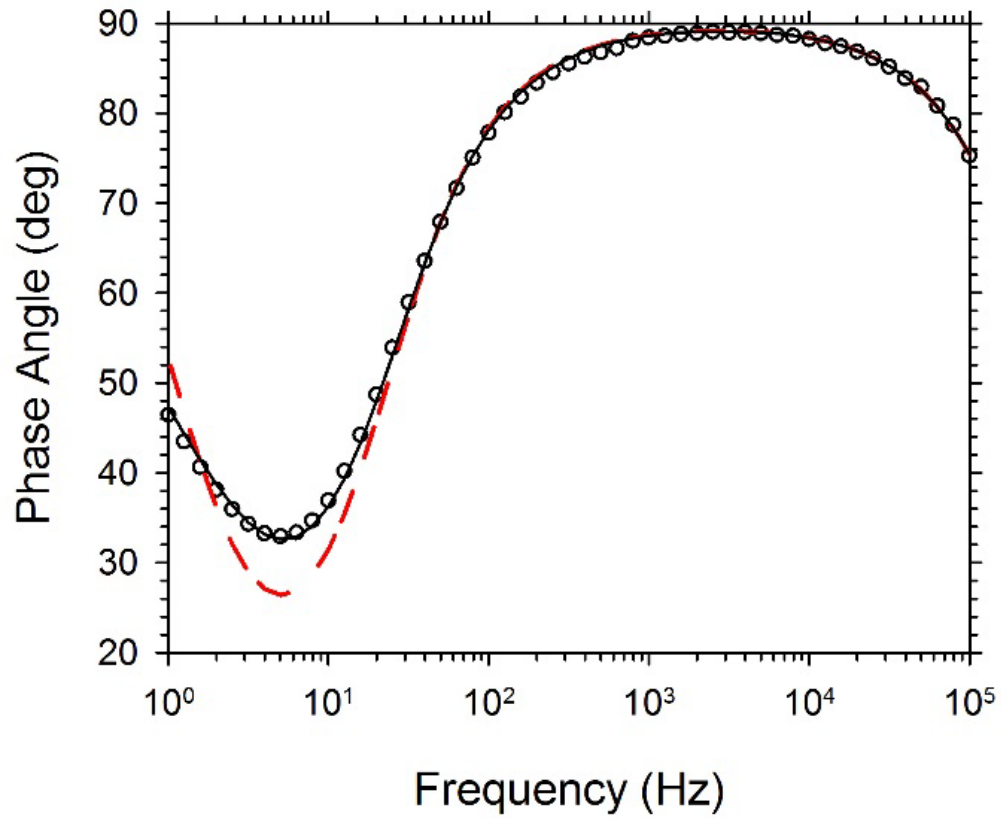


Figure 2.7. Phase angles calculated from 0.1wt% experimental data using (2.26) and plotted as points. The value of parameter Q is obtained from a least-squares fit of points to the CPE model, shown as the solid curve. After calculating C_{dl} from (2.18), the four-element model can be evaluated and is shown as the red dashed curve.

2.4.3 The effect of varying concentration

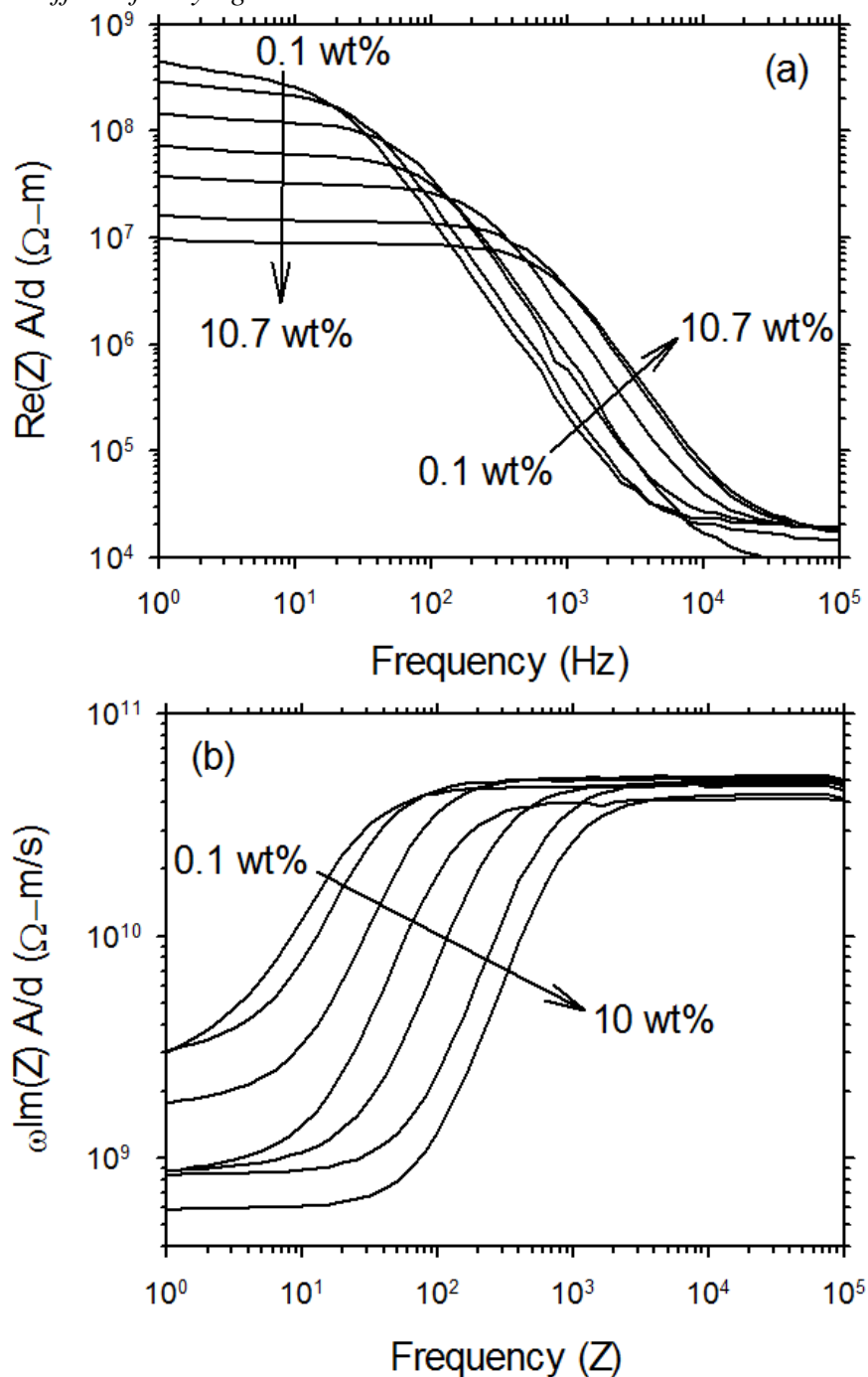


Figure 2.8. Bode plots of (a) the real part and (b) the frequency times the imaginary part of the impedance at various concentrations of OLOA 11000® in dodecane. The impedances have been weighted by cell constant A/d to remove that variation. Curves correspond to 0.1, 0.18, 0.5, 1, 2.6, 5, 7.5 and 10.7 wt% OLOA.

Bode plots for representative spectra of all the mixtures appear in Figure 2.8. The overall effects of concentration are apparent. First, the real part of the impedance at low frequency decreased as the concentration of OLOA 11000[®] increased. The maximum in the imaginary part of the impedance in the high frequency range shifted from lower frequencies to higher frequencies for higher concentrations OLOA 11000. Likewise the frequency of the minimum in the imaginary part shifted from lower values to higher values as the concentration of OLOA 11000[®] increased.

2.4.4 Fluid properties found from equivalent circuit elements

Figure 2.9 summarizes the fluid conductivities calculated from the fluid resistance R_f according to (2.2). Obtaining each point involved reassembling the fluid cell which alters slightly the geometry. The fluid gap d ranged from 9.7 to 17.1 μm with an average of 10.8 μm while the wetted fluid area A_f ranged from 8.8 to 15.4 cm^2 with an average of 14.0 cm^2 . Previous studies with OLOA 11000[®] have found the conductivity to be proportional to the weight percent.[23] The solid line drawn on Figure 2.9 has a slope of unity, which fits well the results at moderate concentrations. But the conductivity at the lowest concentrations lie above this line while the conductivity at the highest concentration lies below. The best fitting straight line (including all the points) has a slope of 0.831 ± 0.025 .

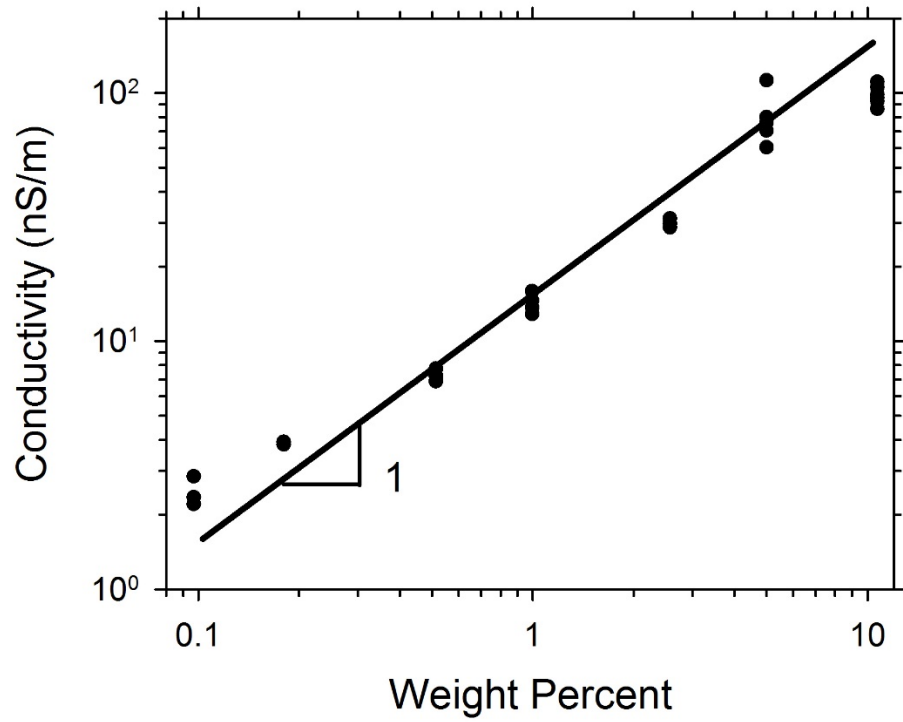


Figure 2.9. The conductivity of OLOA 11000[®] in dodecane.

The fluid's electric permittivity ϵ_f was inferred from the cell capacitance C_c using (2.4). Dividing this by the permittivity of vacuum ϵ_0 gives the fluid's dielectric constant. Results for various OLOA concentrations are shown in Figure 2.10. Values ranged from 2.0 to 2.6 but no systematic dependence on surfactant concentration is evident. The mean and standard deviation of all measurements are 2.25 ± 0.18 . The dielectric constant of pure dodecane is reported as 2.01,[24] which is within 1.3 standard deviations of the mean.

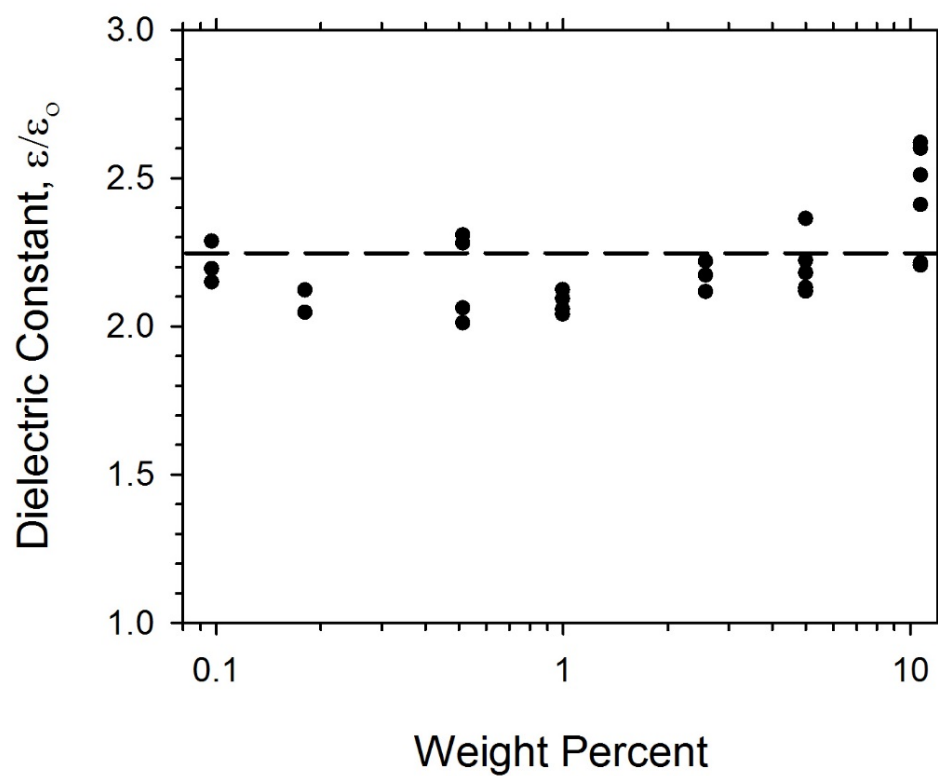


Figure 2.10. The dielectric constant of the fluid is found to be independent of the concentration of OLOA 11000. The average dielectric constant found for all the measurements was 2.25 ± 0.18 , shown as the solid line.

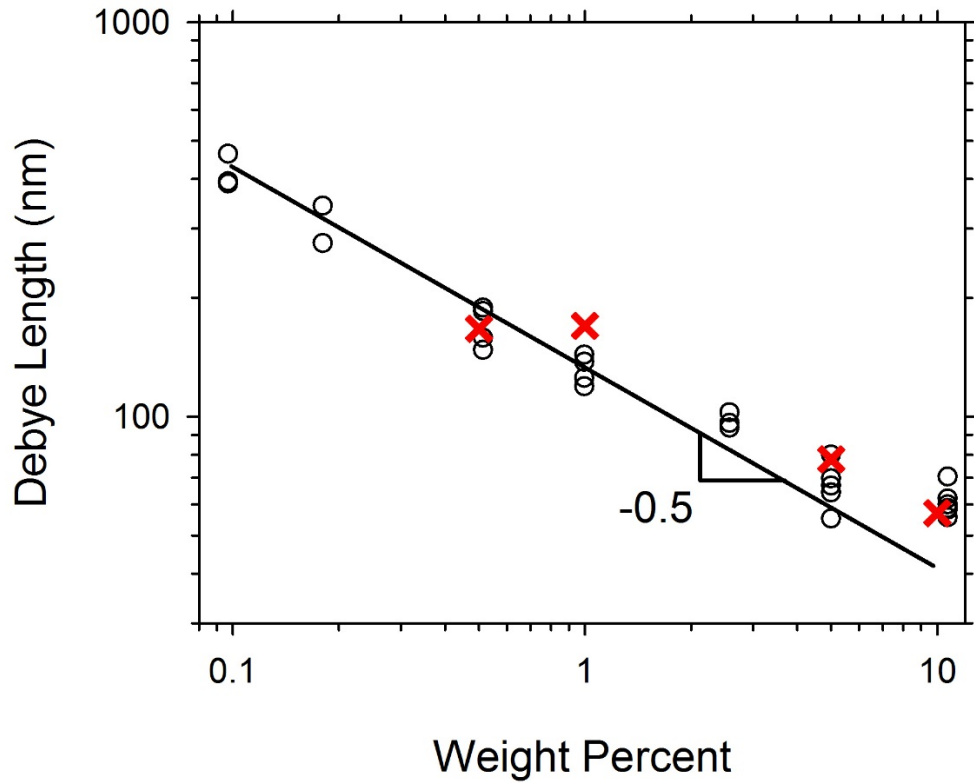


Figure 2.11. Comparison of Debye lengths inferred either from C_{dl} using the CPE model (○) or from TIRM experiments (×) performed on a different grade of surfactant, OLOA 1200.[12] The straight line was drawn with a slope of -0.5 .

We calculated the double layer capacitance C_{dl} from the parameters Q and α of the CPE model using (2.18) and then inferred the Debye length λ_D according to (2.11). The results are shown in Figure 2.11. Also included for comparison in Figure 2.11 are the Debye lengths measured with TIRM by Prieve *et al.*[12] These TIRM experiments used a different grade of OLOA (371 versus 11000) which is a slightly less concentrated version of the same dopant.[17] Nonetheless the good agreement between the two sets at least suggests that the application of (2.18) does indeed lead to the double-layer capacitance. Notice that the Debye lengths appear to be inversely proportional to the square-root of surfactant

concentration as expected from the Gouy-Chapman theory (2.10) if the fraction of the OLOA which is charged is independent of total concentration.

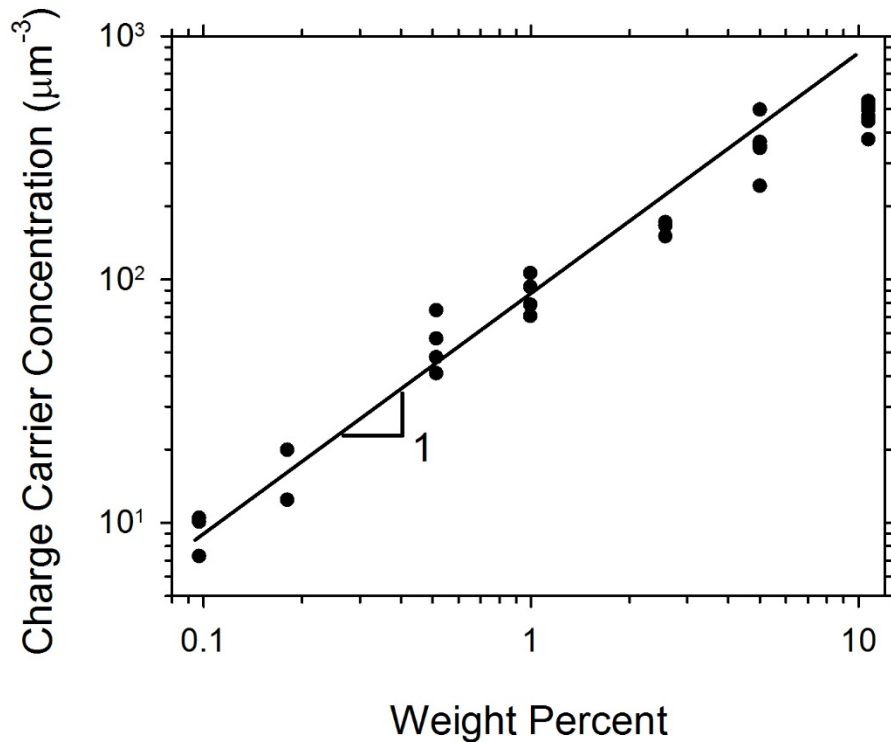


Figure 2.12. The concentration of charge carriers is proportional to the total concentration of surfactant, except possibly at the highest concentration.

The real value of having a value for Debye length is that it can be used to infer the ionic strength n_0 of the solution. Using (2.10) we converted the Debye lengths into the ionic strengths shown in Figure 2.12. If we assume that charge carriers are univalent, then ionic strength equals the number concentration of charge carriers. Dividing the total mass concentration of surfactant by an average molecular weight of 1200, then multiplying the result by Avogadro's number, we can infer the total number concentration of OLOA molecules. The line drawn on

Figure 2.12 corresponds to 17 ppm of all surfactant molecules being charged. In other words, 17 out of every million surfactant molecules are positively charged; an equal number are negatively charged.

Assuming a 1-1 electrolyte with equal ion mobilities $D/k_B T$, the fluid conductivity is

$$K = \frac{2n_0 e^2 D}{k_B T} . \quad (2.27)$$

Knowing the number concentration of charge carriers, n_0 , we can use (2.27) to convert the measured conductivities into the diffusion coefficient of the charge carriers. Figure 2.13 summarizes the diffusion coefficients inferred from (2.27) using the conductivities of Figure 2.9 and the number concentrations of Figure 2.12. Although the diffusion coefficient appears to increase monotonically with concentration from $10 \mu\text{m}^2/\text{s}$ at 0.5 wt.% to $20 \mu\text{m}^2/\text{s}$ at 10 wt.%, this factor of two increase is no larger than the factor of two variation observed when reproducing the diffusion coefficient at a given concentration. Moreover, the trend with concentration does not include two lowest concentration. Thus we conclude that no systematic variation of diffusion coefficient with concentration of OLOA 11000[®] is observed. The average diffusion coefficient of charge carriers is $16 \pm 4 \mu\text{m}^2/\text{s}$. The average diffusion coefficient of charge carriers corresponds to a hydrodynamic diameter of $20 \pm 5 \text{ nm}$ using the Stokes-Einstein relationship

assuming a viscosity of 1.34 cP for dodecane. The light scattering intensity distribution versus hydrodynamic diameter of a 0.1 wt.% OLOA 11000[®] in dodecane is shown in Figure 2.14. The average diameter of reverse micelles is significantly smaller than the boxed area representing the measured diameter of charge carriers found by EIS indicating that light scattering alone is not an accurate approximation to infer the size and mobility of charge carriers.

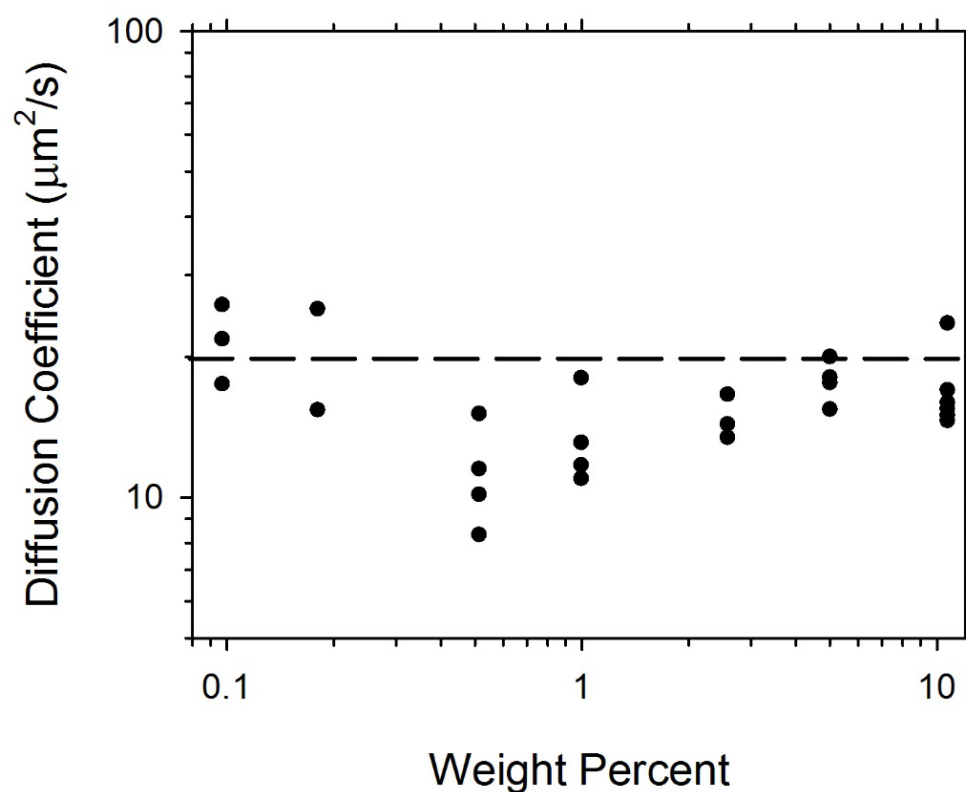


Figure 2.13. The diffusion coefficient of charge carriers inferred from conductivity and charge carrier concentration.

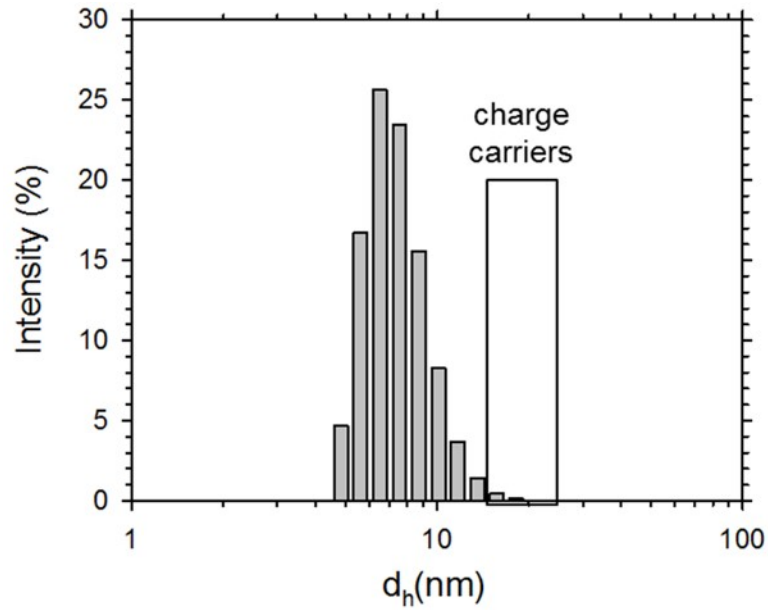


Figure 2.14: The hydrodynamic diameter of 0.1% weight OLOA 11000® in dodecane found by phase analysis light scattering. The hydrodynamic diameter of charge carriers as calculated from the diffusion coefficients found for all concentrations of OLOA 11000® in dodecane is highlighted in the boxed area.

2. 5 Discussion

The question underlying this study was what can be learned about charge carriers in doped nonpolar media from impedance spectroscopy measurements. The answer appears to be conductivity, permittivity and double-layer capacitance of the solution. Fluid resistance R_f is inferred from the radius of the left quarter circle of the Nyquist plot obtained at high frequencies (see Figure 2.6) and the fluid conductivity K is calculated from (2.2). The geometric capacitance C_c is inferred from the asymptotic behavior at high frequency of the imaginary part of the impedance (see Figure 2.5) and then the permittivity is calculated from (2.4). Commercial instruments are also available for measuring the very low

conductivity and permittivity of doped nonpolar liquids.[25, 26] Commercial meters usually employ a conductivity cell requiring about 10 ml of sample. One potential advantage of the thin-cell used in the current work is that only about 10 μl of liquid is required.

The main novelty of the current chapter is the application of impedance spectroscopy to deduce the double-layer capacitance of doped nonpolar liquids. Assuming the zeta potential of the electrodes is comparable to or smaller than the thermal voltage $k_B T/e$, the measured double-layer capacitance can be used to infer the Debye length λ_D from (2.11) and in turn the ionic strength n_0 can be inferred from (2.10). Further assuming univalent charge carriers, the ionic strength also equals the concentration of charge carriers. Measurements of the charge-carrier concentration versus the total concentration of surfactant offer important clues regarding the mechanism for formation of charge-carriers.

For example, the direct proportionality seen in Figure 2.12 supports the disproportionation hypothesis that micelles of the surfactant become charged as a result of proton transfer occurring during a collision between two neutral micelles.[2, 12, 27-31] The mass-action law for the disproportionation model leads to a prediction that the fraction of micelles which are charged is independent of the total concentration of micelles; then conductivity is proportional to concentration over the entire range. By contrast, the mass-action law for dissociation of ion pairs leads to the prediction that the conductivity is

proportional to the total concentration only for concentrations which are small compared to the equilibrium dissociation constant; at the opposite extreme of much higher concentrations, the dissociation model predicts that conductivity is proportional to the square-root of concentration.

Potentially a more direct method of determining the charge carrier concentration (compared to double-layer capacitance) is to measure the total charge which must be passed through the cell in a potentiostatic experiment in order to exhaust all charge carriers from the bulk solution and reach zero current.[31] However, there are a couple of complications. First, the current does not always decay to zero: neutral micelles continue to collide and form new charged micelles and cause a persistent current at long times.[9, 11] Second, the sudden application of a constant voltage causes a singularity in current which is difficult to measure accurately; some of this initial current charges the geometric capacitor (item C_c in Figure 2.2b). This portion of the current does not pass through the fluid and should not be counted when determining the charges in the fluid.

Let's assume these complications can be overcome. Then dividing this total initial charge contained by the fluid by the volume of the cell and by the elemental charge e yields the concentration of carriers (if univalent). This total charge is proportional to the charge per carrier. By contrast the ionic strength (deduced from the double-layer capacitance) is proportional to the charge squared

per carrier. Agreement between the carrier concentrations inferred from these two methods would support the assumption of univalent carriers. Disagreement might be reconciled by allowing nonunivalent carriers.

2.5.1 The CPE Model

In order to fit well the measured impedance spectrum at moderate to low frequencies (at which double-layer capacitance contributes significantly), we must use the CPE model (2.17); the 5-element model (2.12) (in which a simple capacitor is used in place of the CPE to represent the double layer) could not be made to fit well at smaller concentrations of surfactant (see Figure 2.5b).

The CPE is an empirical formula for impedance (2.16) which leads to impedance spectra resembling those measured in many circumstances.[16] Most often it represents elements characterized by a distribution of time constants, instead of just one time constant. For example, a circuit consisting of a simple resistor R in parallel with a simple capacitor C displays a single characteristic time constant RC [see (2.7) and (2.8)]. A simple capacitor might be two parallel plates of area A separated by a distance d which corresponds to $C = \epsilon A/d$ where ϵ is the permittivity of dielectric material between the plates. Now suppose the two plates are not parallel; or suppose one of the plates is a curved surface. Now the plate separation d is not a single value but rather takes on a distribution of values. In turn this leads to a distribution of capacitance values and a distribution of characteristic times. The symbol used for CPE in a circuit diagram is $-|(-$

(suggesting a curved electrode) whereas a simple capacitor is represented by $-||-$ (for two parallel planes).

Owing to a distribution in the diameter of silica spheres used for spacers in our cell, we likely have some distribution in electrode spacing which is one possible source of CPE behavior. However, it is not the geometric capacitor C_c which is being represented as a CPE in (2.17); rather it is the double-layer capacitor C_{dl} . A distribution in spacing would also lead to a distribution in fluid resistances R_f . An increase in spacing increases the resistance and decreases the geometric capacitance such that the time constant $R_f C_c$ is independent of spacing. But a distribution of spacing would lead to a distribution in values for the $R_f C_{dl}$ time constant, which is one source of CPE behavior.

A nonuniform ζ over the surface of the ITO electrodes (in the absence of any applied voltage) is another possible source of CPE behavior in these experiments. If ζ is everywhere small compared to the thermal voltage $k_B T/e$ (as we have assumed), then (2.11) continues to predict a single value for C_{dl} . But if ζ is not small, then (2.11) would predict a distribution in capacitance values, which is a second source of CPE behavior.

After fitting the CPE model to the measured impedance spectrum, (2.18) is used to infer a value for C_{dl} . Equation (2.18) is derived[16] by considering the

impedance of a resistor R_f in series with the double-layer capacitor, with the latter represented by a CPE using (2.16):

$$Z_f = R_f + Z_{CPE} = R_f + Q^{-1} \left(\frac{i}{\omega} \right)^\alpha$$

This sum might be considered the impedance of the fluid as a whole (the electrically neutral bulk plus the two counter ion clouds, one on each electrode). The frequency dependence of this impedance can also be written as

$$Z_f = \left[1 + \left(\frac{i}{\omega\tau} \right)^\alpha \right] R_f$$

where $\tau = (R_f Q)^{1/\alpha}$

is a characteristic time constant for Z_f . Interpreting τ as $(1/2)R_f C_{dl}$, then solving for C_{dl} leads to (2.18). This interpretation for τ is discussed at some length by Brug *et al.*[19] who recommend it in the case of ideally polarizable electrodes (no Faradaic reactions). The later IUPAC recommendations[16] (written by one of the same authors) do not include this recommendation. However more recent studies continue to use (2.18).[20] Indeed the resulting Debye lengths of Figure 2.11 agree remarkably well with those determined independently using TIRM (although the latter employ a different grade of OLOA). This agreement tends to confirm the validity of (2.18).

2.5.2 EIS and a thin cell

The use of a thin cell offered two advantages. First, the relatively low resistance of a thin cell used with a nonpolar fluid allowed currents of tens of nanoamperes to flow even at low concentrations and low applied potentials, currents that were easily measured by the potentiostat.

Second, the thin cell permitted the determination of double-layer capacitance at higher frequencies than would be required for thicker cells. To have the impedance of the capacitor C_{dl} dominate that of the resistor R_f in series with it (recall Figure 2.2b), the frequency must be smaller than $(R_f C_{dl})^{-1}$. However, because of the presence of the second capacitor C_c in the circuit, the frequency does not need to be this small to determine C_{dl} — the frequency just needs to be small enough so that the combined impedance of the two capacitors dominates that of the resistor. Then the asymptotic behavior of impedance at low frequency allows the combined capacitance to be determined. This asymptotic behavior is given by (2.22).

Requiring the second term of (2.22) to be negligible compared with the first, requires

$$\omega \ll \sqrt{\frac{2C_c}{C_{dl}}} \left(1 + \frac{2C_c}{C_{dl}} \right) \frac{1}{R_f C_c} \approx \sqrt{\frac{2\lambda_D}{d}} \frac{K}{\epsilon}$$

To obtain the second equality above, we substituted (2.2) and (2.11) and have approximated (2.4) by $C_c \approx \epsilon A_f/d$; we also assumed $\lambda_D \ll d$ which is valid for all the λ_D reported in Figure 2.11, despite having a small value for d . The main implication of this inequality is that thinner cells (smaller d) allow determination of the double-layer capacitance at higher frequencies. For example, the frequency is an order of magnitude larger for a 10 μm cell than for a 1 mm cell.

2.5.3 The time constants of a polarized cell

Finally, we point out that this study indicated that two main time constants must be kept in mind when designing cells that use nonpolar media. The first time constant can be called the geometric time $\tau_g = R_f C_c$ because it is the product of the cell resistance and the geometric capacitance. For $\omega \tau_g \gg 1$, the impedance of the cell is dominated by geometric capacitor; no significant charge accumulates in the double layers. The second time constant is the double-layer time $\tau_{dl} = R_f C_{dl}$ because it is the product of the cell resistance and the surface capacitance. At $\omega \tau_{dl} = 1$ enough charges are accumulating in the double layers that the voltage drop across them is comparable to the voltage across the electrically neutral bulk solution.

2.6 Conclusions

The main result of this contribution is that impedance spectroscopy can be used to infer the differential double-layer capacitance which in turn can be used to

calculate the Debye length and the charge carrier concentration. At high concentrations of dopant, the double-layer capacitance can be represented by a simple electric circuit capacitor. But at low concentrations, the low-frequency asymptotic behavior of the impedance spectrum cannot be well represented by a simple capacitor. A constant-phase element [see (2.16)] must be used instead. The two parameters of the CPE (Q and α), together with the fluid resistance R_f are then used to calculate the double-layer capacitance from (2.18) and the Debye length λ_D from (2.11). Debye lengths thus determined agree reasonably well with those measured independently by TIRM, which tends to justify this method.

2.7 Acknowledgement

We gratefully acknowledge financial support for this project from the Dow Chemical Company.

2.8 References

1. Klinkenberg, A. and J.L. van der Minne, *Electrostatics in the Petroleum Industry: The Prevention of Explosion Hazards*. 1958, New York: Elsevier.
2. Morrison, I.D., *Electrical charges in nonaqueous media*. Colloids and Surfaces A: Physicochemical and Engineering Aspects, 1993. **71**: p. 1-37.
3. Chen, Y., et al., *Flexible active-matrix electronic ink display*. Nature, 2003. **423**: p. 136.
4. Novotny, V., *Applications of Nonaqueous Colloids*. Colloids and Surfaces A: Physicochemical and Engineering Aspects, 1987. **24**: p. 361-375.

5. Guo, Q., V. Singh, and S.H. Behrens, *Electric charging in nonpolar liquids because of nonionizable surfactants*. Langmuir, 2010. **26**(5): p. 3203-7.
6. Espinosa, C.E., et al., Particle charging and charge screening in nonpolar dispersions with nonionic surfactants. Langmuir, 2010. **26**(22): p. 16941-8.
7. Schmidt, J., et al., Conductivity in nonpolar media: experimental and numerical studies on sodium AOT-hexadecane, lecithin-hexadecane and aluminum(III)-3,5-diisopropyl salicylate-hexadecane systems. J Colloid Interface Sci, 2012. **386**(1): p. 240-51.
8. Poovarodom, S. and J.C. Berg, Effect of particle and surfactant acid-base properties on charging of colloids in apolar media. J Colloid Interface Sci, 2010. **346**(2): p. 370-7.
9. Beunis, F., et al., Inverse micelles as charge carriers in nonpolar liquids: Characterization with current measurements. Current Opinion in Colloid & Interface Science, 2013. **18**(2): p. 129-136.
10. Karvar, M., et al., Transport of Charged Aerosol OT Inverse Micelles in nonpolar Liquids. Langmuir, 2011. **27**: p. 10386-10391.
11. Beunis, F., et al., *Electric charging of inverse micelles in a nonpolar liquid with surfactant*. Colloids and Surfaces A: Physicochemical and Engineering Aspects, 2014. **440**: p. 10-19.
12. Prieve, D.C., et al., Two Independent Measurements of Debye Lengths in Doped Nonpolar Liquids. Langmuir 2008. **24**: p. 1120-1132.
13. Novikov, G.F., et al., *The impedance of solutions of AOT/water micelles in hexane*. Russian Journal of Physical Chemistry A, 2007. **81**(12): p. 2030-2034.
14. Goual, L., Impedance Spectroscopy of Petroleum Fluids at Low Frequency. Energy & Fuels, 2009. **23**: p. 2090-2094.
15. Orazem, M.E. and B. Tribollet, *Electrochemical Impedance Spectroscopy*. 2008, Hoboken, NJ: Wiley.
16. Sluyters-Rehbach, M., Impedances of Electrochemical Systems: Terminology, Nomenclature and Representation. Part I. Pure & Applied Chemistry, 1994: p. 1831-1891.

17. Parent, M.E., et al., Influence of surfactant structure on reverse micelle size and charge for nonpolar electrophoretic inks. *Langmuir*, 2011. **27**(19): p. 11845-51.
18. Hunter, R.J., *Foundations of Colloid Science*. Vol. 1. 1987, Oxford: Clarendon Press.
19. Brug, G.J., et al., The Analysis of Electrode Impedances Complicated By the Presence of a Constant Phase Element. *Journal of Electroanalytical Chemistry*, 1984. **176**: p. 275-295.
20. Orazem, M.E., et al., *Dielectric Properties of Materials Showing Constant-Phase-Element (CPE) Impedance Response*. *Journal of the Electrochemical Society*, 2013. **160**(6): p. C215-C225.
21. Duarte, A.R., et al., Electric impedance of a sample of dielectric liquid containing two groups of ions limited by ohmic electrodes: a study with pure water. *J Phys Chem B*, 2013. **117**(10): p. 2985-91.
22. Freire, F., G. Barbero, and M. Scalerandi, *Electrical impedance for an electrolytic cell*. *Physical Review E*, 2006. **73**(5).
23. Gacek, M., et al., Effects of trace water on charging of silica particles dispersed in a nonpolar medium. *Langmuir*, 2012. **28**(31): p. 11633-8.
24. Wohlfarth, C., Permittivity (dielectric constant) of liquids in *The Handbook of Chemistry and Physics*, 87th ed., D.R. Lide, Editor. 2004, CRC Press: Boca Raton, FL. p. 06-188.
25. Briscoe, W.H. and P. Attard, *Counterion-only electrical double layer: A constrained entropy approach*. *The Journal of Chemical Physics*, 2002. **117**(11): p. 5452.
26. Dukhin, A.S. and P.J. Goetz, How non-ionic "electrically neutral" surfactants enhance electrical conductivity and ion stability in non-polar liquids. *Journal of Electroanalytical Chemistry*, 2006(588): p. 44-50.
27. Kim, J., et al., Ionic Conduction and Electrode Polarization in a Doped Nonpolar Liquid. *Langmuir*, 2005. **21**: p. 8620-8629.
28. Strubbe, F., et al., *Generation current of charged micelles in nonaqueous liquids: measurements and simulations*. *Journal of Colloid and Interface Science*, 2006. **300**(1): p. 396-403.

29. Roberts, G.S., et al., Electrostatic Charging of Nonpolar Colloids by Reverse Micelles. *Langmuir*, 2008. **24**: p. 6530-6541.
30. Beunis, F., et al., *Dynamics of charge transport in planar devices*. *Physical Review E*, 2008. **78**.
31. Kornilovitch, P. and Y. Jeon, *Transient electrophoretic current in a nonpolar solvent*. *Journal of Applied Physics*, 2011. **109**(6): p. 064509.

Chapter 3 Determination of charge carrier concentration in doped nonpolar liquids by impedance spectroscopy in the presence of charge adsorption

3.1 Introduction

Nonpolar liquids such as alkanes have virtually no conductivity, but the addition of surfactants can produce measurable conductivity.[1] For example, practitioners add surfactants to highly refined hydrocarbons to mitigate charge accumulation during transfer of the liquid from one vessel to another, which reduces the risk of ignition by arcing. More recently the addition of surfactants as charge inducing dopants has been used to stabilize particle dispersions electrostatically. For example, adding the commercial surfactant OLOA 11000[®] (poly-isobutylene succinimide) to engine oils suspends soot particles and prevents the buildup of sludge.[2] Other applications include electrophoretic ink displays[3] and printing inks.[4, 5] Aerosol-OT[®] (dioctyl sodium sulfosuccinate), another widely studied dopant, includes an ionic head group[6-10], but ionic groups are not necessary. Even nonionic surfactants including Span[®] 85 (sorbitan trioleate), Span[®] 80 (sorbitan monooleate), and Span[®] 20 (sorbitan monolaurate) raise the electrical conductivity of nonpolar liquids.[11-15]

Various mechanisms have been proposed to explain the stabilization of charge by surfactants in nonpolar media. Amphiphilic surfactants form reverse micelles that display their nonpolar tails to the host liquid while providing a polar core to host the charge. Collisions of two neutral micelles may result in the transfer of a proton (or other small ion). The interaction creates an ion pair, whose subsequent degree of dissociation is determined by the resulting electrostatic attraction relative to the thermal energy $k_B T$. Ionic surfactants might dissociate to some extent to produce separately charged entities. Nonionic surfactants might solubilize and dissociate ionic contaminants present in the solvent, dopant, and surfaces. Finally, because the concentration of charge carriers is extremely small, even alcohols — which would be considered nonionic among aqueous electrolytes — can donate or accept protons to a very limited extent and thus impart conductivity to solutions with nonpolar solvents [16]. Perhaps the “nonionic” Span[®] surfactants work similarly.

The concentration of charged species, however produced and stabilized, is an important quantity for any combination of host liquid and surfactant. For example the Debye screening length in the liquid phase, a crucial length scale governing stability of dispersions by electrostatic repulsion, depends on the inverse square root of this concentration. Conductivity, the most commonly measured property of doped nonpolar liquids, is directly proportional to the charge carrier concentration but also is inversely proportional to carrier size. Thus, conductivity

measurements themselves do not yield the desired charge concentration. Previous studies solved this problem by inferring the charge carrier size from dynamic light scattering, [4, 6] but this determination requires the assumption that the charged carriers and the scatterers have the same size, which might not be true [17]. Alternatively, one can determine the Debye length by measuring the exponential decay of double-layer repulsion [18], but that experiment is more challenging than an electrical measurement.

Electrochemical techniques have been employed to determine the concentration of charge carriers. Fitting numerical simulations to the data of a chronocoulometric experiment is one approach [19, 20], or one can integrate the current with time to determine the total charge available [18, 19, 21, 22]. Dividing this charge by the volume of fluid gives the initial concentration of carriers, but persistent “surface current” can complicate this analysis [14, 23, 24]. Experiments based on electrochemical impedance spectroscopy (EIS) [6, 9, 17] have also been used. We used EIS to measure conductivity and double layer capacitance of nonpolar liquids [17] and thereby deduce Debye lengths for various concentrations of the surfactant OLOA 11000[®] in dodecane. The impedance spectra exhibited classic semicircular behavior in Nyquist plots at higher frequencies and purely capacitive behavior, as modified by constant phase elements, at lower frequencies.

Continuing these studies with a series of Span surfactants, we observed more complicated impedance spectra than with the OLOA 11000[®] surfactant in our prior work [17]. A second semicircle appeared in the Nyquist plot at low frequencies. Here, we focus on this feature as the main topic. We model this more complicated spectrum by including charge adsorption and desorption at otherwise blocking electrodes. The modeling yielded the desired concentration of carriers (and hence the Debye length) despite the complications introduced by the adsorption. Using a Langmuir model for the kinetics of reversible adsorption of charge carriers, we also found that the *desorption* rate increased with total surfactant concentration. While one expects the *adsorption* rate to be proportional to the concentration of charge carriers, the desorption rate was not expected to increase with the bulk concentration. This finding suggests that neutral surfactant molecules or micelles were involved in the desorption of charge.

3.2 Theory

Three models of the impedance of surfactant solutions with charge adsorption at the electrode surface are presented. The first model is based on unsteady diffusion and electromigration of charge carriers with charge adsorption and desorption at either boundary [24]. We refer to this as the “transport model.” The second model is an equivalent circuit with adsorption resistance and capacitance at either electrode [25]. The third model, a variant of the second model, includes constant phase elements. Each of the three models can be applied

to infer charge concentration, the kinetics of adsorption and desorption, and the mobilities of charge bearing species.

3.2.1 Transport Model

Following Barbero [26] we model the unsteady distribution of charge carriers within the fluid cell including adsorption and desorption at the electrodes. Figure 3.1 is a sketch of the domain and coordinate system. When the fluid cell is thin compared to its other two dimensions and the electrodes are good conductors, the unsteady transport is one-dimensional. The positive and negative charge carriers are assumed to have equal diffusion coefficients D and equal but opposite charges $\pm e$, where e is the elementary charge. The reasoning for this assumption is discussed later.

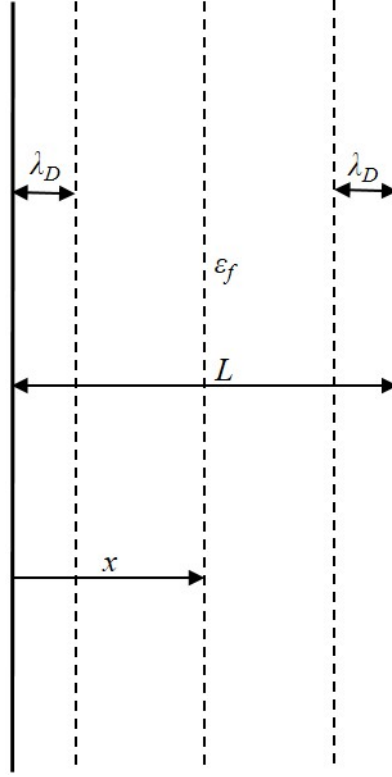


Figure 3.1. A sketch of the domain and coordinate of the thin fluid cell. The cell has a width L that is small compared to the other 2 dimensions of the cell. The fluid permittivity is ϵ_f and λ_D is the Debye length

The Nernst Planck equation expresses the flux of ions due to electromigration and diffusion as

$$N_{\pm} = -D \left(\frac{\partial n_{\pm}}{\partial x} \pm \frac{n_{\pm}}{k_B T} \frac{\partial \phi}{\partial x} \right) \quad (3.1)$$

where k_B is Boltzmann's constant, T is absolute temperature, e is the charge on one proton, $n_{\pm}(x, t)$ are the ion number densities and $\phi(x, t)$ is the electrostatic potential. The + or – subscript denotes either cation or anion, respectively.

Conservation of ions requires

$$\frac{\partial n_{\pm}}{\partial t} + \frac{\partial N_{\pm}}{\partial x} = 0 \quad (3.2)$$

and the electrostatic potential must satisfy Poisson's equation

$$\frac{\partial^2 \phi}{\partial x^2} = -\frac{e}{\varepsilon}(n_+ - n_-) \quad (3.3)$$

where ε is the solution permittivity. The boundary conditions on the potential at the ideally polarizable electrodes take the form of a prescribed voltage which is externally controlled as a function of time. In the absence of any faradaic reactions at the electrodes, any nonzero flux to the electrode must correspond to an accumulation as an associated surface excess for that species, denoted by either Γ_{\pm}^l at the left electrode, or Γ_{\pm}^r at the right electrode:

$$\text{at } x=0: \quad N_{\pm}(0,t) = +\frac{d\Gamma_{\pm}^l}{dt} \quad \text{and} \quad \phi = 0 \quad (3.4)$$

$$\text{at } x=L: \quad N_{\pm}(L,t) = -\frac{d\Gamma_{\pm}^r}{dt} \quad \text{and} \quad \phi = V_{amp}e^{-i\omega t} \quad (3.5)$$

where the kinetics of adsorption require

$$\frac{d\Gamma_{\pm}^l}{dt} = k_a n_{\pm}(0,t) - \frac{1}{\tau_d} \Gamma_{\pm}^l \quad (3.6)$$

and
$$\frac{d\Gamma_{\pm}^r}{dt} = k_a n_{\pm}(L, t) - \frac{1}{\tau_d} \Gamma_{\pm}^r \quad (3.7)$$

where k_a (m/s) is the adsorption rate constant and τ_d (s) is the reciprocal of the desorption rate constant. Cations and anions are assumed to have the same values for k_a and τ_d ; as for the assumption of equal diffusion coefficients, the reasoning underlying this assumption is that modeling efforts made in the Discussion section. In the absence of any applied voltage, the rate of accumulation is zero and the above kinetic equations above can be solved for the equilibrium surface excesses

$$\Gamma_{\pm}^l = k_a \tau_d n_{\pm}(0, t) \quad \text{and} \quad \Gamma_{\pm}^r = k_a \tau_d n_{\pm}(L, t) \quad (3.8)$$

where the product of k_a and τ_d is the adsorption length, L_a . This is Langmuir's adsorption isotherm under conditions of low concentration for which the surface excess Γ is well below the saturation value. This equilibrium adsorption depletes some of the total initial charge concentration, n_{∞} , leaving a residual concentration n^* in the solution. Conservation of either ion requires

$$\Gamma_{\pm}^l + L n^* + \Gamma_{\pm}^r = L n_{\infty}.$$

A uniform concentration of either ion across the fluid at equilibrium means that both local concentrations n_{\pm} equal n^* . Substituting (3.8) for the equilibrium surface excesses into the above equation and solving for n^* yields

$$n^* = \frac{n_\infty}{1 + \frac{2L_a}{L}}$$

and the equilibrium surface excesses of either ion at either electrode are given by

$$\Gamma_\pm^l = \Gamma_\pm^r = L_a n^* \equiv \Gamma^* \quad (3.9)$$

where the adsorption length is defined as L_a . We take this equilibrium state as the initial condition in our transport model:

$$\text{at } t = 0: n_+(x, 0) = n_-(x, 0) = n^*,$$

$$\Gamma_+^l = \Gamma_-^l = \Gamma_+^r = \Gamma_-^r = \Gamma^* \quad \text{and} \quad \varphi(x, 0) = 0 \quad (3.10)$$

The partial differential equations described by equations (3.1) through (3.10) were solved with Matlab (The Math Works, Inc.) to find $n_+(x, t)$, $n_-(x, t)$, $\Gamma_\pm^r(t)$, $\Gamma_\pm^l(t)$ and $\varphi(x, t)$ for various voltage amplitudes, frequencies, and input parameters ε , n^* , D , k_a , and τ_d . The equations were also solved after replacing boundary condition on potential in (3.5) with $\varphi(L, t > 0) = V$ to simulate a potentiostatic experiment.

From Gauss's law the electric field at the right electrode can be written as

$$E(L, t) = -\frac{\Sigma(t) + e\Gamma^r(t)}{\varepsilon} \quad (3.11)$$

where the numerator is the total charge density on the right boundary, which equals the sum of accumulated electronic charges $\Sigma(t)$ and the net ionic charges $e\Gamma^r$, where $\Gamma^r(t) = \Gamma_+^r(t) - \Gamma_-^r(t)$. Electric current $I(t)$ in the external circuit causes accumulation of electronic charges

$$I(t) = A_f \frac{d\Sigma(t)}{dt} \quad (3.12)$$

where A_f is the electrode area wet by the fluid. Eliminating $\Sigma(t)$ between (3.11) and (3.12) gives

$$I(t) = A_f \left[\varepsilon \frac{\partial^2 \varphi(x, t)}{\partial t \partial x} \Big|_{x=d} - e \frac{d\Gamma^r}{dt} \right]. \quad (3.13)$$

Barbero [26] assumed that the applied voltage was a sinusoid of sufficiently small amplitude ($V_{amp} \ll kT/e$) that the current admitted in response was also a sinusoid with the same frequency. In this case it is advantageous to define a complex impedance, $Z(\omega)$, as the quotient of the instantaneous applied potential and current

$$Z(\omega) = \frac{\varphi(L, t)}{I(t)} \quad (3.14)$$

because the time dependence of the quotient vanishes. Barbero [26] gave the solution in terms of a complex admittance, which can be inverted to yield the complex impedance:

$$Z(\omega) = \frac{V_{amp}}{i\omega A_f} \frac{1}{\left\{ -2 \frac{e}{\beta} \left(\cosh\left(\frac{\beta L}{2}\right) + \beta \frac{k_a \tau_d}{1 + i\omega \tau_d} \sinh\left(\frac{\beta L}{2}\right) \right) p_0 + \varepsilon_f c \right\}} \quad (3.15)$$

where
$$\beta = \sqrt{\frac{1}{\lambda_D^2} + \frac{i\omega}{D}} \quad (3.16)$$

and the Debye length λ_D is defined as

$$\lambda_D = \sqrt{\frac{\varepsilon_f k_B T}{2e^2 n^*}}. \quad (3.17)$$

The integration constants p_0 and c are solutions to the following two algebraic equations

$$\begin{aligned} \left\{ 1 + \beta \frac{k_a \tau_d}{1 + i\omega \tau_d} \tanh\left(\frac{\beta L}{2}\right) \right\} p_0 - i \frac{n^* D \beta}{\omega \cosh\left(\frac{\beta L}{2}\right)} \frac{e}{k_b T} c &= 0, \\ -2 \frac{e}{\varepsilon_f \beta^2} \sinh\left(\frac{\beta L}{2}\right) p_0 + \frac{L}{2} c &= \frac{V_{amp}}{2} \end{aligned} \quad (3.18)$$

3.2.2 The Equivalent Circuit Model

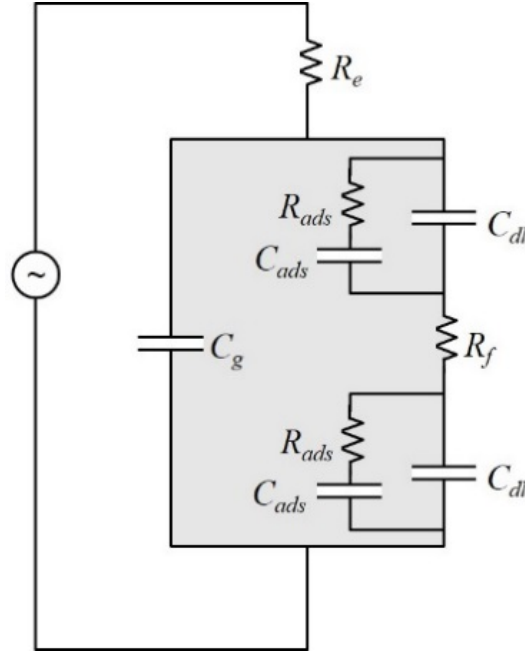


Figure 3.2. Equivalent circuit used to fit impedance data of Span 20[®], Span 80[®], and Span 85[®] in dodecane.

When the current response is linear with the applied voltage, the charge transport and adsorption parameters used in the transport model above can be related to distinct circuit elements of resistors and capacitors. The circuit in Figure 3.2 corresponds to the physical model for charge transport in this case. The circuit consists of the electrode resistance, R_e , due to the conductive ITO, in series with a parallel combination of circuit elements, the first of which is the geometric capacitance, C_g . This capacitance passes current associated with charge separation on the length scale of the cell thickness.

$$C_g = \frac{\epsilon_f A_f + \epsilon_0 A_0}{L}, \quad (3.19)$$

where ε_f is the fluid permittivity, A_f is the fluid area, ε_0 is the permittivity of air, and A_0 is the area of the planar electrodes not wet by the fluid. The geometric capacitance is in parallel with a series combination of fluid resistance

$$R_f = \frac{L}{A_f K} \quad (3.20)$$

where K is the electrical conductivity of the fluid. Any current through the fluid that does not adsorb or desorb at either electrode leads to an accumulation of those charge carriers in a diffuse cloud next to either electrode. In the Gouy-Chapman model,[27] the diffuse cloud has a thickness equal to a few Debye lengths as defined in (3.17) and a voltage difference across it (usually called the zeta potential) that is proportional to the accumulated charge (in the limit of small charges and small voltage drops). Thus each diffuse cloud represents a capacitor having a capacitance of C_{dl} :

$$\frac{C_{dl}}{A_f} = \frac{\varepsilon_f}{\lambda_D}. \quad (3.21)$$

Equation (3.21) expresses (by omission) the assumption that the native zeta potential of the ITO surface is small. We are not aware of any published determinations of the zeta potential of ITO in the presence of the surfactants of this study; hence assigning any particular value is unjustifiable. The Zeta potential of ITO in surfactant doped liquids is discussed more in a later chapter. If the

Zeta potential were to be large compared to the thermal voltage, the Debye lengths reported here would require an increase by the hyperbolic cosine of half the ratio of the zeta potential to the thermal voltage.

Adsorption and desorption of charged species functions as a parallel channel for current in the circuit. If both positive and negative ions can adsorb and desorb from the electrode surface, these processes can be modeled by an additional capacitance and resistance in parallel with the double layer capacitance at each electrode. If the two electrodes are identical, two kinetic parameters appear in the model. The adsorption “resistance” is inversely proportional to the adsorption rate constant [26],*

$$R_{ads} = \frac{\lambda_D^2}{A_f \varepsilon_f k_a}. \quad (3.22)$$

and the adsorption capacitance is proportional to the adsorption length $L_a = k_a \tau_d$:

*Expressions (3.22) and (3.23) were deduced from the low-frequency, thin-Debye-length asymptote of the real and imaginary parts of the impedance given by equation 21 of Barbero [26].

$$\frac{C_{ads}}{A_f} = \frac{L_a \varepsilon}{\lambda_D^2}. \quad (3.23)$$

Each circuit element has its own impedance: the impedance of a resistor $Z_R = R$ and the impedance of a capacitor is $Z_C = i/\omega C$. The total circuit impedance can be calculated as a function of frequency by algebraic combination of these circuit elements. In the limit that the Debye length is thin compared to both the cell thickness and the adsorption length, the result is an algebraic model yielding impedance spectra equivalent to (3.15) through (3.18) of Barbero[26].

3.2.3 Constant Phase Elements

Neither the transport model nor the circuit model described above fully captures the EIS spectra. It is common to replace a capacitor by a constant phase element (CPE) having an impedance is given by $Z_{CPE} = Q^{-1}(i/\omega)^\alpha$ with $0 < \alpha < 1$. [28, 29] For example, we used a CPE to represent C_{dl} in fitting our earlier EIS spectra measured with nonpolar fluids [17]. When Z_{CPE} is expressed in polar form $re^{i\theta}$, the phase angle θ equals $\pi\alpha/2$, which is independent of ω ; this is why this form is called a “constant-phase element.” A physical circumstance that would exhibit CPE behavior is discussed in the Appendix.

Once the values of Q_{dl} and α for the CPE are determined by fitting the spectra to the equivalent circuit, the corresponding double-layer capacitance can be calculated from [30]

$$C_{dl} = 2 \left(Q_{dl} R_f^{1-\alpha} \right)^{1/\alpha} \quad (3.24)$$

where the factor of 2 arises because the model includes one CPE to model two capacitors in series, one for each electrode. The two parameters Q_{dl} and α provide two degrees of freedom which together control the mean and standard deviation of the time-constant distribution. Recall that the mean fluid resistance R_f is determined as a separate circuit element. The mean double-layer capacitance C_{dl} given by (3.24), when multiplied by the mean resistance R_f , gives the mean value of the distributed time constants.

We also use a CPE for the adsorption capacitance to improve the fit with experimental spectra. The two parameters for the adsorption CPE are designated by Q_{ads} and β with

$$C_{ads} = 2 \left(Q_{ads} R_{ads}^{1-\beta} \right)^{1/\beta}. \quad (3.25)$$

A likely source of distributed time constants associated with adsorption is non-uniform chemistry on the electrode surface, which would manifest itself in a distribution of the desorption times τ_d . The adsorption rate constant k_a is an unlikely source of CPE behavior because it vanishes from the product $R_{ads}C_{ads}$.

3.3 Materials and Methods

The nonionic surfactants studied in this work were Span 20[®] (sorbitan monolaurate), Span 80[®] (sorbitan monooleate), and Span 85[®] (sorbitan trioleate) (Sigma-Aldrich). All three surfactants have a polar sorbitan head group connected to a nonpolar tail. Span 20[®] has one 12 carbon tail and is the smallest of the three surfactants with a molecular weight of 346.46 g/mol. Span 80[®] has one 16 carbon tail and a molecular weight of 428.62 g/mol. Span 85[®] has three 16 carbon tails and a molecular weight of 957.52 g/mol. The nonpolar solvent was dodecane (anhydrous 99+%, Sigma-Aldrich). Each surfactant was dissolved in dodecane at dopant concentrations between 0.1 and 10% by weight. All chemicals were used as received without further purification. The solutions were not dried and the humidity was not controlled in situ, but each solution was stored in a desiccator when not in use.

The thin fluid cell used for impedance spectroscopy appears in Figure 3.3. The two electrodes were glass microscope slides coated with a 100 nm thick layer of indium tin oxide (ITO) (Sigma-Aldrich). The cell assembly procedure for each experiment was the same as reported previously [17]. Silica spacer particles (8 μm) (Cospheric, Santa Barbara), added to the surfactant solution at a particle concentration of 1 mg/mL, established the cell gap. 15 μL of the surfactant solution with spacer particles formed a liquid film contained by the electrodes and capillary forces. The average gap between the plates was calculated for each cell

by dividing the imaged area of the liquid film into the known added volume. Electrical connection was achieved through leads epoxied to the ITO and the cell was placed in a Faraday cage. A VersaSTAT 3 potentiostat (Princeton Applied Research), equipped with a Low Current Interface (LCI), powered the cell that was configured as a two electrode circuit by short-circuiting the reference electrode terminal of the potentiostat to the terminal of the counter electrode. The procedure for acquiring the impedance data was the same as in our previous study. [17]

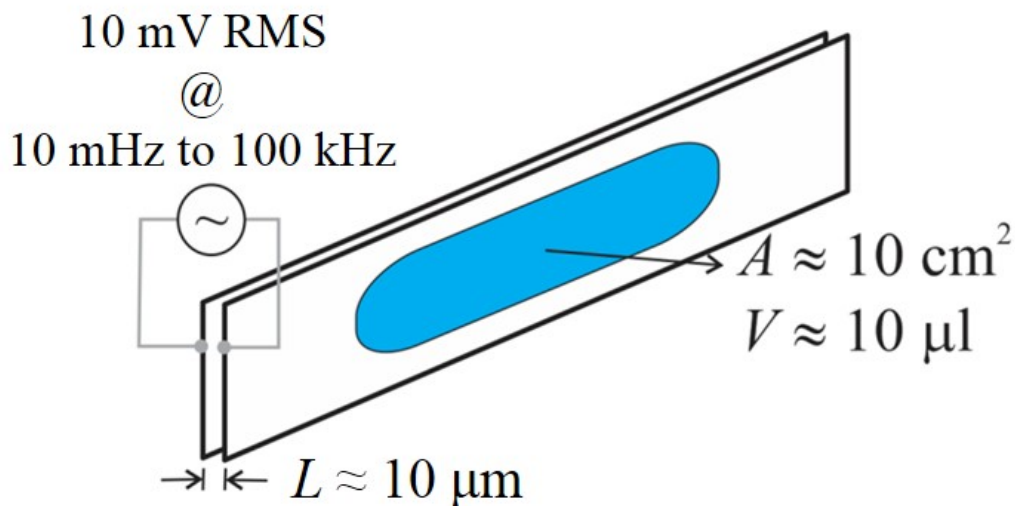


Figure 3.3. Schematic of the thin fluid cell for impedance spectroscopy measurements.

3.4 Results and Discussion

3.4.1 Contrasting spectra of OLOA 11000[®] and Span 80[®] in Dodecane

The impedance spectra of 1.1% wt. (19.5 mM) Span 80[®] in dodecane and 1.0% wt. OLOA 11000[®] in dodecane are compared in a Nyquist plot in Figure

3.4. The two spectra were quite different although acquired with essentially the same surfactant concentration and the same electrodes. The Nyquist plot of OLOA 11000[®] consists of one semicircle at higher frequencies, associated with R_f and C_g acting in parallel

(see Figure 3.2), and a nearly vertical “tail” at lower frequency arising from the double-layer capacitance C_{dl} . This shape corresponds in general to the circuit of Figure 3.2 omitting C_{ads} and R_{ads} . The deviation of the Nyquist plot from a vertical line at the lowest frequencies might arise from non-uniform electrode spacing, and can be modeled by replacing C_{dl} by a CPE, as described in the Theory section. By contrast, the Nyquist plot of the Span 80[®] solution in Figure 3.4 had two connected arcs with two local minima in the imaginary impedance. The qualitative difference between the two impedance spectra reflects the occurrence of some extra phenomenon in the Span 80[®] case. Two arcs were also observed in the spectra of Span 85[®] and Span 20[®] solutions as well. These additional features in the spectra cannot be expressed with the circuit model used in our previous work [17]. We attribute this second arc to adsorption and desorption of charge, as described in the next section.

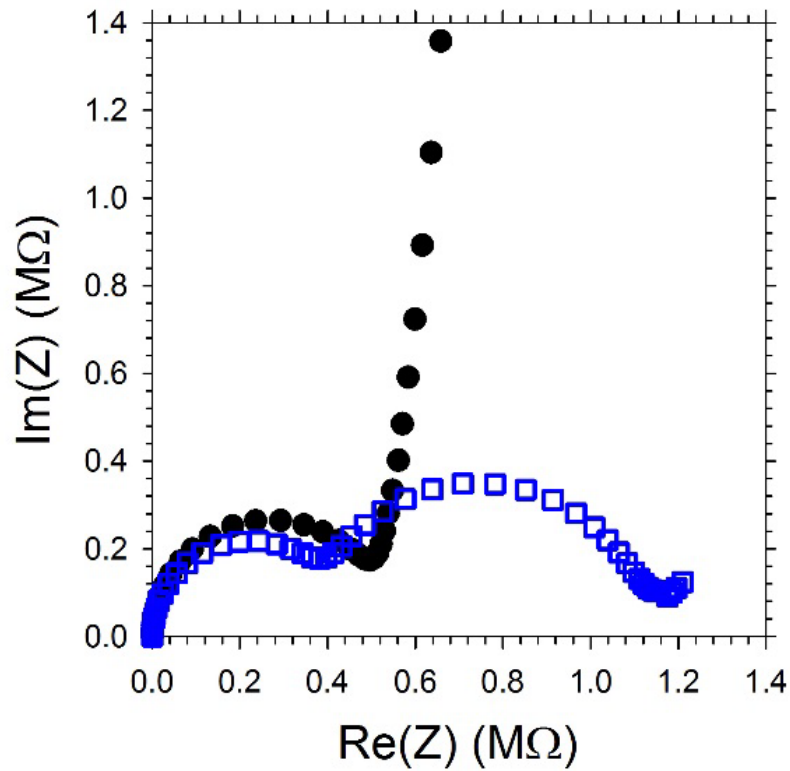


Figure 3.4. Nyquist plot comparing the impedance spectra of 1.0% wt. OLOA 11000[®] in dodecane (filled black circles)[17] and 1.1% wt. (19.5 mM) Span 80[®] in dodecane (open blue squares). The second semi-circle in the Span 80[®] impedance arises from reversible charge adsorption at low frequencies.

3.4.2 EIS spectra and adsorption

The low frequency “second” semicircle of Figure 3.4 appears if another channel for current is available. This second semicircle could also not be described by the different anionic and cationic mobilities according to an analytical model by Lelidis and Barbero.[31] Since faradaic current was unlikely in the nonpolar liquid, we hypothesized that adsorption and desorption of charge might account for the observed behavior. In other words, as charge carriers in the fluid arrive at either electrode, they can either 1) accumulate in the diffuse cloud [corresponding to the double-layer capacitance C_{dl} in Figure 3.2], or 2) adsorb

onto (desorb from) the electrode [corresponding to the adsorption capacitance C_{ads} in Figure 3.2]. The procedure for testing the hypothesis and its internal consistency had three steps:

1. The experimental data were fit to the adsorption circuit of Figure 3.2 using EIS Spectrum Analyzer software implementing the “Powell” algorithm [32]. The circuit was modified slightly by substituting CPEs for each of the two “electrode capacitances” C_{dl} and C_{ads} to obtain the best possible agreement. This process yielded best values for the CPEs (Q_{dl} , α , Q_{ads} , β) as well as R_e , R_f , R_{ads} . The results of this process is designated as the “CPE Model.”
2. Equations (3.24) and (3.25) from the Theory section were used to convert Q_{dl} and Q_{ads} to their corresponding average C_{dl} and C_{ads} . The predictions of the circuit model based on capacitors (instead of CPE’s) are designated as the “Capacitor Model.”
3. Using (3.19) - (3.23) allows one to infer the dielectric constant ϵ , conductivity K , Debye length λ_D , adsorption rate constant k_a , and desorption time constant τ_d from the geometric capacitance, C_g , the fluid resistance, R_f , the double layer capacitance, C_{dl} , the adsorption resistance, R_{ads} , and the adsorption capacitance, C_{ads} . Predictions of equations (3.1) through (3.18) based on these values of the transport parameters are designated as the “Transport Model.”

Figure 3.5 compares each of the three models to the experimental EIS spectrum of an 8.84 mM solution of Span 80[®] in dodecane expressed in both a Nyquist plot and a Bode plot. The CPE Model expresses the impedance of the cell extremely well at all frequencies. The three models coincide at high frequencies (left side of Figure 3.5A and above 20 Hz in Figure 3.5B). The Capacitor Model is indistinguishable from the transport model over the entire spectrum, but they both deviate from the experiments at low frequencies (right side of Figure 3.5A). The agreement between the Capacitor Model and the Transport Model confirms that adsorption and desorption of charge carriers on the electrode can be modeled as a resistor R_{ads} and capacitor C_{ads} in parallel with C_{dl} (as shown in Figure 3.2); and it further confirms (3.22) and (3.23) for their relationship to transport properties.

The overall agreement among the models and data is good evidence that the lumped parameters chosen to define each circuit element in the previous section are accurate. The Transport and Capacitor Models overestimate the imaginary part of the impedance between 1.5 and 5 Hz corresponding to the top of the second arc (see Figure 3.5A). Similarly, the real part of the impedance at frequencies below 0.1 Hz, *i.e.* farthest from the origin of Figure 3.5A, increases slightly as frequency decreases. The CPE used in place of a simple adsorption capacitance allows fitting of this feature while the transport model and capacitor model do not. Since both the double layer capacitance and the adsorption

capacitance would be affected by small heterogeneities in the electrode surface (commonly associated with CPE behavior), it is reasonable to model both elements with CPEs and calculate the effective pure capacitance of each element using (3.24) and (3.25)

In addition to fitting the CPE circuit model to the measured impedance spectra, both the Capacitor Model and the Transport Model were fit directly to the impedance data, bypassing the CPE formulation. Table 3.1 shows the best-fit parameters in each the three models for the spectrum of 8.84 mM Span 80[®] in dodecane shown in Figure 3.5. The values of parameters obtained do not depend strongly on the model. However the uncertainty in the value of C_{dl} deduced from the CPE Model is significantly smaller than that the uncertainty in the value of C_{dl} deduced more directly from the Capacitor Model. This smaller uncertainty is likely the result of better fitting by the CPE model at 0.1 – 20 Hz for which the double-layer capacitance matters most, whereas the capacitor model fits poorly. For this reason, we use values of C_{dl} and C_{ads} inferred from the CPE Model in later comparisons.

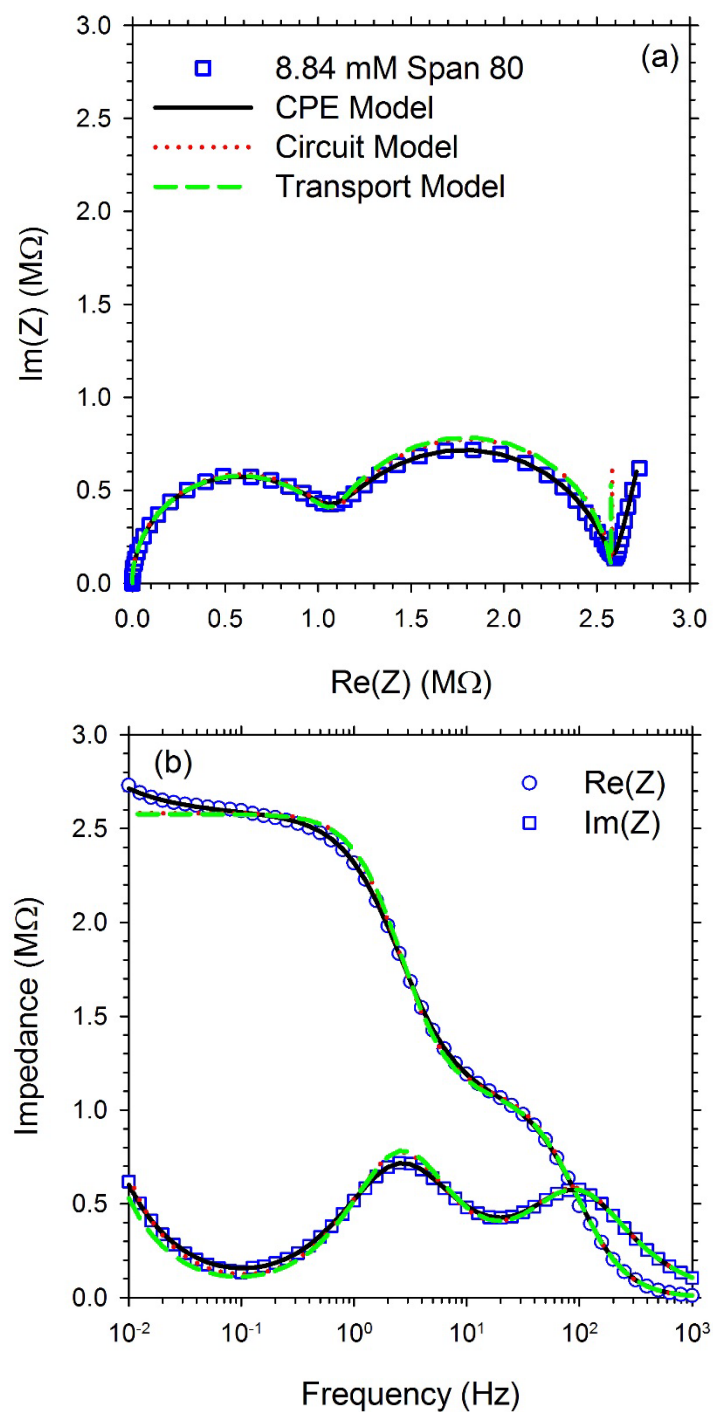


Figure 3.5. Comparison of various models (curves) with experimental data (symbols) obtained with 8.84 mM Span 80® in dodecane. The predictions of the capacitor model (dotted red curve) and the transport model (dashed green curve) are virtually identical under these conditions.

In summary of this subsection, Figure 3.5 demonstrates that introducing first-order adsorption and desorption kinetics captures the major features of impedance spectra observed when Span 80[®] is added to dodecane. Similar agreement was obtained for Span 20[®] as shown in Figure 3.6. The impedance spectra of Span 85[®], however, were problematic and required special attention.

Table 3.1. Comparison of best fit parameters from three different models.

8.84 mM Span 80 [®] in dodecane	CPE Model	Capacitor Model	Transport Model
Conductivity (nS/m)	15.2 ± 0.1	14.8 ± 0.2	15.2
Dielectric constant	2.21 ± 0.01	2.21 ± 0.03	2.18
Debye length (nm)	221 ± 9	213 ± 13	215
Charge concentration ($1/\mu\text{m}^3$)	32 ± 3	35 ± 5	33
D ($\mu\text{m}^2/\text{s}$)	38 ± 4	34 ± 5	37
k ($\mu\text{m}/\text{s}$)	3.7 ± 4	3.5 ± 5	3.8
Tau (s)	40 ± 10	40 ± 20	30

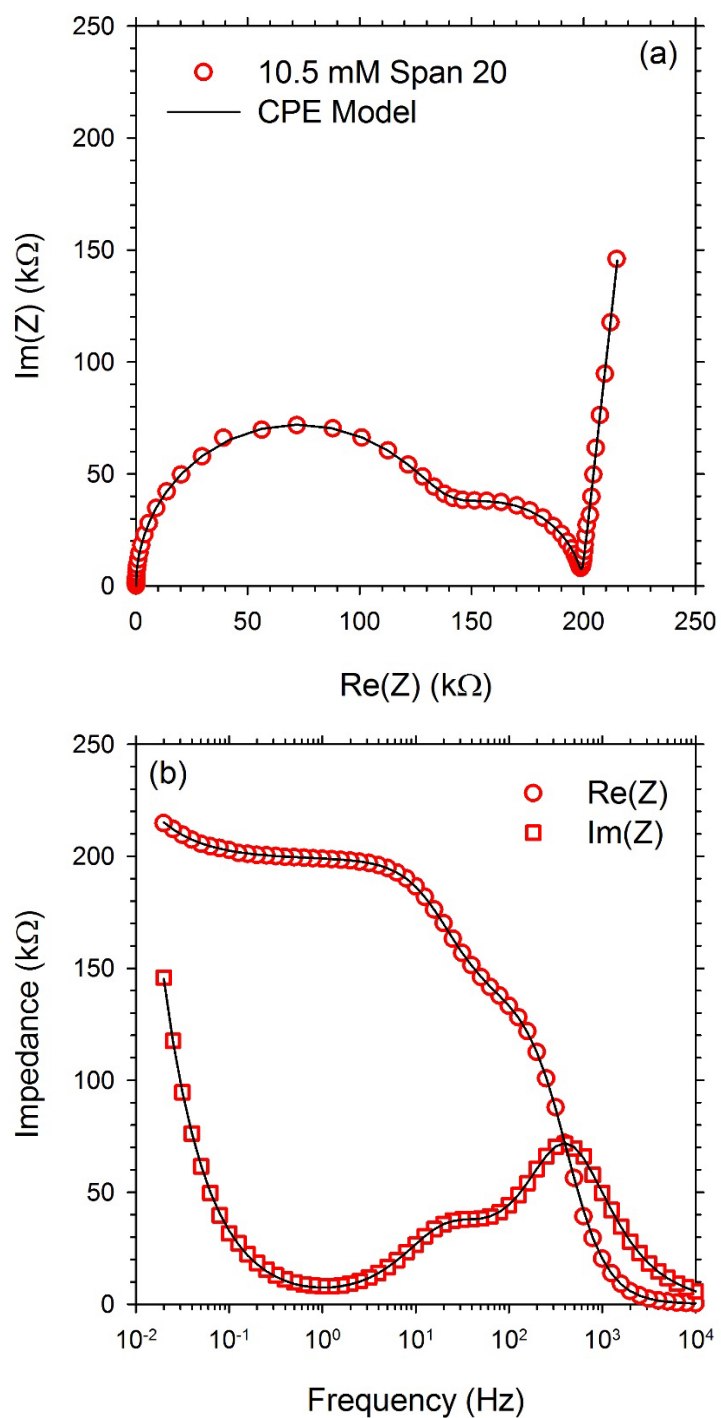


Figure 3. 6. Nyquist plot (a) and Bode plot (b) of the impedance and the best fit CPE model for 10.5 mM Span 20.

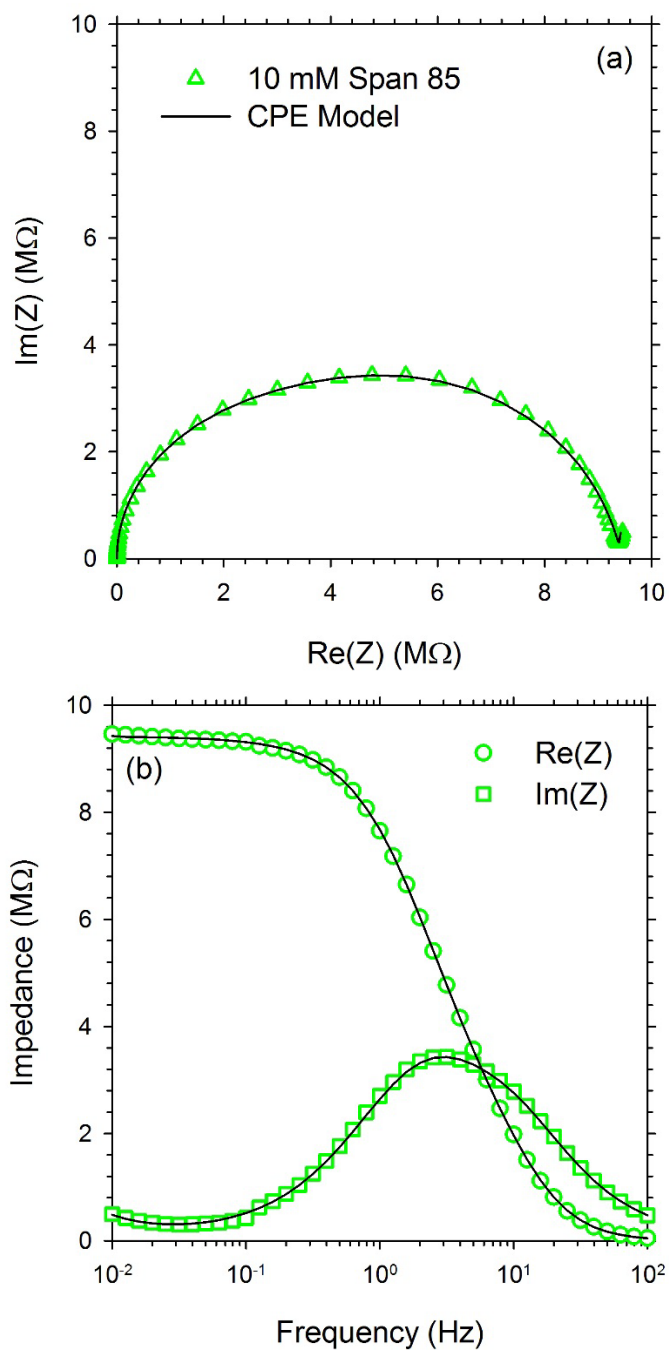


Figure 3.7. Nyquist plot (a) and Bode plot (b) of the impedance and the best fit CPE model for 10.0 mM Span 85. Rather than two distinct semicircles, one distorted semicircle is observed because of the thick Debye length of the solution compared to the gap distance of about 10 μm .

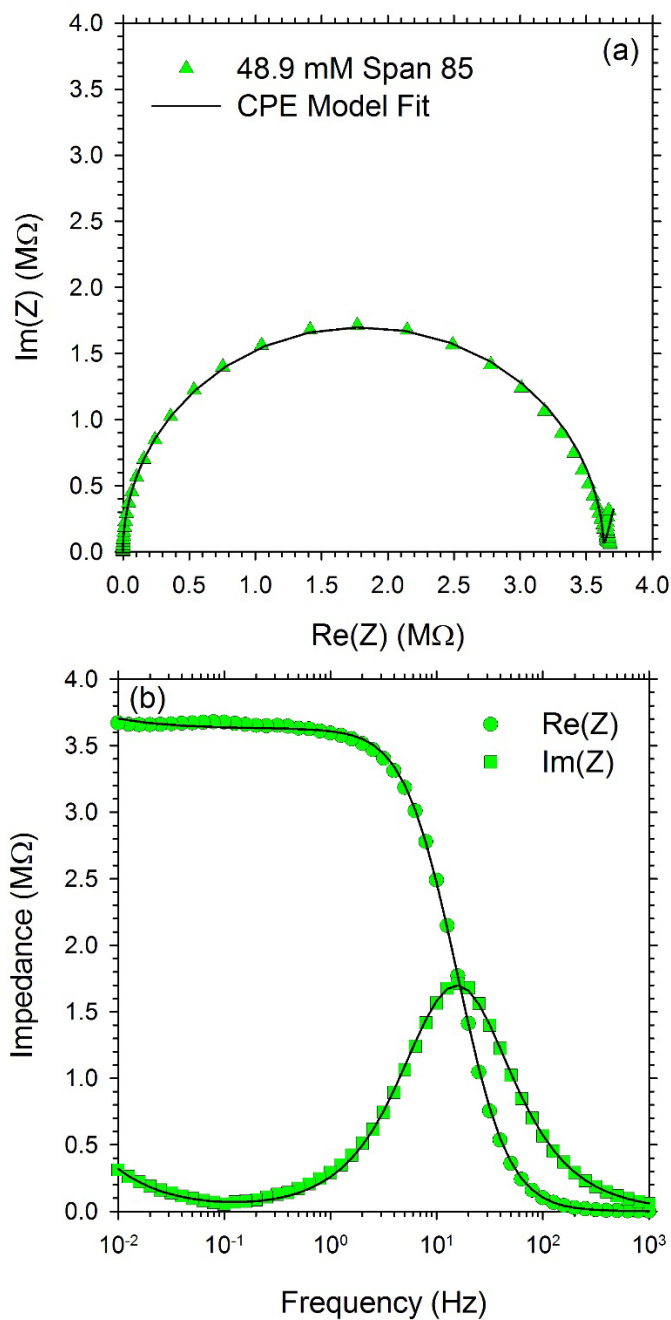


Figure 3.8. Nyquist plot (a) and Bode plot (b) of the impedance and the best fit CPE model for 48.9 mM Span 85. At this concentration of Span85 only one semicircle is observed because the adsorption resistance is small compared to the fluid resistance and cannot be accurately resolved. In this case an accurate measurement of the double layer capacitance is not possible.

3.4.3 Impedance spectra of Span 85

The Nyquist plots of Span 85[®] in dodecane in Figure 3.7a and Figure 3.8a showed a single arc rather than two distinguishable semicircles. Close inspection of Figure 3.7a reveals that the arc is not a semicircle: the height of the arc (3.4 M Ω) is slightly less than half of the width along the horizontal axis (4.7 M Ω). This is more obvious in the Bode plot of Figure 3.7b; if the Nyquist plot is a semicircle then the real and imaginary parts should be equal at the frequency (about 3 Hz) corresponding to the maximum in the imaginary part. But Figure 3.7b shows that the real and imaginary parts cross instead at a frequency higher than the frequency of the maximum in the imaginary part. By contrast, note that the real and imaginary parts of Figure 3.5b and Figure 3.6b cross at the local maximum in the imaginary parts, indicating that the high-frequency (left) arcs in the corresponding Nyquist plots are semicircles. This departure from a semicircular shape of the arc in Figure 3.7a is a feature that can be fit using a CPE for the double-layer capacitance. The slightly negative slope in the imaginary part at the lowest frequencies of Figure 3.7b provides some information about the adsorption capacitance, although more data at lower frequencies would be needed to accurately determine the CPE parameters for adsorption. Nevertheless, we can extract most of the properties for Span 85[®] at 10 mM.

At higher concentrations of Span 85[®], however, the Nyquist plot (Figure 3.8a) more closely resembles a single semicircle and the intersection of the real and imaginary parts on the Bode plot appear normal. As with lower

concentrations of this same surfactant, adsorption is occurring and the arc shown in Figure 3.8a is slightly distorted from a semicircle. The diameter of this semicircle represents the fluid resistance R_f which still yields the fluid conductivity K from (3.20); the decay of the imaginary part at very high frequency also yields the geometric capacitance C_g and the corresponding fluid permittivity ϵ . Values of the remaining parameters, however, had significant uncertainty. The adsorption resistance R_{ads} was only about 10% of the fluid resistance R_f . This small fraction explains why a second arc is not seen: the radius of the two semicircles in Figure 3.5A are $R_f/2$ and R_{ads} ; when R_{ads} becomes negligible compared to R_f , the second semicircle is not apparent. Moreover, in the limit in which R_{ads} is zero, the two capacitors C_{ads} and C_{dl} in Figure 3.2 act in parallel as one larger capacitor and only their sum $C_{ads} + C_{dl}$ could be inferred from fitting of EIS data. This explains the high uncertainty in C_{ads} and C_{dl} when R_{ads} is small compared to R_f .

3.4.4 Complications in thin cell EIS with adsorption

The foregoing discussion regarding Span 85[®] has general implications for using EIS to obtain charge carrier concentrations in nonpolar liquids. Neglecting adsorption, we would obtain reasonable values for R_f and C_g for Span 85[®] (inferred from the frequency and height of the maximum in the imaginary part in the Bode plot), but the double-layer capacitance C_{dl} (inferred from the upturn in the imaginary part at the lowest frequencies) would be absurdly large (about 3

$\mu\text{F}/\text{cm}^2$); the corresponding value of the Debye length calculated from (3.21) would be about 0.5 nm, smaller than the smallest value expected in water. The difficulty arose because $R_{ads} \ll R_f$ at higher concentrations. Substituting (3.20) and (3.22), the ratio R_{ads}/R_f equals $D/k_a L$, which is the reciprocal of the Damkohler (Da) number for adsorption. If we think of adsorption of surfactant as a two-step process in which the steps occurs in series (e.g. R_f and R_{ads} act in series in Figure 3.2); surfactant diffuses from the bulk to the surface and then adsorbs onto the surface. R_{ads}/R_f represents the ratio of the diffusion speed D/L to the adsorption speed k_a . The rate of the overall process is limited by the slower step. When Da is small and $R_{ads} \ll R_f$, the kinetics of adsorption are fast and the rate of adsorption of the surfactant is “diffusion limited”; under these circumstances, the kinetics of the adsorption “reaction” (i.e. R_{ads}^{-1}) cannot be determined accurately.

The Damkohler number points to a tactic that one might consider in order to exaggerate R_{ads} ; decreasing the cell gap L would bias the ratio R_{ads}/R_f favorably. Other physics, however, can limit the effectiveness of this approach. The Capacitor and CPE Models treat the vast majority of the fluid as electrically neutral and homogeneous. Accumulation of non-adsorbing, nonreactive carriers is assumed to occur in a thin but diffuse region proximal to both electrodes and having a capacitance given by (3.21). Both of these assumptions require the Debye length λ_D to be a negligible fraction of the electrode spacing L . This is equivalent to assuming $C_{dl}/C_g \gg 1$. This assumption is not made in the transport

model which should still apply even when the Debye length is not small compared to the electrode spacing, which allows a brief exploration of the impact of L/λ_D .

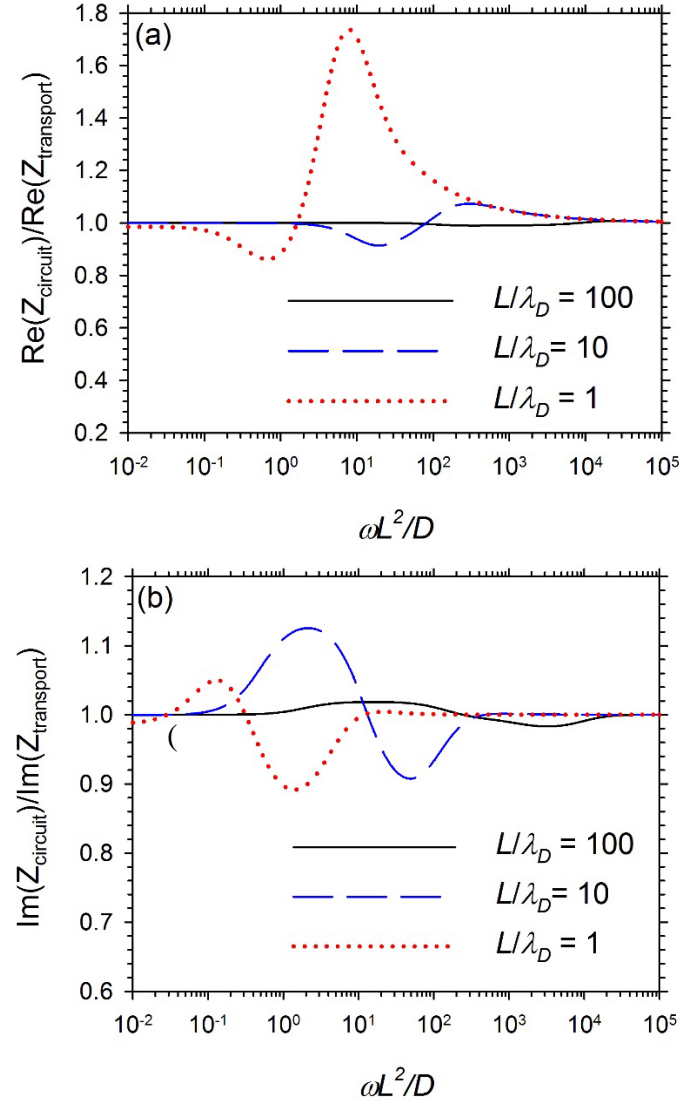


Figure 3.9. Ratio of the real part (a) and imaginary part (b) of the impedance calculated from the circuit model to the transport model versus frequency for various ratios of the gap distance, L , to the Debye length λ_D . As the Debye length approaches the length of the gap distance the circuit model cannot accurately predict the impedance as shown by the transport model solution.

Figure 3.9 a and b show how the real and imaginary impedance calculated by the circuit model and the transport model differ when the Debye length approaches the gap distance, L . In these calculations, the electrode spacing L and all other transport and electrode properties are fixed while the concentration of carriers is decreased, thereby increasing the Debye length while decreasing the conductivity. The electrical parameters used in the circuit model are calculated from (3.19) through (3.23). At a ratio of L/λ_D equal to 10 the error between the two models approaches 10% in both the real and imaginary impedance. Therefore the Debye length should be no more than 10% of the electrode spacing.

The twin constraints that both R_{ads}/R_f and L/λ_D should exceed certain values can be rendered in a single graph. Figure 3.10 summarizes the values of the two ratios C_{dl}/C_g (or L/λ_D) and R_{ads}/R_f (or D/k_aL) for experiments performed in this work. The data points mapped on the figure were all taken from measurements in a cell with a gap around 10 μm . The data taken below the CMCs (filled points) gave Debye lengths that were too large to be fit accurately with the circuit model. While a simple solution would be to use a larger cell gap to raise the ratio of L/λ_D , this would simultaneously lower the ratio of D/k_aL and might violate the other constraint. For the systems studied in this work, the only approach to accurately measure Debye lengths with EIS would be to use a thick cell (100 μm – 1mm) with an electrode having a lower rate of charge adsorption than ITO coated glass, thus lowering the value of k_a and raising D/k_aL . Figure 3.10, unfortunately, is not

predictive; one does not know *a priori* the diffusion coefficient, Debye length, and adsorption rate constants. Figure 3.10 does show that varying the concentration and cell gap in multiple experiments might be necessary to obtain a full picture of the phenomena present.

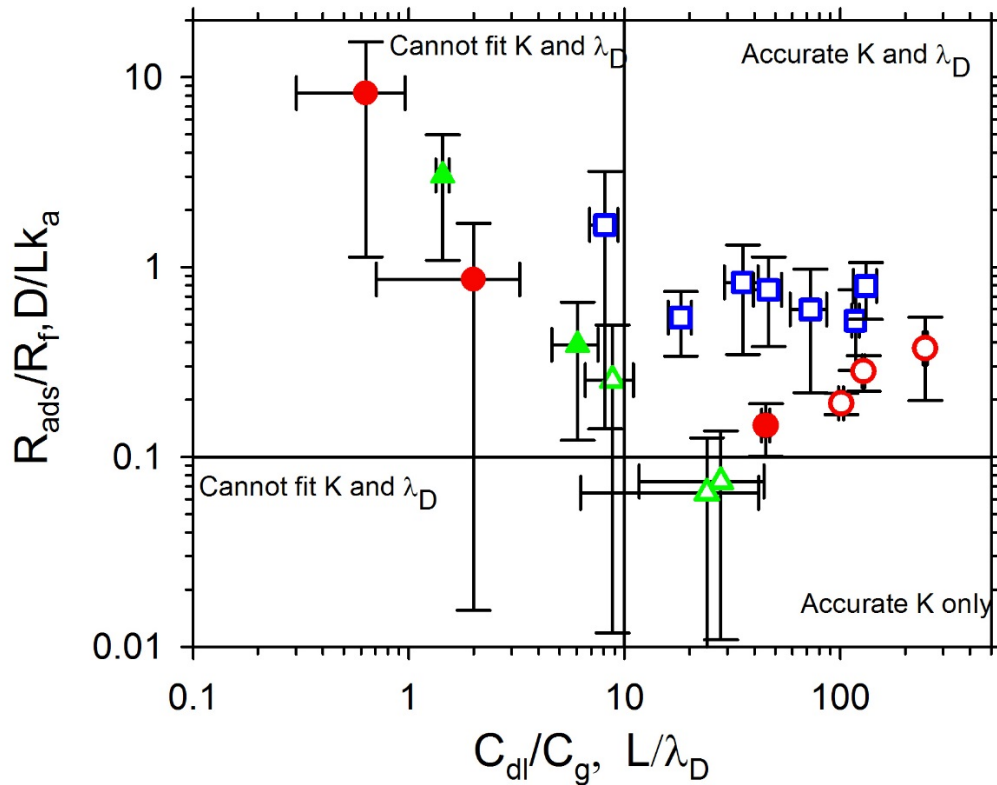


Figure 3.10. Operational diagram for thin cell impedance spectroscopy with charge adsorption. The ratio of the adsorption resistance to the fluid resistance is plotted versus the ratio of the double layer capacitance to the geometric capacitance for Span 20[®] (red circles), Span 80[®] (blue squares), and Span 85[®] (green triangles) in dodecane. When the ratio of the capacitances is less than 10 than the circuit model fails to accurately measure the fluid properties resulting in a high standard deviation in the measured parameters than at higher ratios. If the ratio of the adsorption resistance to the fluid resistance becomes less than 0.1 than the charge adsorption is diffusion limited and the double layer capacitance cannot be resolved resulting in large standard deviation in the parameters. The open data points above the CMC of each surfactant generally follow both constraints except for low concentrations of Span 80[®] and Span 85[®] where the Debye lengths are still long compared to the gap distance, and at high concentrations of Span 85[®] where the adsorption resistance is very low. Below the CMC (filled points), the charge concentration is very low leading to large Debye lengths that cannot be fit with equivalent circuits.

3.4.5 Conductivities

Figure 3.11 summarizes the conductivity calculated from the solution resistance, R_f , according to (3.20). The data points represent the average value for at least 3 different measurements. The error bars represent the standard deviation between the different measurements. A “measurement” is defined as an experiment in which the fluid cell was re-assembled with cleaned electrodes and fresh solution. Previous studies[12] of Span 85[®] in hexane have shown the conductivity to be proportional to concentration at concentrations above the critical micelle concentration (CMC) (open triangles), which is about 10mM, and also proportional to concentration below the CMC (filled triangles); the ratio of the two slopes (below the CMC to above the CMC) is 1.66. In the log-log plot of Figure 3.11, this change in the proportionality constant at the CMC means that the conductivity of Span 85[®] should be rendered as two parallel lines having a slope of unity and intercepts separated by $\log 1.66 = 0.2$. While the proportionality with concentration is confirmed by the slope of unity in Figure 3.13, the change in intercept of 0.2 units of a decade is comparable to the size of the error bars and therefore is not apparent in Figure 3.11.

Similarly, the conductivity of Span 20[®] in kerosene has also been shown to be proportional to surfactant concentration at concentrations above 0.1% by weight and larger than the conductivities of both Span 80[®] and Span 85.[13] The results from this study also show the higher conductivity of Span 20[®] in Figure 3.11 and the conductivity appears to be linear at concentrations above 5 mM

(open circles). The large difference between the conductivity of Span 20[®] below 5 mM (filled circles) and above (open circles), is most likely due to 5 mM being near the CMC for Span 20[®] in dodecane. Above the CMC, Span 20[®] forms micelles large enough that a significant portion of micelles can carry charges that are not formed below the CMC.

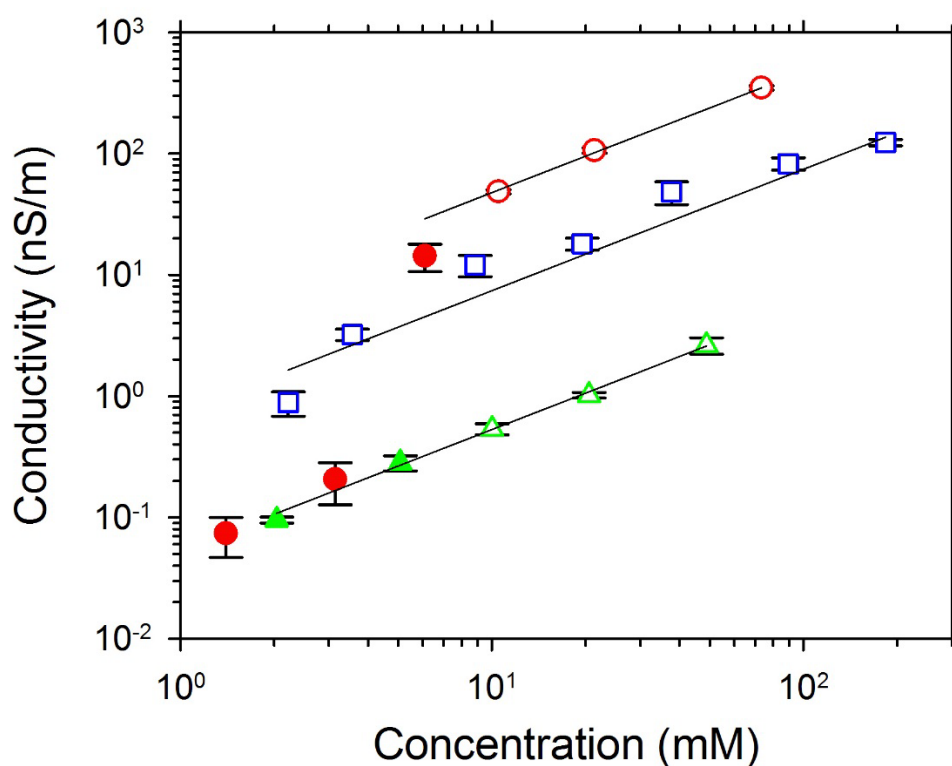


Figure 3.11. The most conductive surfactant is Span 20[®] (red circles), followed by Span 80[®] (blue squares) and Span 85[®] as the least conductive (green triangles). The data points at concentrations above the CMC (open) follow trend lines with a slope of 1 while the data below the CMC (filled) do not.

Previous conductivity measurements of Span 80[®] in hexane are proportional to concentration at high surfactant concentrations, but not throughout the entire micellar region because the Span 80[®] micelle size and shape is concentration dependent.[11] While all the measurements taken for Span 80[®] in this work were

at concentrations higher than the reported CMC of 0.058 mM[33], the conductivity of Span 80[®] in dodecane displayed in Figure 3.11 is not linear with concentration throughout the entire regime, which suggests that the size and shape of the micelle might not be constant with concentration in dodecane as well.

3.4.6 Debye lengths, charge concentrations, diffusion coefficients

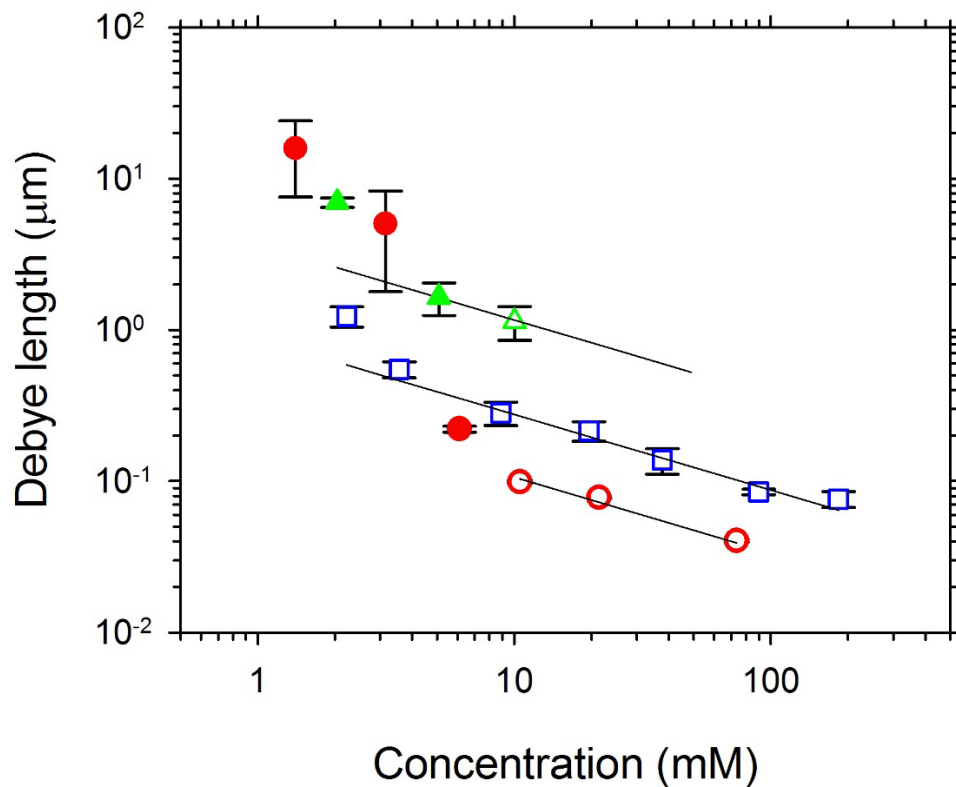


Figure 3.12. Debye lengths of Span 20[®] (red circles), Span 80[®] (blue squares), and Span 85[®] (green triangles) are plotted versus surfactant concentration calculated from the inferred double layer capacitance. As more surfactant is added the Debye lengths at either electrode get smaller. The data points at concentrations above the CMC (open) follow trend lines with a slope of -0.5 while the data below the CMC (filled) do not.

The inclusion of adsorption and desorption model in the model allowed fitting of the impedance spectra as demonstrated in Figure 3.5 – Figure 3.7. Thus we could extract the double layer capacitance despite the presence of adsorption

and desorption with the appropriate limitations mentioned previously. We calculated the fluid permittivity and Debye lengths from relations between the findings of values for the circuit elements of Figure 3.2 and equations presented in the Theory section. The Debye lengths, λ_D , so calculated appear for each surfactant in Figure 3.12. At high concentration the Debye lengths decreased with the characteristic square root of the surfactant concentration, while they decreased more strongly at lower concentrations.

The Debye lengths at each concentration were then used to calculate the charge concentration in the bulk liquid, n^* , using (3.17). The charge concentration is displayed in Figure 3.13 as a function of surfactant concentration. At low concentrations the charge concentration of each surfactant increased with surfactant concentration with a power greater than 1. At high concentrations the charge concentration was proportional to the surfactant concentration. In the high concentration region Span 20[®] maintained a ratio of charge carriers per surfactant molecule of 22 ppm while Span 80[®] had a 3 ppm ratio and Span 85[®] had a ratio of about 0.2 ppm.

The diffusion coefficient for the charge carriers, D , is

$$D = \frac{k_B T K}{2n^* e^2} \quad (3.26)$$

when one assumes the charges are 1-1 with equal mobilities. The diffusion coefficients for charge carriers were calculated at each concentration from the measured conductivity and charge concentration. The diffusion coefficients are shown in Figure 3.14. At low concentrations below the CMC for Span 85[®] the diffusion coefficients are high indicating that the charge carriers are smaller than reverse micelles. At high concentrations the diffusion coefficients are essentially independent of concentration. Although the uncertainty in some of the values in Figure 3.14 is large, Span 20[®] consistently has the smallest mean diffusion coefficient which means that the micelles formed by Span 20[®] probably are larger than the micelles of the other surfactants in dodecane. The larger micelles of Span 20[®] would stabilize charge more effectively, which might explain why Span 20[®] has the highest ratio of charge carriers per molecule.

The assumption of equal diffusion coefficients for cations and anions is consistent with the disproportionation model in which the collision of two neutral micelles results in the exchange of a proton or other ion, thus forming an ion pair which might dissociate by thermal energy to form separate but equal-sized and oppositely-charged ions.[2] Other mechanisms have also been proposed which result in unequal sized ions.[16, 34] In theory, the impedance spectra at low frequencies differ for these two cases.[26, 31] If the cations and anions have different diffusion coefficients the real part of the impedance will have two plateaus similar to the observed real impedance in Figure 3.5B, but only one local

maximum arises in the imaginary part of the impedance because the effect does not result in any additional capacitance. While no evidence of different diffusion coefficients is observed, all the experimental spectra reported in this paper exhibit significant CPE behavior at low frequencies, which obscures any difference between equal versus unequal diffusion coefficients. Thus we can make no conclusion regarding the equality or inequality of the diffusion coefficients.

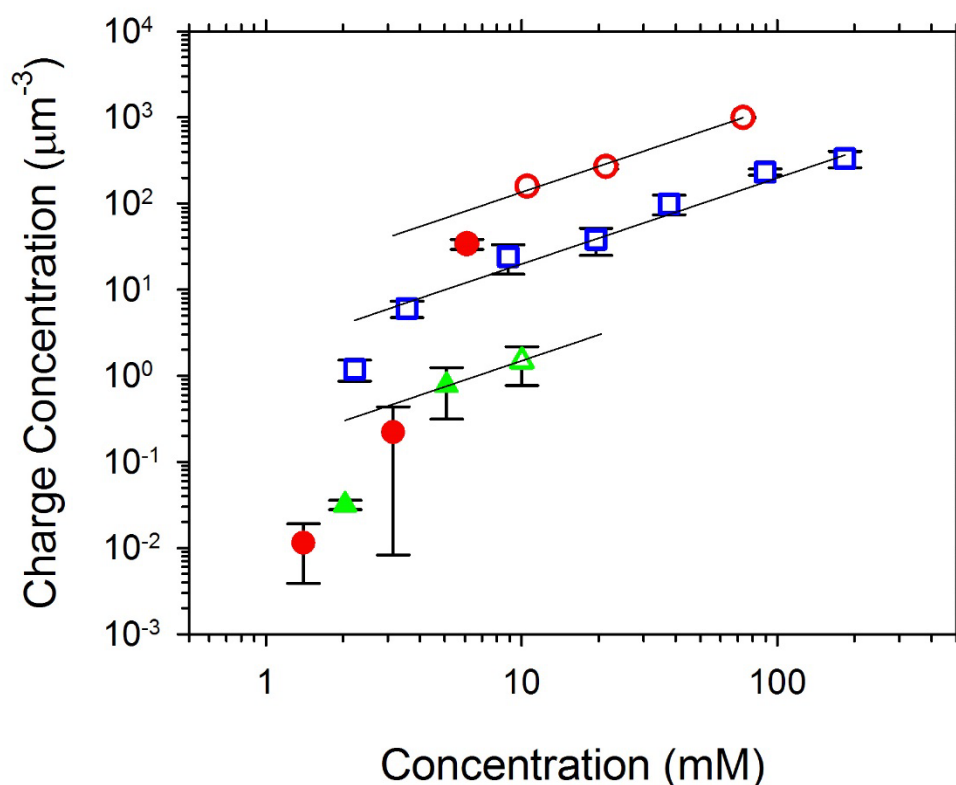


Figure 3.13. Bulk charge concentration of Span 20[®] (circles), Span 80[®] (squares), and Span 85[®] (triangles) is displayed versus surfactant concentration found from the Debye lengths. The data points at concentrations above the CMC (open) follow trend lines with a slope of 1 while the data below the CMC (filled) do not.

As mentioned in a previous subsection, Span 85[®] was problematic for the determination of charge concentration when R_{ads} decreased relative to R_f at higher concentrations. Below the CMC, however, the diffusion coefficient of charge

carriers is significantly higher than above the CMC (see Figure 3.14) which results in a higher value of R_{ads}/R_f (higher Da); thus most of the difficulty fitting R_{ads} occurs above the CMC. Increasing the surfactant concentration above the CMC has no effect on the resolution of the difficulty. As the concentration of surfactant increases, the concentration of charge carriers also increases (see Figure 3.13), which decreases the square of the Debye length and increases the conductivity proportionally (no effect on Da).

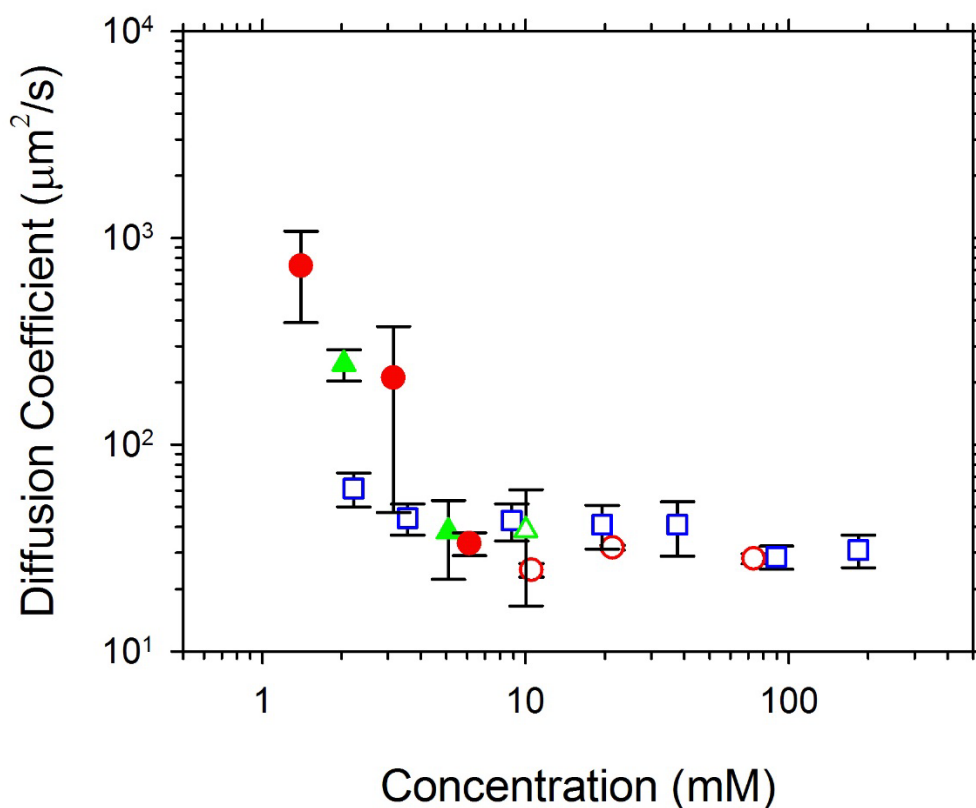


Figure 3.14. Diffusion coefficients of charge carriers of Span 20® (red circles), Span 80® (blue squares), and Span 85® (green triangles) in dodecane plotted on a log-log scale. At below the CMC (filled) concentrations the diffusion coefficients are large signifying small charge carriers. Above the CMC (open) the diffusion coefficient is smaller and near constant.

3.4.7 Adsorption and desorption parameters

The best fit values of the adsorption resistance, R_{ads} , were used to find the adsorption rate constant, k_a , from (3.22). Figure 3.15 displays the rate constants versus concentration for each surfactant tested. Within error, the adsorption rate constants were independent of the surfactant concentration. All three of the Span molecules exhibited adsorption rate constants within a factor of ten of each other.

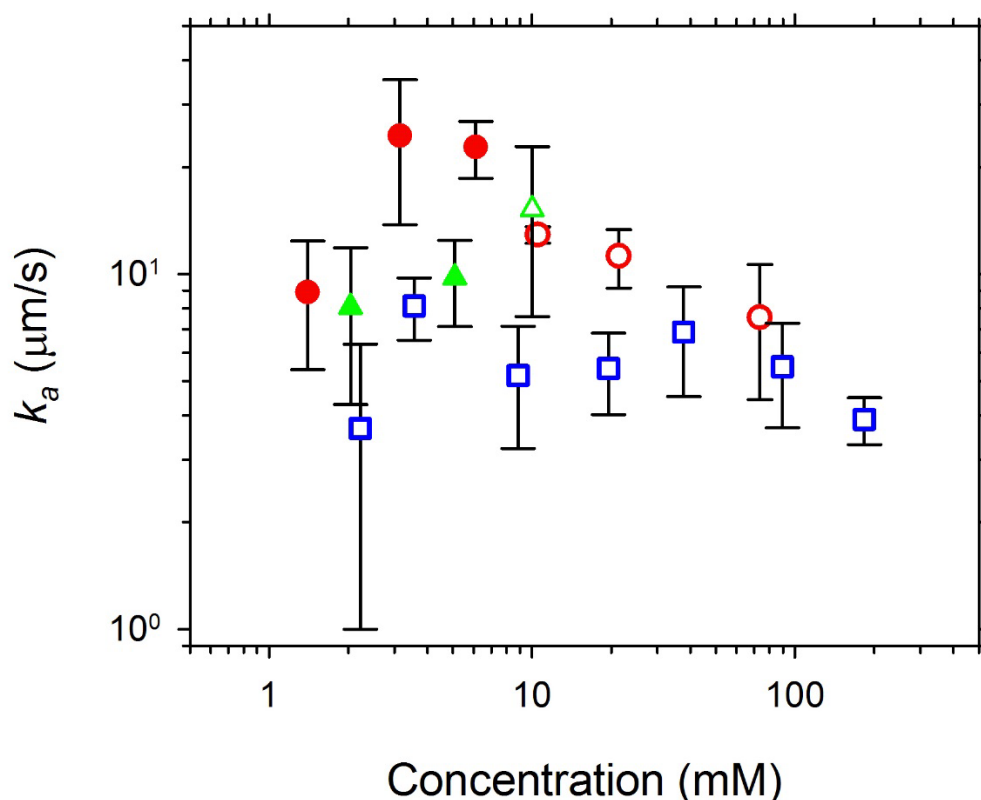


Figure 3.15. The charge adsorption rate constant, k_a , is plotted versus surfactant concentration for Span 20[®] (red circles), Span 80[®] (blue squares), and Span 85[®] (green triangles) in dodecane. The charge adsorption rate is not dependent on surfactant concentration. There is not a large change in the adsorption rate constant above the CMC (open) and below the CMC (filled).

The desorption rate constant, τ_D , was found from the adsorption capacitance, C_{ads} , and the other parameters used in (3.23). The desorption rates of Span 85[®] at

some low concentrations of Span 20[®] and Span 80[®] could not be determined because the lowest experimental frequency of 10^{-2} Hz was not low enough to accurately determine the adsorption capacitance, C_{ads} . The desorption rates displayed in Figure 3.16 show that the desorption time constant is inversely proportional to the surfactant concentration. The rate constants in kinetic equations like (3.6) and (3.7), which are based on the law of mass-action, should not depend on the concentration of reactants or products. The systematic dependence of the desorption rate constant τ_D on bulk surfactant concentration suggests that the desorption process involves a species from the fluid — not just the adsorbed species whose concentration is Γ_{\pm} . One possibility is that the charged species which is adsorbing and desorbing is a single surfactant molecule or small ion like H^+ — not the entire charged micelle which acts as a carrier in the bulk. Then, in order to desorb a stable charged species, the single surfactant molecule or small ion must combine with a neutral micelle from the bulk. If so, then the desorption process involves the combination of two species instead of one and the kinetic expressions (3.6) and (3.7) might be replaced by

$$\frac{d\Gamma_{\pm}}{dt} = k_a n_{\pm} - k_d n_0 \Gamma_{\pm}$$

where n_0 is the concentration of neutral micelles which might be approximately the total concentration of surfactant divided by the average aggregation number for the micelles. Clearly then $k_d n_0$ is expected to be proportional to the total

surfactant concentration while $\tau_D = (k_d n_0)^{-1}$ is expected to be inversely proportional to the concentration — as shown in Figure 3.16.

The rate constants k_d and τ_D might each take on different values for anions and cations even though we have assumed the oppositely charge species respond similarly in this study. As with the assumption of equal diffusion coefficients for anions and cations, the assumed model expressed all of the qualitative features of the impedance spectra with a minimum number of adjustable parameters. The twin assumptions of equality of diffusion coefficients and reaction parameters do not imply that these properties of the anion and cation are in fact equal; the reality is that the observed impedance spectra do not contain discernible evidence of different values for cation and anion.

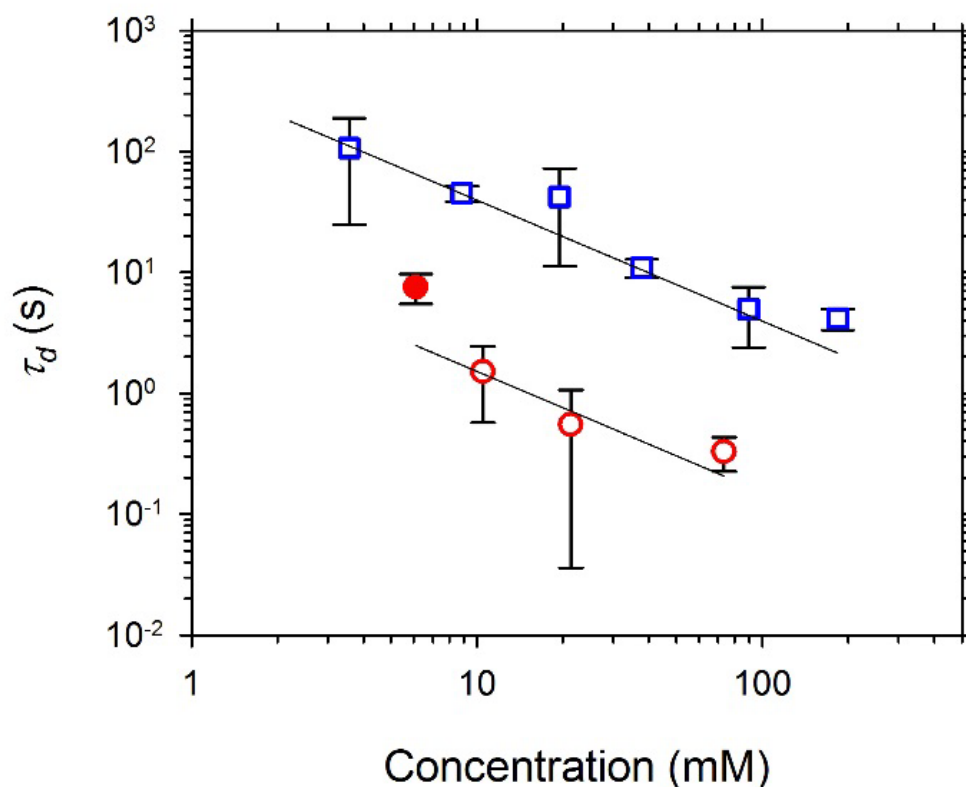


Figure 3.16. Desorption rate constants versus surfactant concentration for Span 20[®] (circles) and Span 80[®] (squares) in dodecane. The desorption rate was found from the adsorption capacitance, which could only be found accurately from the impedance of Span 80[®] and Span 20[®] at concentrations above their respective CMCs. The desorption rate is dependent on surfactant concentration suggesting that the concentration of uncharged surfactant is involved in facilitating the desorption kinetics. The solid trend lines have a slope of -1.

3.4.8. Implications for the origin of charge in solutions involving Span surfactants

The surface charge densities at equilibrium can then be calculated from the charge concentration and the adsorption length by (3.9). For Span 80[®], the average surface charge density was 7000 charge carriers per μm^2 . At equilibrium there are assumed to be an equal number of positive and negative charge carriers on the electrode, which implies that the total charge density on the electrode is $2\Gamma^*_{\pm}$. Taking the reciprocal of the total charge density gives an area per adsorbed

charge of $70 \text{ nm}^2/\text{charge}$. This result means that on average there is one adsorbed charge on the electrode for every $8 \text{ nm} \times 8 \text{ nm}$ square area. While this area per charge is larger than the area that an adsorbed inverse micelle would occupy, this result suggests a significant fraction of the electrode surface is covered with charged inverse micelles. This scenario is improbable because only a small fraction of inverse micelles acquire charge in the bulk. A second explanation for the large values of charge density is that the surface species is a charged surfactant molecule or a small ion as mentioned in the previous section.

Following the sketch in Figure 3.17, the adsorbed charge is pinned at the interface by uncharged surfactant but can dissociate by solvation in the core of nearby uncharged micelles. Charge in nonpolar liquids is believed to originate from dissociable ion pairs within the bulk solvent or surfactant; however, the large surface concentrations in our measurements suggest that the dissociable species might be pinned to the surfaces. The interaction between surfaces and uncharged micelles is able to transfer charge into the bulk thus creating charge in doped nonpolar liquids. This mechanism of charge creation due to desorption from the electrode surfaces might also explain results from other experiments with doped nonpolar liquids. For example, the “destruction” of charge in solution by deposition on a solid, the opposite direction, certainly has been observed [34].

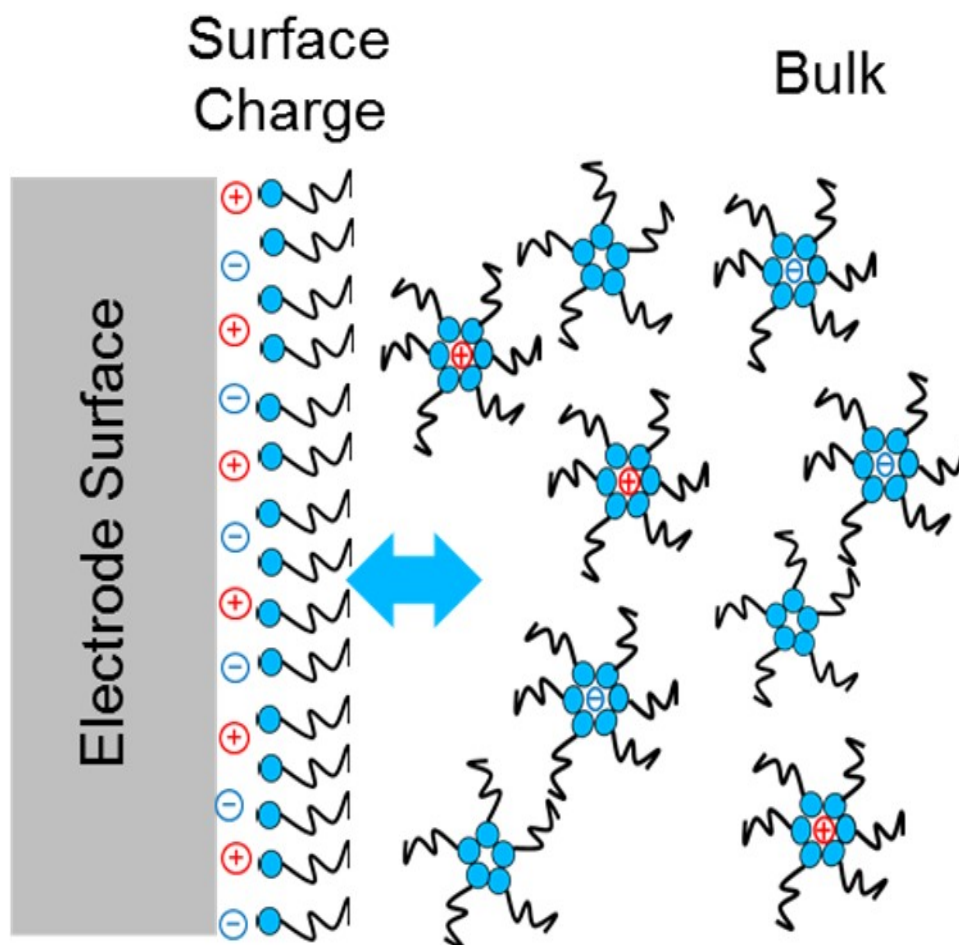


Figure 3.17. Possible schematic of charge adsorption mechanism between surfactant at the electrode-liquid interface and micelles in the bulk.

3.4.9 Comparison to a potentiostatic experiment

The adsorption/desorption model also can be used to interpret of potentiostatic experiments. Karvar et al. [14] showed the current response of various surfactants in dodecane when a constant voltage was applied across thin parallel plate electrodes. The current passing through a 0.1% wt. Span 80[®] solution in contact with ITO electrodes with 5V applied was digitized from [14]

and re-plotted in Figure 3.18. The blue circles are the digitized experimental data and the solid black line is the simulated current found by solving the Poisson-Nernst-Planck equations without adsorption using the parameters listed by Karvar et al.[14] for 0.1 wt.% Span 80[®] in dodecane which included a charge concentration of 20.8 charges/ μm^3 , an electrophoretic mobility of $\pm 1.50 \times 10^{-9} \text{ m}^2\text{V}^{-1}\text{s}^{-1}$, and a charge carrier radius of 4.09 nm. The dashed red line is a simulated current response allowing for charge adsorption using the same parameters from Karvar et al.[14] and a best fit value for the adsorption rate constant of $30 \mu\text{m}^3\text{s}^{-1}$ and a desorption constant of 200 s. The good agreement obtained with the adsorption/desorption model suggests that this same physical phenomenon can be observed in both small amplitude impedance measurements and large voltage DC measurements.

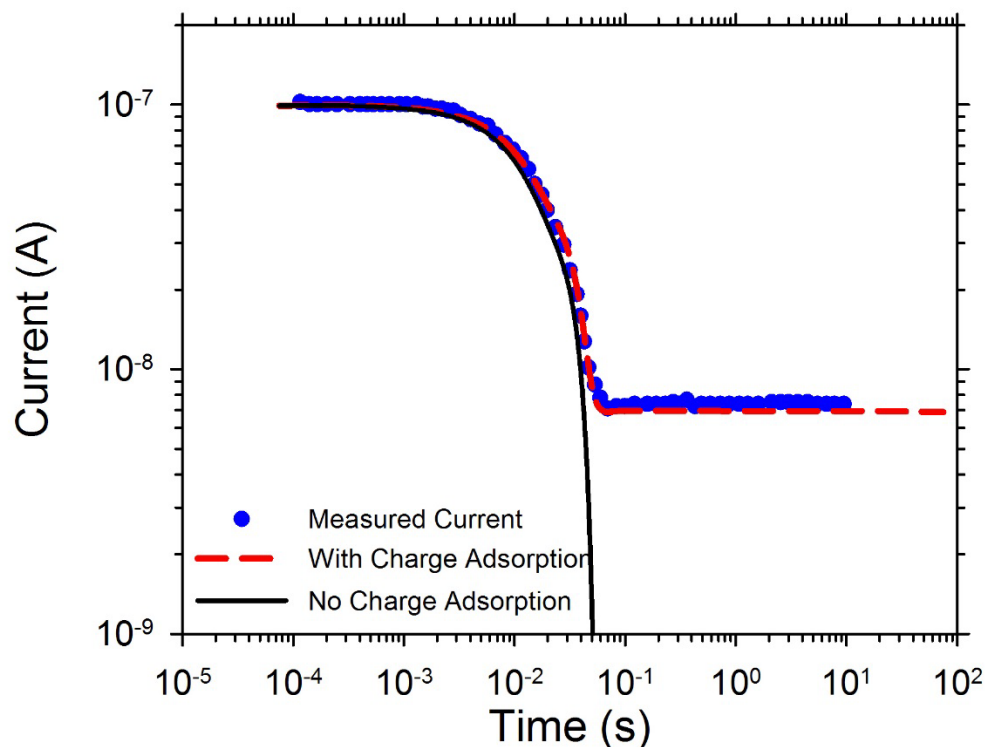


Figure 3.18. Potentiostatic data for 0.1% Span 80[®] in dodecane in a thin cell with ITO electrodes and 5V applied (blue circles) taken from [14] (fig.2). The solid black line is the transport model simulation without charge adsorption. The dashed red line is the transport model simulation with charge adsorption using the conditions presented in this work.

3.5 Conclusions

We investigated the small amplitude AC response of three different nonionic Span surfactants in dodecane. The electrical impedance was determined over 7 orders of magnitude of frequency. The major findings were the following:

- The impedance spectra of Span 85[®], Span 80[®], and Span 20[®] in dodecane were qualitatively different from OLOA 11000[®] in the same

solvent. A second semicircle at low frequencies appeared in the Nyquist plots.

- The impedance spectra of each surfactant was expressed by an equivalent circuit model accounting for charge adsorption and desorption at the electrode interface.
- The equivalent circuit can mimic the solution to the linearized PNP equations, provided the Debye length is less than 10% of the electrode separation.
- The circuit elements were used to find the conductivity, dielectric constant, Debye length, bulk charge concentration, charge diffusion coefficient, adsorption rate constant and desorption rate constant
- Above the CMC the conductivities of solutions with surfactant added were linear with surfactant concentration
- The ratio of charge per surfactant molecule for Span 20[®] is 22 ppm, 3 ppm for Span 80[®], and 0.2 ppm for Span 85. The mobilities of Span 20[®] were much lower, indicating that the charge bearing species in Span 20[®] are larger, which facilitates charge stabilization.
- The adsorption rate was proportional to the surfactant concentration, while the desorption rate was found to be proportional to the product of the surfactant concentration and surface excess. This desorption rate suggests that the desorption process involves neutral micelles.

- The transport model described potentiostatic measurements from the literature [14] when adsorption and desorption was added to the boundary conditions.

The origin of charge in nonpolar liquids is believed to come from dissociable ion pairs in the solvent or surfactant, however the large surface concentrations shown in these measurements suggest that the dissociable species may be pinned to the surfaces. The interactions between surfaces and uncharged micelles is able to dissociate charge into the bulk thus providing a source for charge creation in doped nonpolar liquids.

3.6 Acknowledgement

We thank Thomas R. Walker for help the impedance spectroscopy experiments. We also gratefully acknowledge financial support for this project from the Dow Chemical Company.

3.7 References

1. Klinkenberg, A. and J.L. van der Minne, *Electrostatics in the Petroleum Industry: The Prevention of Explosion Hazards*. 1958, New York: Elsevier.
2. Morrison, I.D., *Electrical charges in nonaqueous media*. Colloids and Surfaces A: Physicochemical and Engineering Aspects, 1993. **71**: p. 1-37.
3. Chen, Y., et al., *Flexible active-matrix electronic ink display*. Nature, 2003. **423**: p. 136.

4. Poovarodom, S. and J.C. Berg, Effect of particle and surfactant acid-base properties on charging of colloids in apolar media. *J Colloid Interface Sci*, 2010. **346**(2): p. 370-7.
5. Novotny, V., *Applications of Nonaqueous Colloids*. Colloids and Surfaces A: Physicochemical and Engineering Aspects, 1987. **24**: p. 361-375.
6. Schmidt, J., et al., Conductivity in nonpolar media: experimental and numerical studies on sodium AOT-hexadecane, lecithin-hexadecane and aluminum(III)-3,5-diisopropyl salicylate-hexadecane systems. *J Colloid Interface Sci*, 2012. **386**(1): p. 240-51.
7. Tetley, K.E. and D. Lee, Effect of thermal treatment and moisture content on the charge of silica particles in non-polar media. *Soft Matter*, 2013. **9**: p. 7242-7250.
8. Gomez-Diaz, D., J.C. Mejuto, and J.M. Navaza, Density, Viscosity, and Speed of Sound of Solutions of AOT[®] Reverse Micelles in 2,2,4-Trimethylpentane. *J. Chem. Eng. Data*, 2006. **51**: p. 409-411.
9. Novikov, G.F., et al., *The impedance of solutions of AOT/water micelles in hexane*. *Russian Journal of Physical Chemistry A*, 2007. **81**(12): p. 2030-2034.
10. Karvar, M., et al., Transport of Charged Aerosol OT Inverse Micelles in nonpolar Liquids. *Langmuir*, 2011. **27**: p. 10386-10391.
11. Espinosa, C.E., et al., Particle charging and charge screening in nonpolar dispersions with nonionic surfactants. *Langmuir*, 2010. **26**(22): p. 16941-8.
12. Guo, Q., V. Singh, and S.H. Behrens, *Electric charging in nonpolar liquids because of nonionizable surfactants*. *Langmuir*, 2010. **26**(5): p. 3203-7.
13. Dukhin, A.S. and P.J. Goetz, How non-ionic "electrically neutral" surfactants enhance electrical conductivity and ion stability in non-polar liquids. *Journal of Electroanalytical Chemistry*, 2006(588): p. 44-50.
14. Karvar, M., et al., Investigation of Various Types of Inverse Micelles in Nonpolar Liquids Using Transient Current Measurement. *Langmuir*, 2014. **30**: p. 12138-12143.

15. Gacek, M.M. and J.C. Berg, Effect of surfactant hydrophile-lipophile balance (HLB) value on mineral oxide charging in apolar media. *J Colloid Interface Sci*, 2015. **449**: p. 192-197.
16. Dukhin, A.S. and S. Parlia, Ion-Pair Conductivity Theory Fitting Measured Data For Various Alcohol-Toluene Mixtures across Entire Concentration Range. *Journal of the Electrochemical Society*, 2015. **162**(4): p. H256-H263.
17. Yezer, B.A., et al., Use of electrochemical impedance spectroscopy to determine double-layer capacitance in doped nonpolar liquids. *J Colloid Interface Sci*, 2015. **449**: p. 2-12.
18. Prieve, D.C., et al., Two Independent Measurements of Debye Lengths in Doped Nonpolar Liquids. *Langmuir* 2008. **24**: p. 1120-1132.
19. Beunis, F., et al., Inverse micelles as charge carriers in nonpolar liquids: Characterization with current measurements. *Current Opinion in Colloid & Interface Science*, 2013. **18**(2): p. 129-136.
20. Beunis, F., et al., *Dynamics of charge transport in planar devices*. *Physical Review E*, 2008. **78**.
21. Kim, J., et al., Ionic Conduction and Electrode Polarization in a Doped Nonpolar Liquid. *Langmuir*, 2005. **21**: p. 8620-8629.
22. Kornilovitch, P. and Y. Jeon, *Transient electrophoretic current in a nonpolar solvent*. *Journal of Applied Physics*, 2011. **109**(6): p. 064509.
23. Beunis, F., et al., *Electric charging of inverse micelles in a nonpolar liquid with surfactant*. *Colloids and Surfaces A: Physicochemical and Engineering Aspects*, 2014. **440**: p. 10-19.
24. Strubbe, F., et al., *Generation current of charged micelles in nonaqueous liquids: measurements and simulations*. *Journal of Colloid and Interface Science*, 2006. **300**(1): p. 396-403.
25. Grafov, B.M. and V.V. Elkin, *Impedance spectroscopy of an ideally polarizable electrode*. *J. Electroanal. Chem.*, 1991. **304**: p. 31-40.
26. Barbero, G., Influence of adsorption phenomenon on the impedance spectroscopy of a cell of liquid. *Physical Review E*, 2005. **71**.
27. Hunter, R.J., *Foundations of Colloid Science*. Vol. 1. 1987, Oxford: Clarendon Press.

28. Orazem, M.E., et al., *Dielectric Properties of Materials Showing Constant-Phase-Element (CPE) Impedance Response*. Journal of the Electrochemical Society, 2013. **160**(6): p. C215-C225.
29. Orazem, M.E. and B. Tribollet, *Electrochemical Impedance Spectroscopy*. 2008, Hoboken, NJ: Wiley.
30. Brug, G.J., et al., The Analysis of Electrode Impedances Complicated By the Presence of a Constant Phase Element. Journal of Electroanalytical Chemistry, 1984. **176**: p. 275-295.
31. Lelidis, I. and G. Barbero, Effect of different anionic and cationic mobilities on the impedance spectroscopy measurements. Physics Letters A, 2005. **343**: p. 440-445.
32. Bondarenko, A.S. and G.A. Ragoisha, *Inverse Problem in Potentiodynamic Electrochemical Impedance*, in *Progress in Chemometrics Research*, A.L. Pomerantsev, Editor. 2005, Nova Science Publishers: New York. p. 89-102 (the program is available online at <http://www.abc.chemistry.bsu.by/vi/analyser/>).
33. Michor, E.L. and J.C. Berg, Extension to the Charge Fluctuation Model for the Prediction of the Conductivity of Apolar, Reverse Micellar Systems. Langmuir, 2012. **28**: p. 15751-15755.
34. Dukhin, A.S. and S. Parlia, *Ions, ion pairs and inverse micelles in non-polar liquids*. Current Opinion in Colloid & Interface Science, 2013. **18**: p. 93-115.

3.8 Appendix: A physical circumstance leading to a CPE

To better understand the need for CPE's, consider the following example: the dynamic response of current through a simple capacitor C_{dl} in series with a simple resistor R_f is characterized by a single time constant given by $R_f C_{dl}$. Suppose in our parallel-plate fluid cell (see Figure 3.3), the plates are not quite parallel. Instead of a single uniform thickness L over the entire electrode area, the local gap varies slowly with position over the electrode surface. Recall from

(3.20) that R_f is proportional to L . If we used something like the lubrication approximation to solve the new 2-D or 3-D transport problem across the electrically neutral bulk solution, the equivalent circuit is a large set of resistors (each in series with two capacitors having capacitance per unit area of C_{dl}/A_f) acting in parallel, where the resistors have different resistances in proportion to the local gap. This more complicated circuit would give rise to a distribution of time constants $R_f C_{dl}$ instead of a single value. Simply put, a CPE is a single circuit element that expresses a large parallel set of resistors and capacitors.

Chapter 4 Increase in Conductivity with Micelle Size of Surfactant Solutions in Dodecane

4.1 Introduction

Oil soluble amphiphilic surfactant molecules can often aggregate to form structures called “inverse micelles” or just “micelles” in nonpolar liquids. [1-5] The addition of these micelle forming surfactants such as Aerosol-OT[®] (AOT) in nonpolar solvents can increase the electrical conductivity of the solution and also generate charge on solid surfaces.[6, 7] The micelles have a hydrophilic core that can aid in the solubilization and dissociation of free charge thus increasing the conductivity of the solution.[8] Many studies have disputed the mechanisms that control the formation charge in these micellar solutions.[9-14] The three most common mechanisms to describe charge formation in nonpolar liquids include charge fluctuation, disproportionation, and ion-pair dissociation.[11]

The charge fluctuation model predicts the effect of water content on the conductivity of micro-emulsions. The model postulates that the number of charged-droplet carriers is limited by the work required to give a positive and negative charge to two equally sized neutral droplets.[7, 11, 15, 16] This model has been successfully used to predict the conductivity not only of micro-emulsions containing significant water but also of micelles in nonpolar liquids

with very little added water.[12, 13, 17] Most previous work has shown the effectiveness of the model for only one particular surfactant in a nonpolar solvent as a function of added water. In this work, the conductivity and charge carrier concentrations of five different commercial surfactants were measured with impedance spectroscopy and compared with predictions made from the charge fluctuation model.

4.2 Theory

The Bjerrum length, λ_B is a critical length scale in determining the conductivity in nonpolar liquids. The Bjerrum length is the length scale that two point charges of valence z and $-z$ need to be separated in medium of permittivity $\epsilon\epsilon_0$ for the electrostatic potential energy to be equal to thermal energy,

$$\lambda_B = \frac{z^2 e^2}{4\pi\epsilon\epsilon_0 k_B T} \quad (4.1)$$

where e is the elementary charge, k_B is the Boltzmann constant, and T is the temperature. As derived by Hall[7] and corrected for micro-emulsion droplets the ratio of the concentration of charged micelles, C_{\pm} , to the concentration of total micelles, C_m , is given by

$$\frac{C_{\pm}}{C_m} = \exp\left(-\frac{\lambda_B}{2a}\right) \quad (4.2)$$

where a is the radius of the hydrated core of the micelle. Assuming that the positive and negative droplets are monovalent and have the same size, an expression for the conductivity, K , can be found assuming the droplets are spherical with hydrodynamic diameter, d_h , that follows the Stokes-Einstein relation,

$$K = \frac{2e^2 C_{\pm}}{3\pi\eta d_h} = \frac{2e^2 C_m}{3\pi\eta d_h} \exp\left(-\frac{\lambda_B}{2a}\right), \quad (4.3)$$

where η is the viscosity of the solution. Assuming that the concentration of the surfactant in the micelle solution is by definition above the critical micelle concentration (CMC) and that the micelles have a constant aggregation number, N_{agg} , an expression can be written for the conductivity as a function of the surfactant concentration, C_s ,

$$K = \frac{2e^2 N_{agg} C_s}{3\pi\eta d_h} \exp\left(-\frac{e^2}{8a\pi\epsilon\epsilon_o k_B T}\right). \quad (4.4)$$

Accordingly, if we assume that the hydrodynamic diameter, aggregation number, and hydrated core of the micelles are independent of surfactant concentration it can be shown that the conductivity should increase linearly with surfactant concentration,

$$\frac{dK}{dC_s} = \frac{2e^2 N_{agg}}{3\pi\eta d_h} \exp\left(-\frac{e^2}{8a\pi\epsilon\epsilon_o k_B T}\right). \quad (4.5)$$

An important consequence of the charge fluctuation theory is that the only the aggregation number, hydrodynamic diameter, and hydrated core radius of the surfactant micelles effects the conductivity of the solution. This would suggest that ionic surfactants, nonionic surfactants, small molecule surfactants, and polymeric surfactants should all follow this simple framework. In this work, the charge fluctuation model presented above will provide a basis for analyzing data from impedance spectroscopy measurements for solutions of AOT[®], OLOA 11000[®], Span 85[®], Span 80[®], and Span 20[®] in dodecane. In addition, measurements made with a conductivity meter of solutions of Span 85[®], Tergitol NP-4[®], Triton X-15[®], Tergitol TMN-3[®], and Tergitol 15-S-3[®] in dodecane will be compared to the predictions laid out by the charge fluctuation theory.

4.3 Materials and Methods

4.3.1 Solution Preparation- Common Oil Soluble Surfactants

Surfactant solutions of OLOA 11000[®] (Chevron Oronite), Aerosol-OT[®] (AOT) (Sigma), Span 85[®] (Sigma), Span 80[®] (Sigma), and Span 20[®] (Sigma) were prepared in anhydrous dodecane (Sigma-Aldrich) at concentrations ranging from 1 to 100 mM. The solutions were sonicated for 30 minutes and stored in a desiccator for at least one day before measurements were taken. No additional steps were made to purify the commercial surfactants. These particular surfactants were selected for their known ability to form micelles in dodecane and increase the electrical conductivity of nonpolar liquids.

4.3.2 Phase analysis light scattering

A ZetaSizer Nano (Malvern) was used to conduct phase analysis light scattering (PALS) on the surfactant solutions. One milliliter of solution was added to a quartz cuvette that was compatible with the nonpolar solvent. Each measurement was made with 10 mM of surfactant in dodecane for the solutions of The light scattering was performed over a longer 60 second period rather than the 30 second default period to decrease noise in the measurement. Each run consisted of at least 10 different measurements and the results were averaged over the individual measurements. At least three runs were performed for each surfactant solution and the distributions were averaged over the three runs.

4.3.3 Impedance spectroscopy

Thin-cell impedance spectroscopy was performed with the surfactant solutions following the procedure outlined in previous work.[18, 19] The impedance results from AOT[®], Span 85[®], Span 80[®], and Span 20[®] were fit with an equivalent circuit model that includes charge adsorption at the electrode surface. There was no evidence of charge adsorption in the impedance results from the OLOA 11000[®] solutions. A 127 μm thick gasket was machined out of a polycarbonate sheet (McMaster-Car) to create a “thick cell” in order to accurately determine the conductivity in the low concentration range AOT[®] in dodecane. The gasket has a set area of 10 cm^2 and filled with a Pasteur pipette during each thick cell measurement.

4.3.4 Less common nonionic surfactants

In addition to the well-known charge dispersants, the relationship between conductivity and micelle size was studied for a series of nonionic surfactants that have not previously been shown to increase charge in nonpolar liquids. Solutions ranging from 0.1 to 5% wt. of four other commercial surfactants Tergitol NP-4[®], Triton X-15[®], Tergitol TMN-3[®], and Tergitol 15-S-3[®] (Dow Chemical) were prepared in dodecane. The size of any micelles formed in these solutions was measured with PALS over the entire concentration range studied since the micellization behavior of these surfactants in nonpolar liquids has not been well studied.

4.3.4 Nonaqueous Conductivity Meter

A DT-700 (Dispersion Technology) nonaqueous conductivity meter was used to measure the conductivity of solutions of Span 85[®], Tergitol NP-4[®], Triton X-15[®], Tergitol TMN-3[®], and Tergitol 15-S-3[®] in dodecane. About 10 mL of each solution was measured with the probe in a glass test tube.

4.4 Results and Discussion

4.4.1 Light Scattering of Micelles

Phase analysis light scattering (PALS) was used to produce the micelle size distributions shown in Figure 4.1 for 10 mM surfactant solutions in dodecane. This concentration was chosen to be above the critical micelle concentration (CMC), yet low enough to avoid interference from multiple scattering. The

intensity distributions are shown in Figure 4.1a while the number distribution is plotted in Figure 4.1b. The peaks at the lowest size of each curve in the intensity distributions is due to the micelles in solution while the peaks at higher diameters are most likely due to dust or other contaminants. When the size bias is removed from the intensity data and replotted as the number distribution (Figure 4.1b) the larger peaks disappear and only the smaller peak remains. The size of the micelles was in between 1 nm and 20 nm. The average micelle diameters from the intensity distributions in Figure 4.1a are listed in Table 4.1 with the standard error found from the peak width of the intensity distributions. The OLOA 11000[®] solutions were the largest micelles while the solutions of AOT[®] in dodecane formed the smallest micelles.

Previous work has shown that the micelle size increases with the water content of the solution as the micelles must swell to take up the water.[14, 15] In this work, no water was added to the solutions; they were stored in a desiccator when not in use. No attempts were made to remove any initial water content in the solvent or surfactants. The measurements of light scattering were often performed days after the impedance spectroscopy was performed. For the purposes of comparison, we assume that the micelle size of the solutions was the same as tested with light scattering as when measured with impedance spectroscopy.

Additionally, previous studies have shown that Span 80[®] may form non-spherical micelles in dodecane at high concentrations.[20] The phase analysis

light scattering of the 10 mM solution of Span 80[®] in dodecane in Figure 4.1 reports the longer dimension of a rod-shaped micelle.

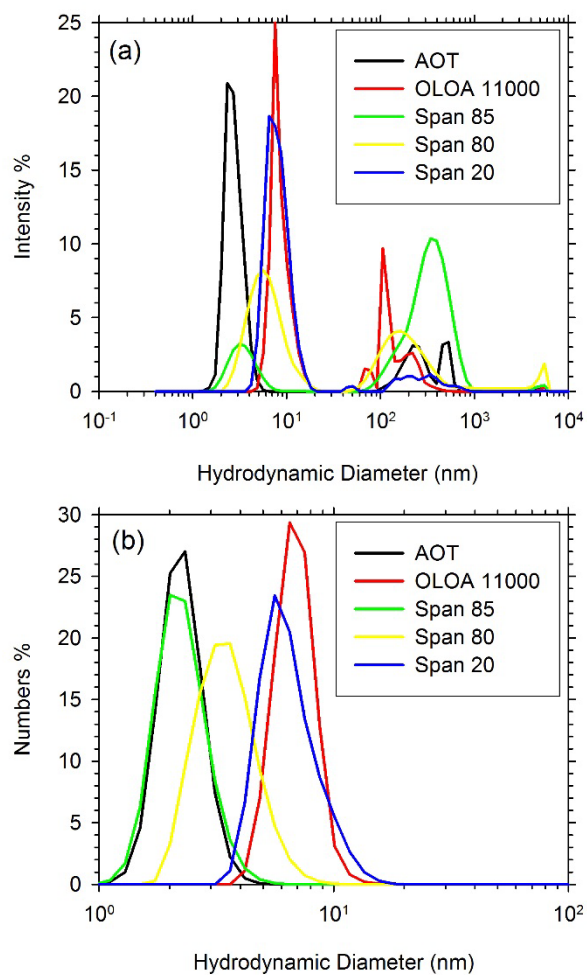


Figure 4.1. Phase analysis light scattering data of surfactants in dodecane shown with intensity distribution (A) and number distribution (B). Each surfactant was 10 mM in dodecane for AOT[®] (black), OLOA 11000[®] (red), Span 85[®] (green), Span 80[®] (yellow), and Span 20[®] (blue).

Table 4.1. Results from phase analysis light scattering of micelles in dodecane

Surfactant in Dodecane	Hydrodynamic diameter, d_h (nm)	Tail Length (nm)	Estimated diameter of the polar core (nm)
AOT	2.8 ± 1.4	0.7 [14]	1.4 ± 1.4
OLOA 11000	8.6 ± 1.5	2.81 [14]	3.0 ± 1.5
Span 85	3.5 ± 1.3	1.7	0.14 ± 1.3
Span 80	6.3 ± 0.5	1.95 [14]	2.4 ± 0.5
Span 20	8.3 ± 2.2	1.7	4.9 ± 2.2

4.4.2 Conductivity of Surfactants in Dodecane

Thin-cell impedance spectroscopy was performed on solutions of AOT[®], OLOA 11000[®], Span 85[®], Span 80[®], and Span 20[®] following the procedures previously established doped nonpolar media.[18, 19] The fitted conductivities are plotted in Figure 4.2 at various surfactant concentrations in dodecane. For all cases, the conductivity increased with the addition of surfactant. For some concentrations, the conductivity was proportional to the surfactant concentration, however sharp increases in conductivity were observed at low concentrations of Span 80[®] and Span 20[®] as the concentration increased past the critical micelle concentration for the reverse micelles (about 10 mM for both Span 20[®] and Span 80).

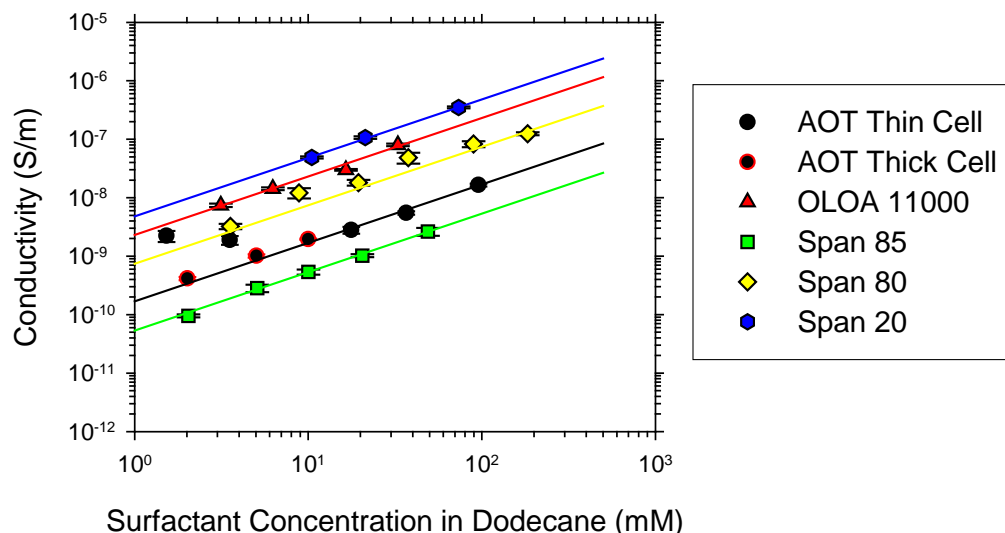


Figure 4.2. Conductivity measurements obtained from impedance spectroscopy versus surfactant concentration in mM. The surfactants measured were AOT[®] (black circles), OLOA 11000[®] (red triangles), Span 85[®] (green squares), Span 80[®] (yellow diamonds), Span 20[®] (blue hexagons). Measurements were made in a 10 μm thin cell except for the AOT[®] (black circles, red edges) measured in a 125 μm thick cell. Solid lines are best-fit linear curves.

The lines on Figure 4.2 are linear fits relating the conductivity to surfactant concentration above the CMC.[4, 13, 20, 21] The slopes of these curves were taken as the molar conductance of the surfactants in dodecane above the CMC and listed with the standard error from fitting in Table 4.2.

The AOT[®] in dodecane solutions (red circles) include both data using a 10 μm “thin” cell (black edge) and a 125 μm “thick cell. At concentrations of AOT[®] below 10mM a deviation was observed between the “thin” cell and “thick” cell measurements. This difference is due to the failure of the adsorption circuit model when the Debye length approaches the gap distance of the cell as described in previous work.[19] The conductivity measurements made with the thicker cell are more accurate at low concentrations of surfactant because the circuit model

used to fit the impedance data is valid for a wider range of concentrations. As shown with the thick cell measurements, the conductivity should linear for AOT[®] in dodecane over the concentration range tested since the concentration is above the critical micelle concentration (CMC).[22]

4.4.3 Ionic Strength

The charge carrier concentration plotted in Figure 4.3 was calculated from the Debye length measured with thin cell impedance spectroscopy at concentrations above the known CMC. The solid lines were fit to the high concentrations above the CMC assuming the charge concentration is linear with surfactant concentration in this region. The fitted slopes were converted to a ratio of charge carriers per surfactant displayed in Table 4.2. The standard error from fitting was fairly low in the solutions of OLOA 11000[®], Span 20[®], and Span 80[®], but very high for the solutions of Span 85[®] and AOT[®] due to difficulties in fitting the adsorption model as described in previous work.[19] Two local maxima in the imaginary impedance were observed for solutions of AOT[®] in dodecane indicating the presence of charge adsorption on the ITO coated glass slides.[19] The presence of charge adsorption masked the double layer capacitance when measurements were made with a thick cell so only a thin 10 μm cell could be used to infer the Debye length, charge concentration, and diffusivity of charge carriers for these solutions.

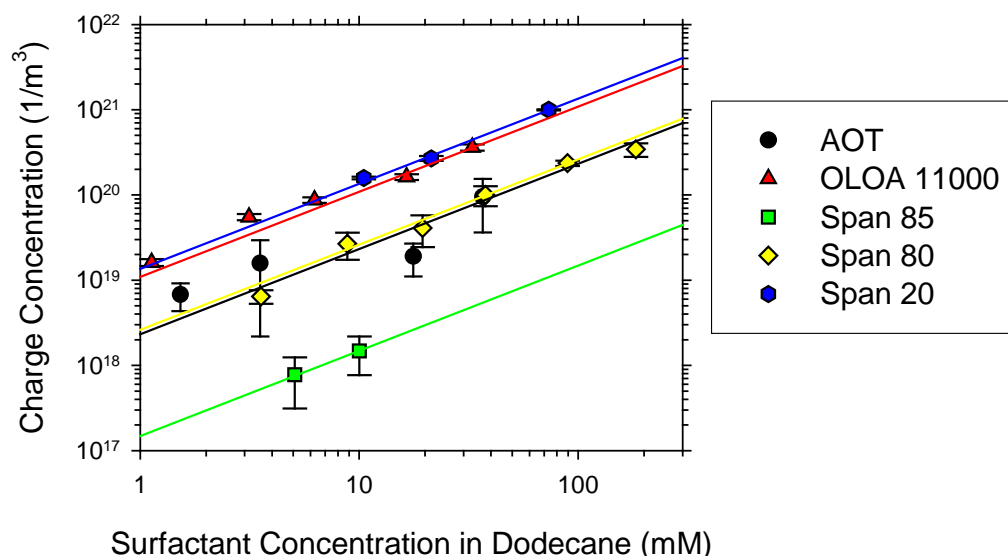


Figure 4.3. Charge concentrations of different surfactants in dodecane measured with impedance spectroscopy with a 10 μm thin cell. The surfactants measured were AOT[®] (black circles), OLOA 11000[®] (red triangles), Span 85[®] (green squares), Span 80[®] (yellow diamonds), Span 20[®] (blue hexagons). Solid lines are best-fit linear curves.

4.4.4 Molar Conductivity and Micelle Size

The molar conductivity found above the CMC for each surfactant was plotted on a semi-log plot against the hydrodynamic micelle diameter found from PALS in Figure 4.4. The results show some correlation between the conductivity of a solution and the micelle size with the larger micelles having an exponentially larger conductance. Despite a disagreement with the ordering of micelle sizes, a single straight line can be drawn through all the error bars in Figure 4.4 indicating an exponential relationship.

According to the charge fluctuation model (4.4) the ratio of charged micelles to total micelles depends exponentially on the relationship between the Bjerrum length of the solution and the radius of the polar core of the micelle. This

diameter represents the hydrated internal core of the micelles, which is smaller than the hydrodynamic diameter measured with PALS. To account for this difference the diameter of the polar core is estimated for each surfactant micelle by subtracting the hydrodynamic diameter by two times the length of the hydrophobic tails. The tail lengths for OLOA 11000[®], AOT[®], and Span 80[®] were taken from literature[14] while the tail lengths of Span 85[®] and Span 20[®] were estimated from bond lengths using an approximation for alkyl chains in Berg.[23] These estimated diameter of the polar cores are listed in Table 4.2 and plotted against the molar conductivity in Figure 4.5. Adjusting for the tail lengths greatly improves the exponential correlation between the molar conductance and micelle size. As the micelle size changes depending on the type of the surfactant, the molar conductivity is greater exponentially greater for larger micelles. Adjusting the hydrodynamic radius to estimate the polar core of the micelle follows the correction to the fluctuation theory in [16] that correctly scales the Bjerrum length with the diameter of the polar core.

Table 4.2. Molar Conductivity and Charge Carriers per surfactant molecule

Surfactant in Dodecane	Molar Conductivity (S/m/mM)	Charge carriers per surfactant (ppm)
AOT	$1.68 \pm 0.05 \times 10^{-10}$	3.9 ± 0.7
OLOA 11000	$2.3 \pm 0.1 \times 10^{-9}$	18.1 ± 0.7
Span 85	$5.3 \pm 0.1 \times 10^{-11}$	0.25 ± 0.04
Span 80	$7.41 \pm 0.8 \times 10^{-10}$	4.3 ± 0.1
Span 20	$4.77 \pm 0.04 \times 10^{-9}$	22.5 ± 0.4

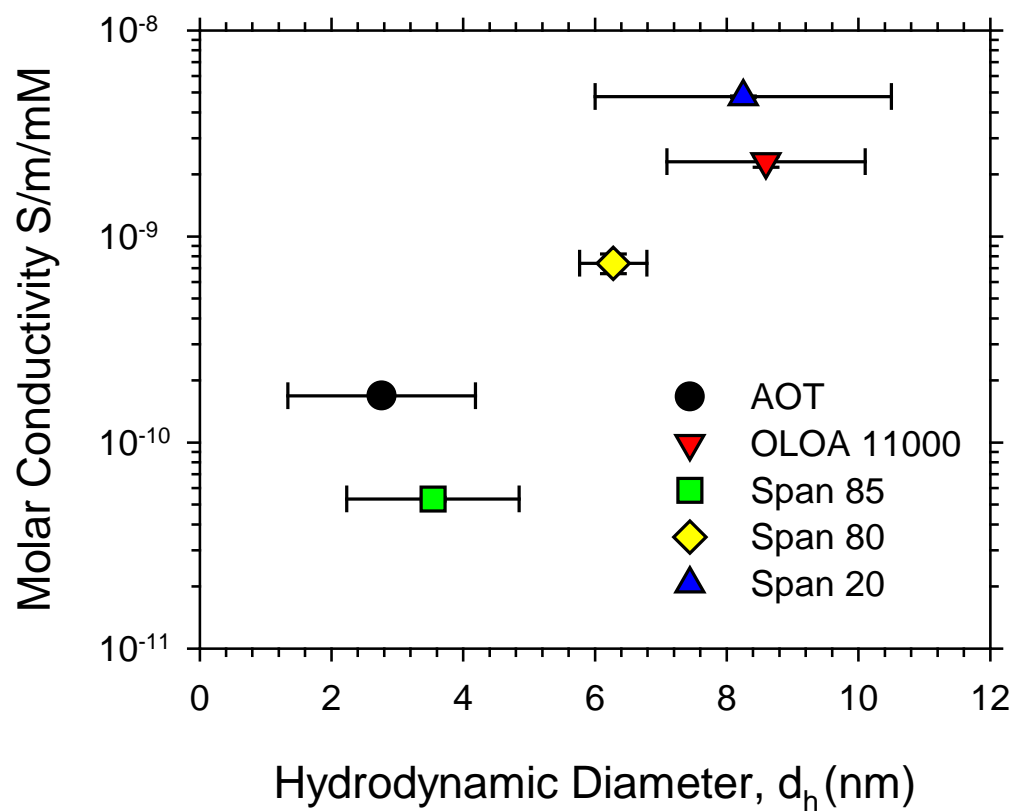


Figure 4.4. Molar conductivity versus hydrodynamic micelle diameter measured from phase analysis light scattering.

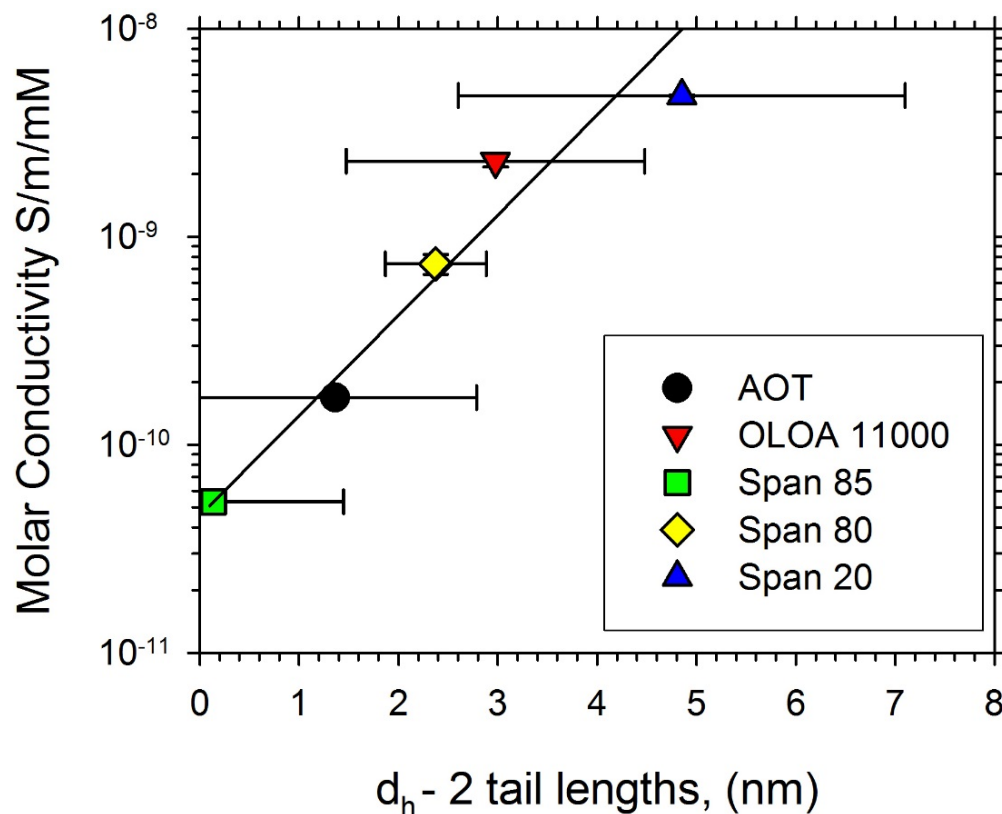


Figure 4.5. Molar conductivity of the surfactant solutions versus the estimated Diameter of the polar core found by subtracting the hydrodynamic diameter by 2 tail lengths. The solid line is the best-fit exponential curve.

4.4.5 Charge Concentration and Micelle Size

The ratio of charge carriers per surfactant molecule, found from Debye length measurements with impedance spectroscopy, is plotted versus the hydrodynamic diameter of each surfactant in Figure 4.6. As with the molar conductivity, we see that the larger micelles form more charge carriers per surfactant molecule. The relationship in (4.2) suggests that the charge concentration per surfactant micelle should vary exponentially with the ratio of the Bjerrum length to the polar core of the micelle. The diameter of the polar micelle core was estimated from the surfactant tail lengths as above and plotted in

Figure 4.7. The solid line is the best-fit exponential relationship drawn to guide the eye and suggests a qualitative agreement to the exponential relationship in (4.2). Errors in this analysis may arise due to the assumptions of the diameter of the polar core, an impact due to the different aggregation numbers for the different micelles, or improper measurements of charge concentration due to non-zero zeta potentials acquired on the electrode surface.

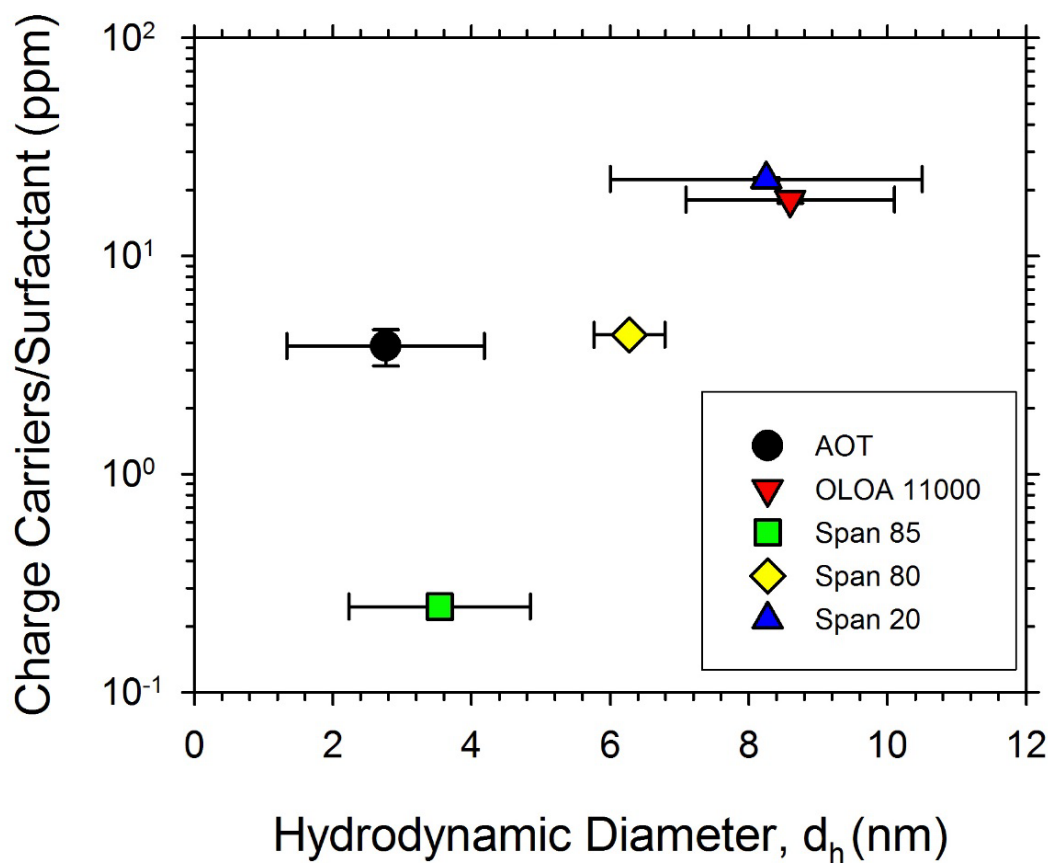


Figure 4.6. Charge carriers per surfactant versus hydrodynamic diameter measured with phase analysis light scattering of 10 mM solutions in dodecane.

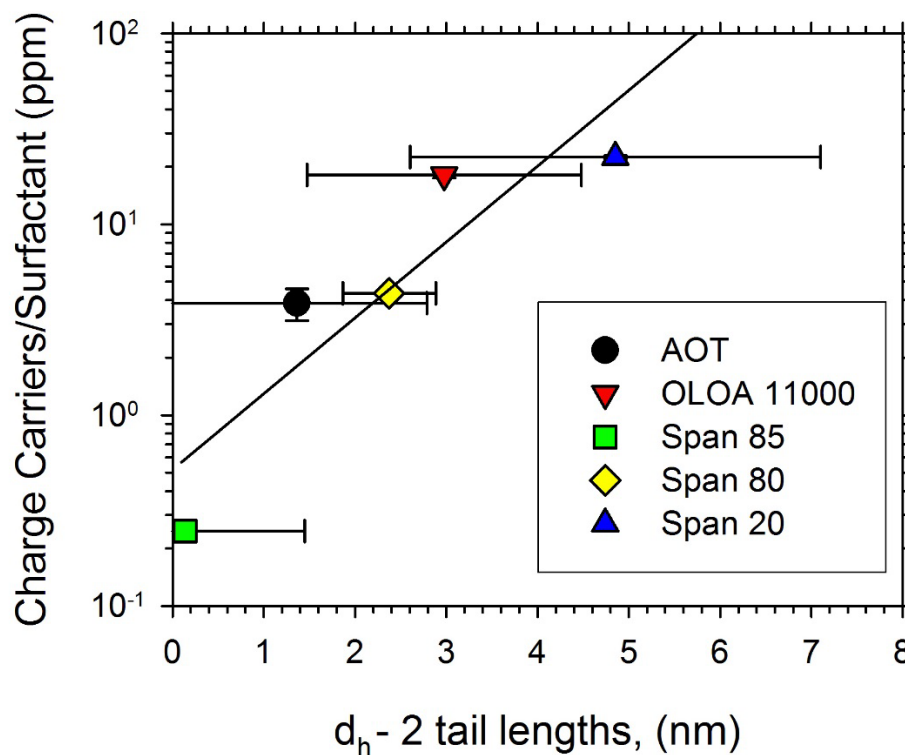


Figure 4.7. Charge carriers per surfactant using versus the estimated hydrated core diameter found by subtracting the hydrodynamic diameter by two times the surfactant tail length. The solid line is the best-fit exponential relationship.

4.4.6 Results from Tergitol NP-4[®] and Triton X-15[®]

In addition to the solutions of dodecane doped with AOT[®], OLOA 11000[®], Span 85[®], Span 80[®], and Span 20[®] discussed above, the conductivities and micelle sizes of Tergitol NP-4[®], Triton X-15[®], Tergitol TMN-3[®], and Tergitol 15-S-3[®] were also studied. Solutions were prepared over a concentration range from 0.1% to 5% wt. in dodecane in the same manner as described above.

The conductivity was measured with a commercial DT-700 conductivity meter (Dispersion Technology) for the different solutions and plotted versus concentration in Figure 4.8. Solutions of Span 85[®] were also prepared and the

conductivity was measured over the same concentration range for comparison. The solutions of Tergitol NP-4[®] were the most conductive of these surfactants tested in dodecane, however these surfactants are much less conductive than Span 20[®] and OLOA 11000[®] discussed previously. Unlike the surfactants presented above, however, the conductivity of Tergitol NP-4[®] rises much faster than linearly in the high concentration range: the slope on log-log coordinates is +3 at high concentration rather than +1. This non-linear increase in conductivity can only follow the fluctuation model in (4.5) if the micelle size increases with concentration.

In order to determine if these surfactants still obey the relationship between conductivity and the diameter of the polar core in equation (4.4), light scattering was performed on the solutions over the same concentration range as the conductivity measurements. Of the 4 surfactants tested, only the Tergitol NP-4[®] and Triton-X 15[®] demonstrated any aggregates with measurable size (using DLS). The size of the measurable micelles is displayed on Figure 4.9 at the measured concentration of surfactant in dodecane. The light scattering data in Figure 4.9 shows that the hydrodynamic diameter of the micelles formed by Tergitol NP-4[®] and Triton-X 15[®] do increase in size with the surfactant concentration. Unlike the micelles studied above, this concentration dependence would result in a non-linear conductivity relationship between conductivity and surfactant according equation (4.5) because the derivative of the conductivity with respect to surfactant

concentration will increase because the diameter of the polar core of the micelles is no longer constant with respect to concentration. Since the aggregation number and the diameter of the polar core are unknown for Tergitol NP-4[®] and Triton-X 15[®] a quantitative fit of the conductivity could not be found, however the non-linear increase in conductivity observed in both Tergitol NP-4[®] and Triton-X 15[®] solutions in Figure 4.8 can be explained qualitative by the increasing micelle size.

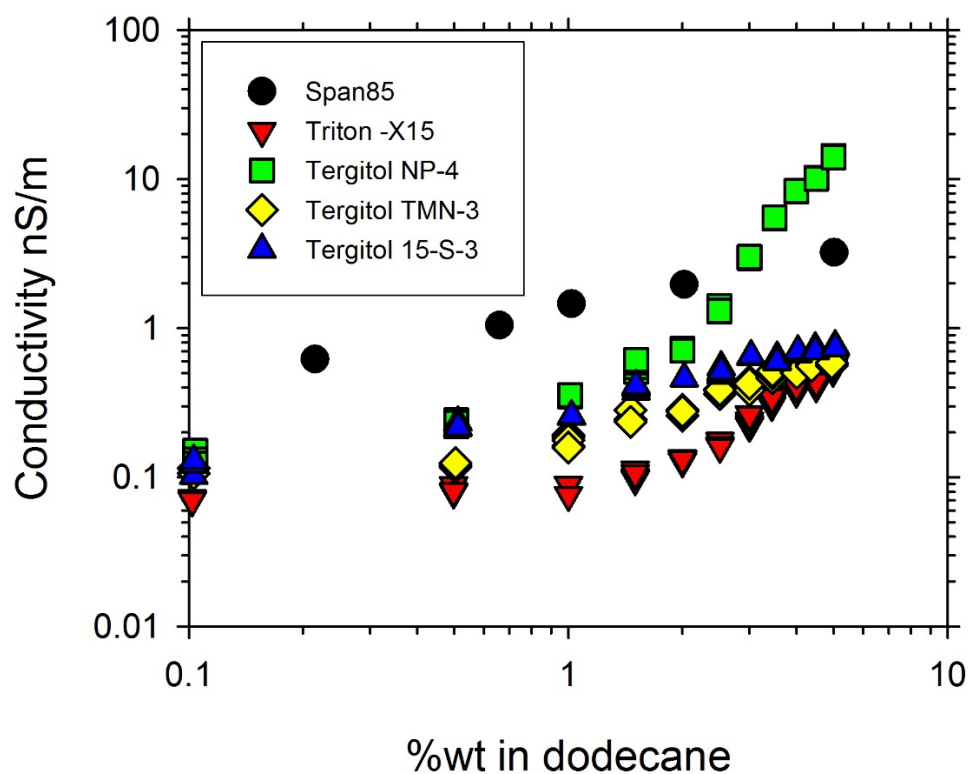


Figure 4.8. Conductivity measurements made with a DT-700 nonaqueous conductivity meter. Solutions of Span 85[®] (black circles), Triton X-15[®] (red triangles), Tergitol NP-4[®] (green squares), Tergitol TMN-3[®] (yellow diamonds), Tergitol 15-S-3[®] (blue triangles) in dodecane.

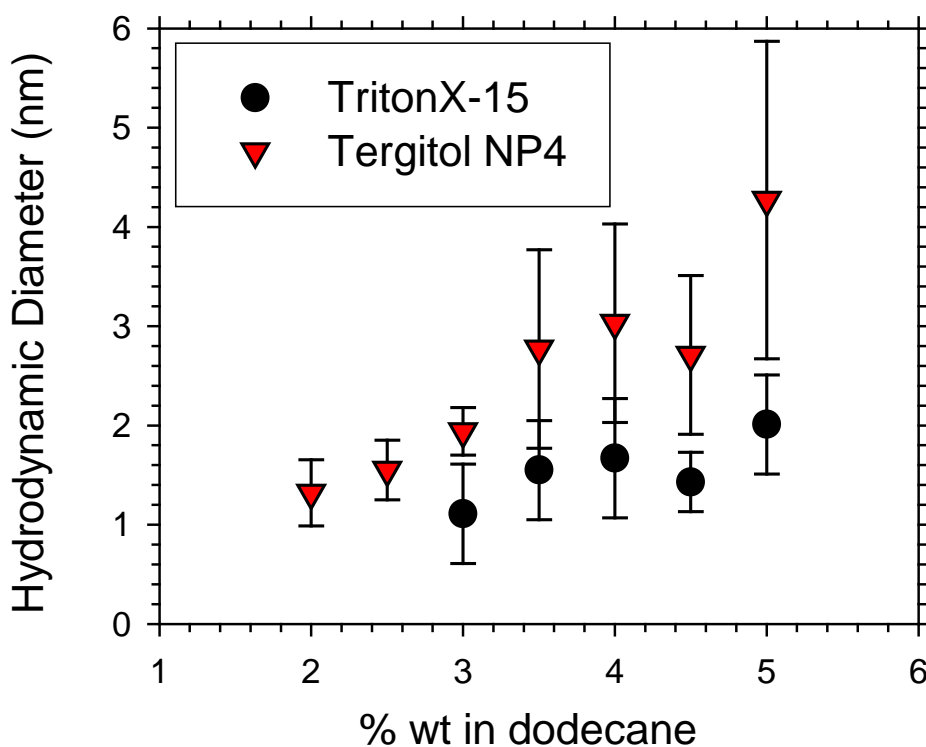


Figure 4.9. Average hydrodynamic diameters of micelles found from phase analysis light scattering versus concentration of surfactant in dodecane.

4.5 Conclusions

The conductivity and charge concentration of AOT[®], OLOA 11000[®], Span 85[®], Span 80[®], and Span 20[®] micelle solutions in dodecane were found with impedance spectroscopy across a range of concentrations. The hydrodynamic diameter of the micelles was determined from phase analysis light scattering. The surfactants that formed the larger micelles in dodecane exhibited the highest electrical conductivity. The diameter of the polar core of the micelles was estimated using the tail lengths of the surfactants. The molar conductance of each surfactant increased exponentially with the estimated diameter of the polar core of

the micelles. The charge fluctuation model accurately predicted the observed result that micelle size is the most important factor in increasing the conductivity of nonpolar liquids.

The charge concentration per surfactant molecule of each surfactant was also determined with impedance spectroscopy. Similarly, the surfactants forming the larger micelles exhibited larger charge concentration. Good exponential agreement between the charge concentration per surfactant and the diameter of the polar core of the micelle, however, was not observed in the data. A quantifiable exponential fit was not obtained due a few possible factors including improper estimations of the micelle aggregation number, tail length, and improper measurements of the charge concentration due to a non-zero zeta potential on the ITO electrodes.

The conductivity of Tergitol[®] NP-4 and Triton[®] X-15 in dodecane was not proportional with the surfactant concentration. Measurements of the micelle size with phase analysis scattering revealed the micelle size to be concentration dependent for these surfactants. The charge fluctuation model can qualitatively predict the non-linear relationship between conductivity and surfactant concentration because of the increasing micelle size that should increase the ratio of micelles that obtain charge exponentially. More information on the size and structure of the micelles is needed before the model can be quantitatively fit these

results. Overall, this study has suggested the generality of the charge fluctuation model when applied to a variety of surfactants and micelles in dodecane.

4.6 Acknowledgement

We thank Yuan Fang for performing measurements with the conductivity meter and phase analysis light scattering for the solutions of Tergitol NP-4[®], Triton X-15[®], Tergitol TMN-3[®], and Tergitol 15-S-3[®]. We also gratefully acknowledge financial support for this project from the Dow Chemical Company.

4.7 References

1. *Interfacial Phenomena in Apolar Media*. Surfactant Science Series, ed. M.J. Schick and F.M. Fowkes. 1987, New York, NY: Marcel Dekker.
2. Eicke, H.F., *Surfactants in nonpolar solvents: Aggregation and Micellization*. Topics in Current Chemistry, 1980. **87**: p. 85-145.
3. Eicke, H.F. and H. Christen, *Is Water Critical to the Formation of Micelles in Apolar Media?* Helvetica Chimica Acta, 1978. **61**(6): p. 2258-2263.
4. Smith, G.N., et al., Evidence for a critical micelle concentration of surfactants in hydrocarbon solvents. Langmuir, 2013. **29**(10): p. 3252-8.
5. Smith, G.N. and J. Eastoe, *Controlling colloid charge in nonpolar liquids with surfactants*. Phys Chem Chem Phys, 2013. **15**(2): p. 424-39.
6. Morrison, I.D., *Electrical charges in nonaqueous media*. Colloids and Surfaces A: Physicochemical and Engineering Aspects, 1993. **71**: p. 1-37.
7. Hall, D.G., Conductivity of Microemulsions: An Improved Charge Fluctuation Model. Journal of Physical Chemistry, 1990. **94**: p. 429-430.
8. <Morrison nonpolar media 2005.pdf>.

9. Bombard, A.J. and A. Dukhin, *Ionization of a Nonpolar Liquid with an Alcohol*. Langmuir, 2014.
10. Dukhin, A. and S. Parlia, *Ions, ion pairs and inverse micelles in non-polar media*. Current Opinion in Colloid & Interface Science, 2013. **18**(2): p. 93-115.
11. Dukhin, A.S., Properties of electrolytic solutions: Dissociation, fluctuation and disproportionation models for ionization of surfactant solutions in low- and non-polar liquids. JCIS manuscript, 2012.
12. Guo, Q., Surfactants in Nonpolar Oils: Agents of Electric Charging and Nanogel Templates. PhD Thesis, 2012.
13. Guo, Q., V. Singh, and S.H. Behrens, *Electric charging in nonpolar liquids because of nonionizable surfactants*. Langmuir, 2010. **26**(5): p. 3203-7.
14. Michor, E.L. and J.C. Berg, Extension to the Charge Fluctuation Model for the Prediction of the Conductivity of Apolar Reverse Micellar Systems. Langmuir, 2012. **28**: p. 15751-15755.
15. Eicke, H.F., M. Borkovec, and B. Das-Gupta, *Conductivity of Water-in - Oil Microemulsions: A Quantitative Charge Fluctuation Model*. Journal of Physical Chemistry, 1989. **93**: p. 314-317.
16. Kallay, N. and A. Chittofrati, *Conductivity of Microemulsions: Refinement of Charge Fluctuation Model*. Journal of Physical Chemistry, 1990. **94**: p. 4755-4756.
17. Gacek, M., et al., Effects of trace water on charging of silica particles dispersed in a nonpolar medium. Langmuir, 2012. **28**(31): p. 11633-8.
18. Yezer, B.A., et al., Use of electrochemical impedance spectroscopy to determine double-layer capacitance in doped nonpolar liquids. Journal of Colloid and Interface Science, 2015. **449**: p. 2-12.
19. Yezer, B.A., et al., Determination of charge carrier concentration in doped nonpolar liquids by impedance spectroscopy in the presence of charge adsorption. Journal of Colloid and Interface Science, 2016. **469**: p. 325-337.
20. Abou-Nemeh, I. and H.J. Bart, *Microstructures in the System Water/D2EHPA/Span-80/n-Dodecane*. Langmuir, 1998. **14**: p. 4451-4459.

21. Mukherjee, K. and S.P. Moulik, Thermodynamics of Micellization of Aerosol OT in Polar and Nonpolar Solvents. A Calorimetric Study. *Langmuir*, 1993. **9**: p. 1727-1730.
22. Hsu, M.F., E.R. Dufresne, and D.A. Weitz, *Charge Stabilization in Nonpolar Solvents*. *Langmuir*, 2005. **21**: p. 4881-4887.
23. Berg, J.C., *An Introduction to Interfaces and Colloids: The Bridge to Nanoscience*. 2010, Singapore: World Scientific Publishing.

Chapter 5 Determination of the zeta potential of planar solids in nonpolar liquids

5.1 Introduction

The zeta potential is a common metric of the electrostatic state at a solid/liquid interface. Determining the zeta potential of a solid in contact with aqueous solutions is a routine procedure for particles and planar samples.[1, 2] Electrophoresis and light scattering are the basis of popular commercial instrumentation for particles. One measures the electrophoretic mobility and uses theory to calculate the zeta potential.[2] Complications arise when the Debye length (κ^{-1}) is comparable to the particle size (*radius a*), but corrections are available.[3] For macroscopic surfaces like planar samples, one measures streaming potential or streaming current generated by flow over the sample and uses appropriate theory to convert it to zeta potential. Flow through a slit is a classic method for planar samples.[1, 2] Surface conductivity can complicate the interpretation of streaming potential when using the slit design, but methods for correcting the simplest models are well known. [1-3] Flow in the vicinity of a rotating disk also generates streaming potential that can be used to determine the zeta potential of planar samples.[4-6] The rotating disk does not suffer from surface conductivity because the appropriate length scale in the Dukhin number is

the radius of the disk, making the contribution of surface conduction negligible.[6, 7]

5.1.1 Charge on solids in nonpolar media

Researchers also use electrokinetic phenomena to probe the electrostatic state near particulate solids in nonpolar media.[8-21] Commercial surfactants such as OLOA 11000[®], AOT[®], Span 85[®], Span 80[®], and Span 20[®] impart measurable electrophoretic mobility to particles. Nonpolar host liquids, however, present special problems. The relatively large screening lengths associated with small charge concentrations mean that κa typically is not large. Corrections as mentioned above can be applied in order to determine the zeta potential if the Debye length is known, but κ^{-1} typically is not known. Furthermore, the very magnitude of the electrophoretic mobility is small because it is proportional to the permittivity of the liquid, as in Smoluchowski's equation and related formulas, and the permittivity of nonpolar liquids is small. For equal zeta potential and viscosities, the magnitude of the electrophoretic mobility of a particle in a nonpolar liquid ($\epsilon/\epsilon_0 = 2$) would be 40 times smaller than in water. Special cells and settings are required for most commercial instruments to measure the lower values of electrophoretic mobility of particles in nonpolar liquids. The values test the detection limitations of the instrument; for example, one might even need to be concerned about detecting electrophoresis in a non-negligible background of Brownian motion. In addition to the smaller response, the measured mobilities of

particles in nonpolar liquids also depend on the applied electric field.[11, 13, 18] The electrophoretic mobility must be extrapolated to zero field, introducing even more uncertainty in the zeta potential of the particles.

The electrostatic state near macroscopic surfaces in nonpolar media also can also be characterized by a zeta potential, but the measurement is not much investigated other than for glass capillaries where complications with capillary length dependence arise.[21] The determination of zeta potentials of macroscopic surfaces could be useful, for example, when particles of the same material cannot be suspended or when judging the attraction or repulsion between a colloid and a solid surface such as a filter. We had a particular interest in determining the zeta potential of glass slides coated with indium tin oxide, the material we used as electrodes in electrochemical impedance spectroscopy experiments to determine the Debye length in surfactant-doped dodecane. The impedance spectra yielded the capacitance of the double layer on the electrode. We converted the capacitance to Debye length by taking the quotient of the permittivity and the capacitance per unit area. Underlying this calculation is an assumption that the native zeta potential of ITO in the test solutions was smaller than the thermal voltage. Thus, we needed to determine the zeta potential of ITO electrodes to test this assumption.

5.1.2 The rotating disk

We chose the rotating disk as the basis for determining the zeta potential of solid samples because surface conductivity does not diminish the streaming potential. A schematic of the rotating disk arrangement appears in Figure 5.1. A motor (not shown) rotates a disk-shaped sample on its axis in a liquid. The rotation generates a streaming potential in the vicinity of the disk. Two sensors, one near the sample on the axis and the other far from the sample, detect the streaming potential. The sensors in aqueous solutions are Ag/AgCl electrodes, known to be reversible and stable. The most basic formula for converting the streaming potential ϕ_s to zeta potential ζ is [4]

$$\zeta = \frac{\phi_s K_L}{a \varepsilon} \sqrt{\frac{\nu}{\Omega^3}} \left[\frac{1.960 \sqrt{1 + \bar{z}^2}}{1 - 2\bar{z} \sqrt{1 + \bar{z}^2} + 2\bar{z}^2} \right] \quad (5.1)$$

where ε is the permittivity, a is the sample radius, Ω is the rotation rate, ν is the kinematic viscosity, and K_L is the ionic conductivity of the liquid. The variable z is the distance between the sensor at the axis and the plane of the sample's surface; the overbar on z indicates normalization by the sample's radius.

The software developed for the experiment modulates the rotation rate of the disk between zero and a specified value according to a square wave at 0.2 Hz. A voltmeter records a corresponding square wave signal at the same frequency. The amplitude of the streaming potential varies from zero to several mV depending on the conductivity, permittivity, rotation rate, and zeta potential of the sample. One

observes repeating sharp transitions of measured voltage in solution when the motor cycles on or off as in Figure 5.2 for freshly cleaved mica rotating at 4000 rpm in dilute KCl. In Figure 5.2 the jump was approximately $300\ \mu\text{V}$. We equate the voltage change at the abrupt jump of the signal with the streaming potential. The software identifies the latest credible voltage before a transition and the first credible voltage after a transition, calculates the difference, and reports this difference as the streaming potential. The difference typically is taken between readings separated in time by approximately 40 ms.

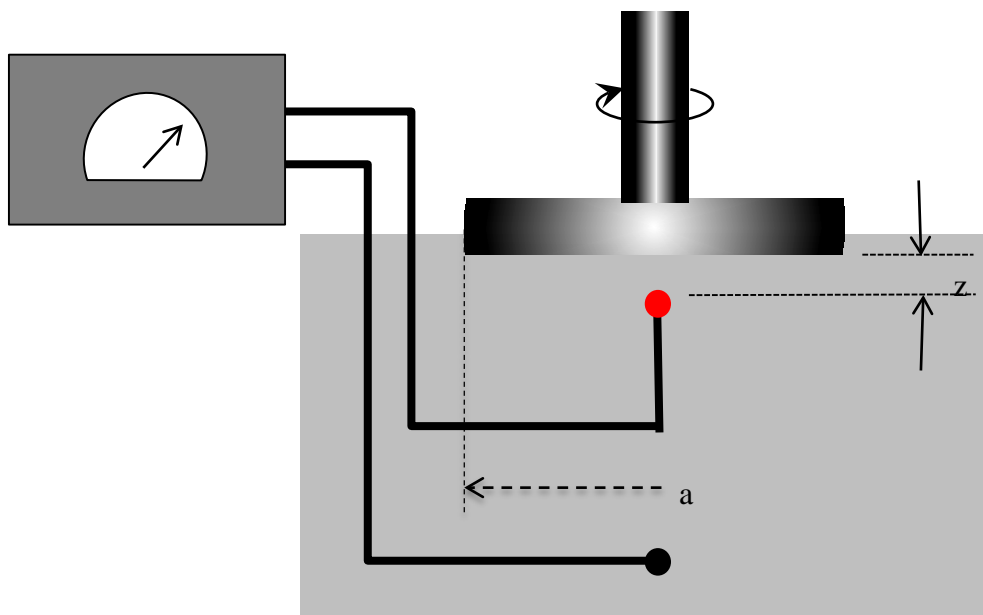


Figure 5.1. The rotating disk approach to streaming potential measurement. One sensing electrode is at the axis near the rotating sample and the other sensing electrode is far from the sample. The voltmeter reports the potential difference between the two electrodes.

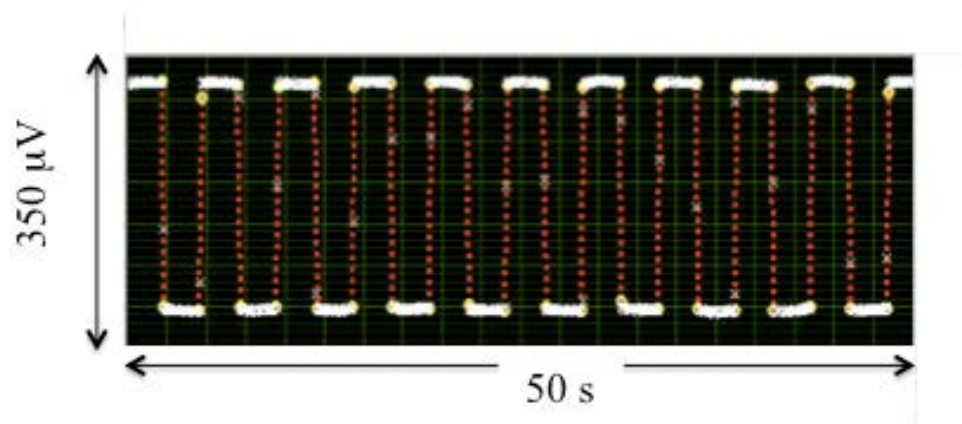


Figure 5.2. Streaming potential near a mica surface in dilute KCl solution with the standard procedure used for aqueous solutions with Ag/AgCl sensors. The dotted lines correspond to the times at which the rotation transitioned from off to on and vice versa. The white symbols are data points spaced by 20 ms. Note the square wave voltage measurement in response to the mechanical rotation. The measured potential tracked to streaming potential closely.

5.1.3 Application to nonpolar liquids

Here, we present the results of experiments in which the apparatus and method were adapted to determine the zeta potential of solids in nonpolar liquids. We measured the potential that arose when various planar solids were rotated in the vicinity of two glassy carbon sensors that replaced the Ag/AgCl electrodes shown in Figure 5.1 and an electrometer replaced the nanovoltmeter. The aims of the investigation were to determine whether a signal generated by rotating a disk-shaped sample and measured in this fashion could be streaming potential and, if so, to produce evidence that (5.1) can be applied to determine the zeta potential of the sample. The shape of the signal obtained was unlike the signal obtained in polar solvents, but we identified a method of obtaining the streaming potential from it; the voltages derived therefrom produced plausible zeta potentials when

(5.1) was used to reduce the data. The shape of the signal was rationalized as described herein.

5.2 Experiments

5.2.1 Apparatus

A precision motor/controller (Pine Instruments AFMSRCE) rotated a 25 mm diameter x 50 mm long cylindrical sample support made of polycarbonate. The vessel was a 500 mL polycarbonate container filled to a level just above the plane of the sample when it was in position for experimentation. The sensors were short rods of glassy carbon (SPI Supplies) affixed to silver wires with conductive silver epoxy and sheathed in fluorinated heat shrink tubing. For the axial sensor (Figure 5.1), the rods used in the fabrication were 3 mm in diameter and the sheath covered the entire rod other than the circular end face exposed to the solution. The sensor placed far from the sample was likewise constructed from a glassy carbon rod, silver epoxy, and silver wire, but the heat shrink tubing exposed approximately 35 mm of bare rod as well as the tip face. The distance between the plane of the sample and the electrode at the axis was 1 mm. Either a Keithley Instruments 2182A Nanovoltmeter or a Keithley Instruments 6514 Electrometer detected the voltage that arose between the sensors. The positive terminal of the voltmeter or electrometer was attached to the sensor at the axis and the negative terminal was attached to the sensor far from the sample. The grounding terminal of the voltmeter was attached to a metal stage supporting the cell.

5.2.2 Materials

The test liquids were DI water and solutions of OLOA 11000[®] (polyisobutylene succinimide, Chevron Oronite), AOT[®] (Sigma-Aldrich), and Span 20[®] (Sigma-Aldrich) in dodecane. Experiments based on electrochemical impedance spectroscopy[22] and tests with the aid of a conductivity meter designed for nonaqueous liquids (Dispersion Technologies DT-700) provided the conductivities and dielectric constants of these liquids. The cell was open to the atmosphere. The samples were disks of muscovite mica (SPI Supplies cat. # 01926-MB), borosilicate cover glasses (Electron Microscopy Sciences, cat. #72225-01), ITO coated glass (Bioprotechs, Butler, PA) or fused silica disks having diameters of 25 mm, *i.e.* commensurate with the sample support.

5.2.3 Method

For the preliminary experiments in de-ionized water, the samples were attached to the support with double-sided tape, but a different method was required in dodecane. A solution of sugar dissolved to saturation in water was heated until a thick syrup was formed; the syrup was used as glue to attach the samples to the circular end face of the polycarbonate supports, which held the samples satisfactorily for the duration of the experiments. The cylindrical support, with sample attached, was screwed onto the end of the spindle driven by the motor. The software (LabVIEW, National Instruments) started and stopped the rotation with a rotator rise time of a few milliseconds. The rotation was imposed for times varying from seconds to minutes. During each experiment the voltmeter

and electrometer stored up to 1024 and 2500 measurements, respectively, that were subsequently downloaded them to a computer via a GPIB connection.

5.2.4. Electrophoretic mobility measurements

250 nm Silica particles (Fiber Optics Center Inc., New Bedford, MA) were dried in a vacuum oven at 170 °C for 2 hours. The particles were then added to each solution at 500 ppm by weight. The suspensions were sonicated for 1 hour and allowed to equilibrate overnight in a desiccator before measurements were made. The electrophoretic mobility of the suspensions was measured by Phase Analysis Light Scattering (PALS) using a Malvern ZetaSizer Nano. The suspensions were measured in a quartz cuvette with a “dip-cell” designed for non-aqueous solvents (Malvern). The palladium electrodes of the dip-cell are spaced 0.5 cm apart. The electrophoretic mobility of each sample was determined at applied voltages varying from 10 to 40 V. Each measurement was averaged over ten “runs” and ten measurements were made at each applied voltage. To eliminate any effects of field-induced charging, the electrophoretic mobility of each concentration was extrapolated back to zero field strength to determine the mobility of the particles.

5.3 Results

5.3.1 Glassy carbon sensors

In initial experiments to test the response of the glassy carbon sensors with resistive liquids, we rotated disks of freshly cleaved muscovite mica in

experiments with de-ionized water and in other experiments with dodecane doped with 0.5 wt.% AOT[®]. The experiment in de-ionized water (Figure 5.3) followed the pattern of Figure 5.2, where the recorded potential changed abruptly when the rotation rate began or ended. The measured potential decreased, which means that the sign of the charge on mica was negative in the water, as expected. The conductivity of the water was measurable, which allowed the determination of the zeta potential of -150 mV, as expected for this highly charged mineral in water at extreme dilution. The response in dodecane, Figure 5.4A, was quite different. The potential drifted monotonically. Subtle kinks were observed at the beginning and end of rotation, but the relationship between the potential signal in Figure 5.4a and the streaming potential was not clear.

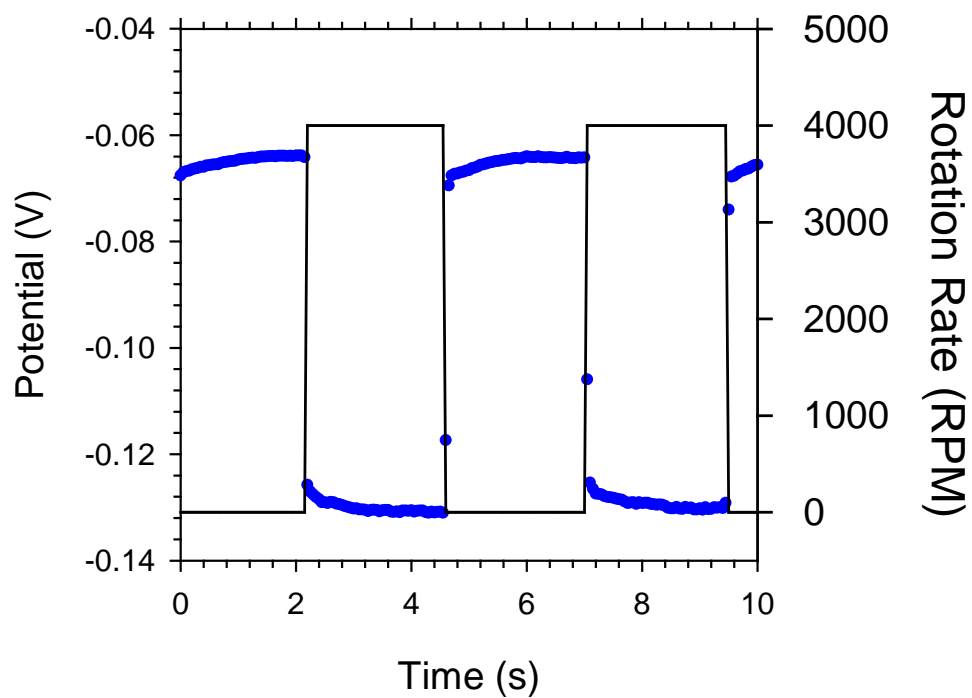


Figure 5.3. Streaming potential (blue circles) measurement of mica in deionized water with a 4000 RPM square wave rotation rate (black curve) applied with the standard procedure used for aqueous solutions adjusting glassy carbon electrodes for the Ag/AgCl sensors.

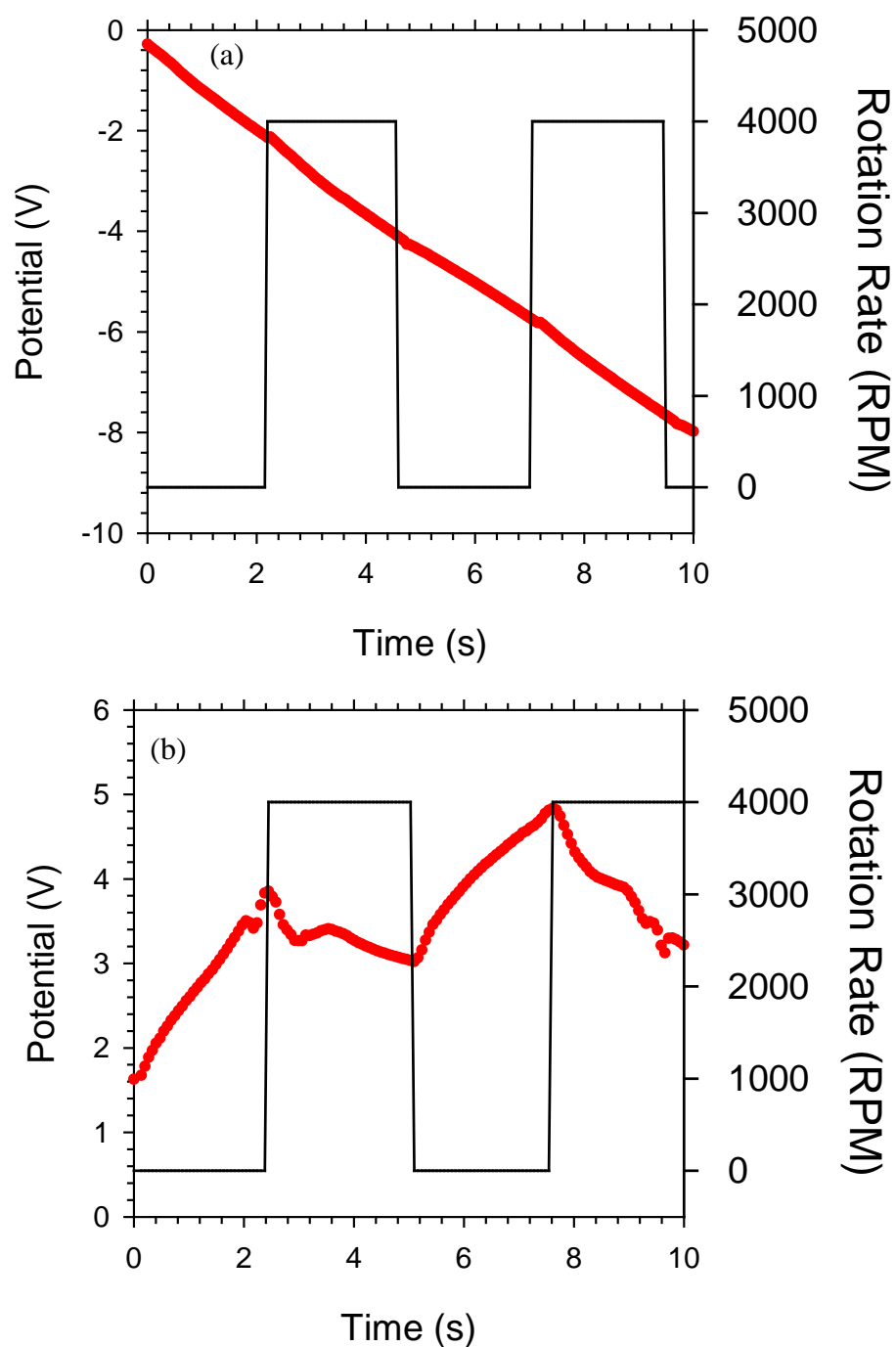


Figure 5.4. A) Mica in 0.5% wt. AOT[®] in dodecane measured with glassy carbon electrodes connected to a nanovoltmeter. B) Mica in 0.5% wt. AOT[®] in dodecane measured with glassy carbon electrodes connected to an electrometer.

5.3.2 Substitution of an electrometer for the nanovoltmeter

Hypothesizing that the drift indicated the need for detection of electric potential with a higher input impedance, we substituted the electrometer for the nanovoltmeter. The input resistance of the electrometer was 5 orders of magnitude greater than the input resistance of the nanovoltmeter. The same 4000 rpm (amplitude) square wave at 0.2 Hz was applied to the mica surface in 0.5% AOT-dodecane with glassy carbon sensors. The change of detection instrument resulted in the “saw-tooth” signal observed in Figure 5.4b. Use of the electrometer eliminated the negative drift in the potential observed in Figure 5.4a. The signal in Figure 5.4b, however, was unlike the instantaneous “jumps” observed in Figure 5.2 and Figure 5.3. The relationship between this signal and streaming potential of the mica surface was still unclear, but we hypothesized that the pattern might be attributed to a slow response of the instrument in such highly insulating liquids.

We extended the period of rotation to 600 seconds to reveal more of the rise of the voltage. The result of rotating the mica as in Figure 5.4a and Figure 5.4b, but for a period of 1200 s, appears in Figure 5.5. When rotation began, the potential of the axial electrode (ordinate) increased with respect to the potential of the reference electrode and asymptotically approached a “steady-state” plateau value as a function of time. Most of the increase occurred within the first 100 seconds. When the rotation stopped, the potential difference decreased at the same rate it had increased and asymptotically approached its value before the initial rotation. The value of the potential difference at the plateau during rotation was

42 V relative to the reference electrode. The abrupt transitions of Figure 5.2 and Figure 5.3 were not observed, but the pattern of Figure 5.5 was highly reproducible. Taking that the plateau value of Figure 5.5 just before the transition from “on” to “off” as the streaming potential relative to the value just prior to the previous “on”, we used the formula of equation (5.1) and calculated a zeta potential of the mica surface in 0.5% wt. AOT[®] equal to +100 mV .

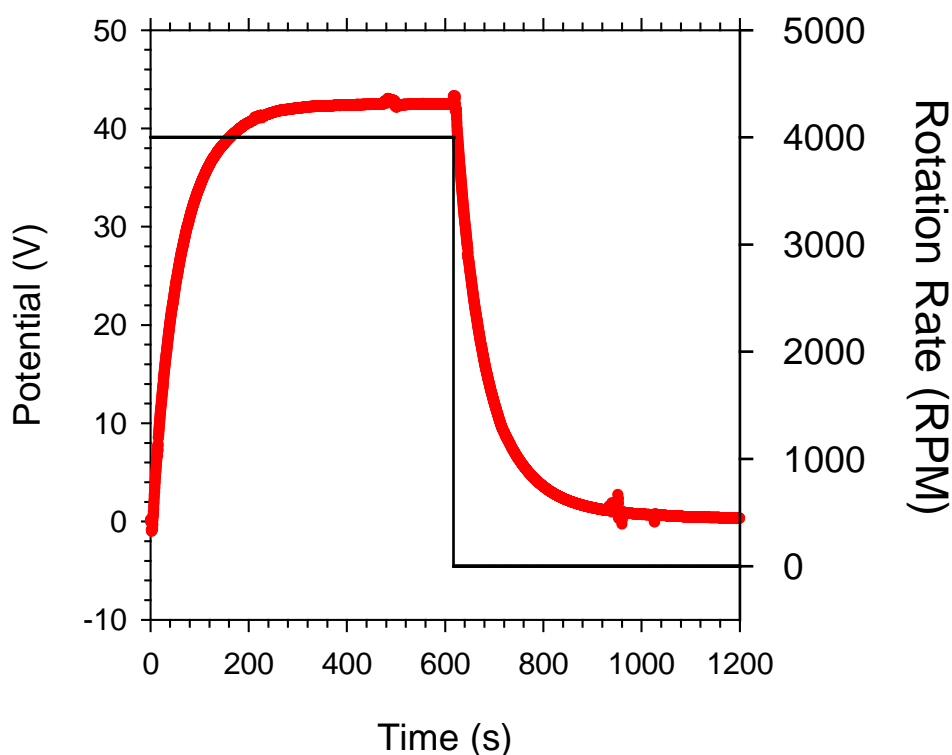


Figure 5.5. Mica in 0.5% wt. AOT[®] in dodecane measured with glassy carbon electrodes, an electrometer, and a long 10 minute rotation time plotted on the right axis.

The next experiments were designed to probe whether the difference between the measured “steady-state” potentials was indeed the streaming potential.

Equation (5.1) predicts that the streaming potential depends on the rate of rotation to the 3/2 power, the sign of charge on the sample, the positioning of the

electrodes, and the presence or absence of species in the liquid having charge opposite in sign to the charge on the sample. Three experiments as described below were designed to build confidence that streaming potential was being measured.

5.3.3 Effect of rotation rate

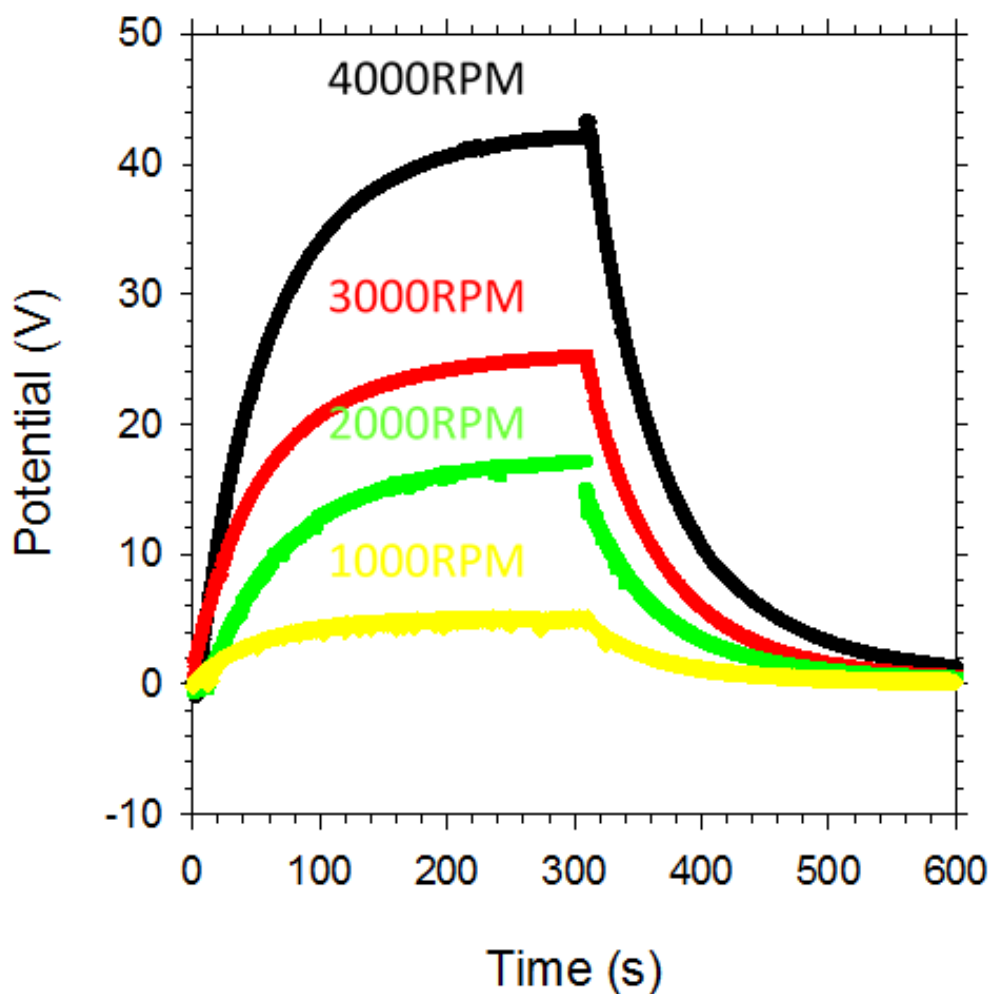


Figure 5.6. Mica in 0.5% wt. AOT® in dodecane at 4000 RPM (black), 3000 RPM (red), 2000 RPM (green), and 1000 RPM (yellow).

Varying the rotation rate produced the data of Figure 5.6 in the same 0.5% wt. AOT/dodecane solution as Figure 5.5. The rapid rise/fall followed by an

asymptotic approach to a steady value was obtained in all cases. The plateau value increased as the rotation rate increased as expected from (5.1).

5.3.4 Effect of sensor location

Figure 5.7A shows the resulting potential and current lines near a rotating disk previously calculated for this geometry.[4] The sign of the potential at the disk axis has the same sign as the zeta potential of the disk, but the sign of the potential reverses near the edge of the disk. Figure 5.7B shows data obtained when the on/off pattern was performed with the sensor at the axis and then was moved to the periphery. When at the axis, the electrode reported an increasing voltage after the start of rotation. When near the periphery, the same electrode in the same solution reported a decrease of voltage upon rotation. In both cases, the measurements were made with respect to the other sensor placed far from the sample.

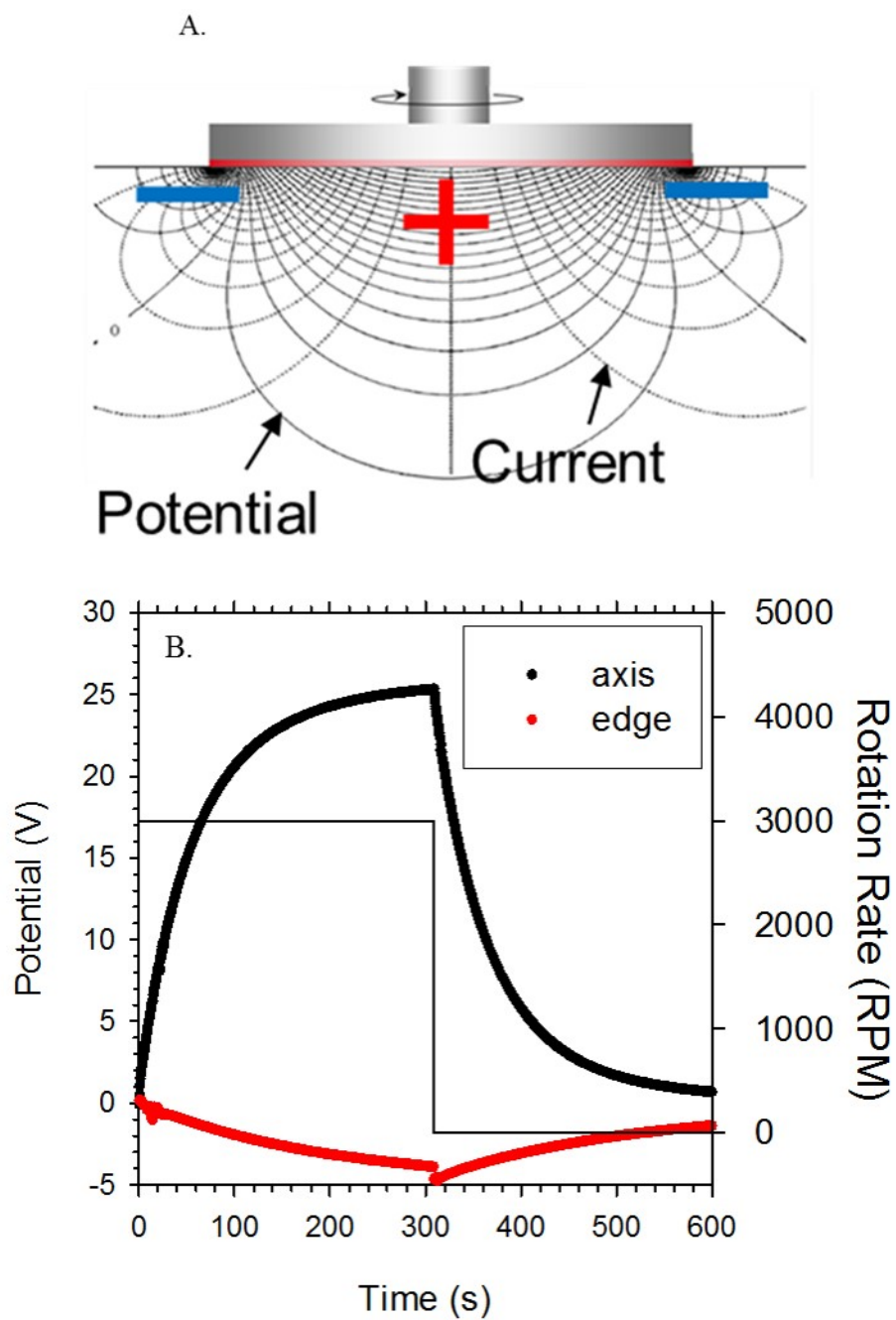


Figure 5.7. A) Schematic of potential and current lines near a positive rotating disk as calculated in[6]. B) Data using the method for nonpolar liquids with sensor at axis and disk edge with 0.5% AOT[®] dodecane.

5.3.5 Adsorption of oppositely charged particles

The third test involved measuring the streaming potential of mica in the absence or presence of carbon black particles (Cabot, Monarch 280) in a solution of 1.5% wt. AOT[®] in dodecane. Figure 5.8 shows that the rotation caused the potential of the electrode to rise in the absence of carbon black particles (blue curve) while the potential decreased to a negative “steady state” potential when the particles were dispersed into the solution (red curve). The rise of potential in the absence of particles is consistent with the same positive rise observed for mica in AOT-dodecane in Figure 5.5 and Figure 5.6. In the presence of carbon black particles, however, the rotation caused the potential of the electrode at the axis to fall. The sign of the potential therefore was opposite in the two cases, but the rate at which the measured potential approached its asymptotic value was not affected.

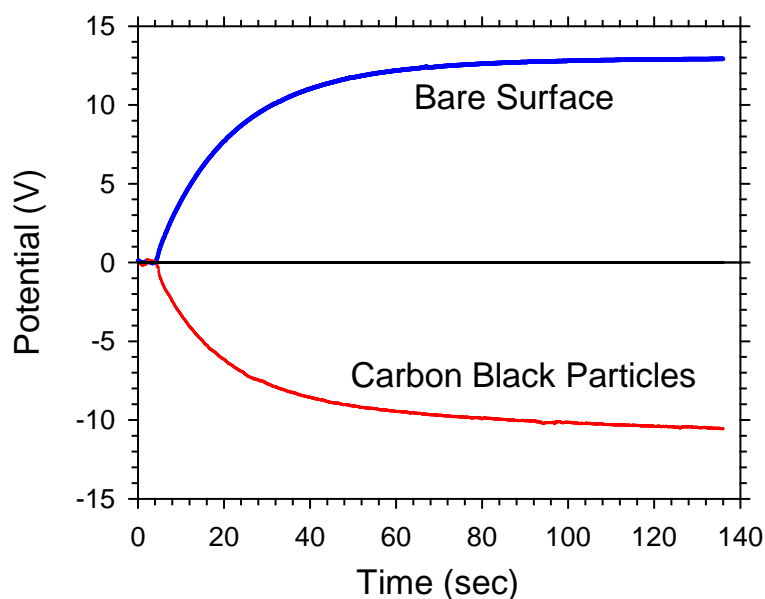


Figure 5.8. Mica in 1.5% AOT[®] dodecane, 4000 RPM with a positively charged bare surface (blue curve) and with negatively charged carbon black particles added to the solution (red curve).

5.4 Discussion

As mentioned in the previous section, we hypothesized that the voltage difference between the last measurement *before* an on/off transition and the asymptote *after* the same transition was the correct measurement of the magnitude of the streaming potential for use in (5.1). The direction of change of the measured potential when rotation begins indicated the appropriate sign of the streaming potential for use in that equation. With respect to Figure 5.5, a positive streaming potential, as measured when the positive terminal of the electrometer is connected to the axial sensor, indicated a positive zeta potential, and *vice versa*. In the three part discussion that follows we first argue that the results in Figure 5.5– Figure 5.8 support the hypothesis that streaming potential is being measured. The second part rationalizes the asymptotic approach of the measured potential to full value. Finally, zeta potentials of the sample materials in surfactant-doped dodecane are reported.

5.4.1 The streaming potential

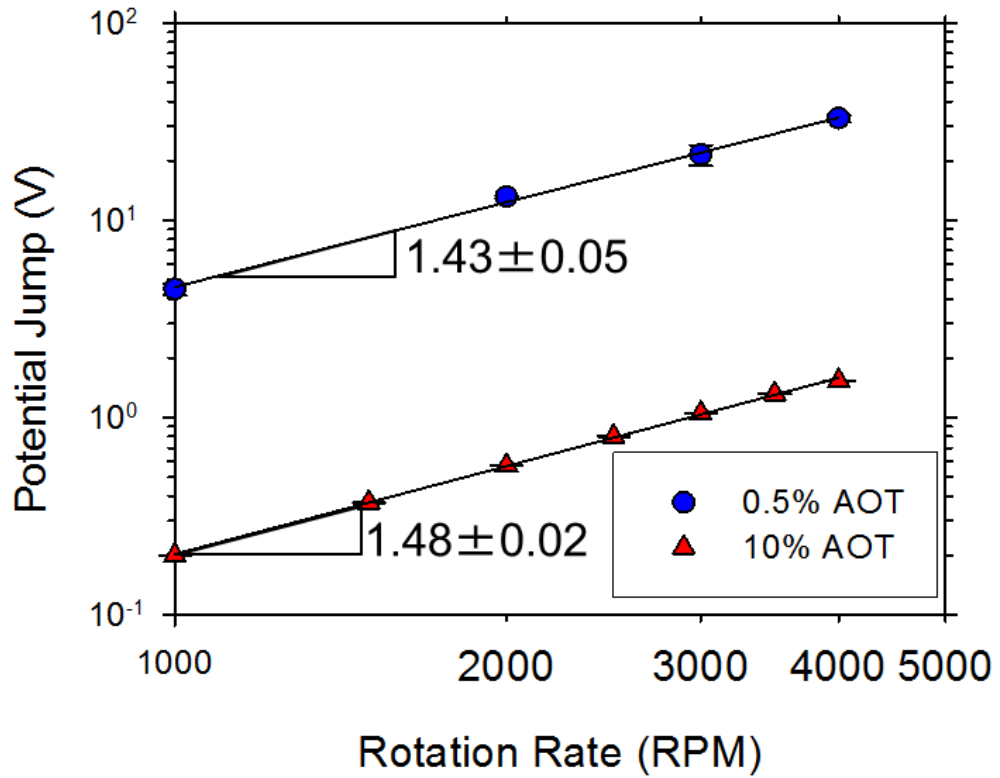


Figure 5.9. Rotation rate dependence of mica in 0.5 wt.% and 10 wt.% AOT[®].

Equation (5.1) predicts that the magnitude of the streaming potential increases with the $3/2$ power of the rotation rate. Experiments in aqueous solutions have verified this characteristic dependence.[6] The asymptotic plateau values of Figure 5.6 were re-plotted in Figure 5.9 against the rotation rate, on logarithmic scales for two different solutions of surfactants in dodecane, with mica as the sample. Linear regression of the log of the potential versus the log of the rotation rate had a slope of 1.43 ± 0.05 for the solution of 0.5% wt. AOT[®] in dodecane and a slope of 1.48 ± 0.02 for the solution of 10% wt. AOT[®] in dodecane. In both cases the streaming potential depended on the rotation rate near

to the $3/2$ power. This agreement with the theory of equation (5.1) was strong evidence that streaming potential was being measured.

The theory of the streaming potential near a rotating disk also predicts that the periphery of the sample is one pole of the streaming potential and the center of the sample is the opposite pole (see Figure 5.7A).[4] Ohmic solution resistance separates the two poles. A sensing electrode positioned at the axis near the sample should detect a potential of one polarity and the same sensor should report a potential of the opposite polarity when positioned outside the radius of the sample and near its plane. Figure 5.7B demonstrates that the measurements fulfilled this requirement. When the electrode was placed at the axis and near the sample, rotation biased the sensor negatively, which indicated a negative zeta potential. The same sensor, when subsequently moved to the periphery in the same solution with the same sample, was biased toward a positive potential. This second major piece of evidence indicated that streaming potential was being detected.

The third test of the hypothesis was an experiment in which a sample exhibiting a positive-going signal at the onset of rotation was exposed to a dispersion containing particles independently determined to be negative. The experiments of Figure 5.5 and Figure 5.6 showed that rotation of mica in dodecane doped with surfactant biased the measured potential positively when the rotation was started. Carbon black particles are known to have negative mobility

in AOT–doped dodecane;[19] therefore, carbon black particles dispersed in a solution of AOT[®] in dodecane should electrostatically adsorb onto the mica and reverse its sign. This logic underlies the experiment and results appearing in Figure 5.8, where carbon black particles, pipetted into a solution of AOT[®] in dodecane, reversed the direction of the change of measured potential at the onset of rotation.

The results and discussion above establish that streaming potential is being measured, but the shape of the signal in Figure 5.5 was quite different from the shape of the signal in Figure 5.2. The final step in building the case that we were measuring the full value of the streaming potential is to rationalize the different shapes.

5.4.2 The shape of the signal

The signals obtained with aqueous solutions (Figure 5.2 and Figure 5.3) were similar even though the sensors used in Figure 5.2 were reversible Ag/AgCl electrodes and the sensors used in Figure 5.3 were glassy carbon electrodes known to be electrochemically irreversible in the absence of a reacting species. The signal from the glassy carbon electrodes in a nonpolar liquid as measured by the 2182A Nanovoltmeter (Figure 5.4A) was quite different from the signal for de-ionized water in Figure 5.3. The measured potential responded reproducibly in Figure 5.5 when an electrometer was used in place of the nanovoltmeter with sufficiently long periods of “on” and “off”. The three cases described above were

strong evidence that streaming potential was being measured, but the results begged two fundamental questions:

1. How can irreversible electrodes be used to measure the streaming potential?
2. Why did the on/off cycle in aqueous 1 mM KCl solutions exhibit a square wave response, but the on/off waveform in nonpolar solutions exhibit an asymptotic approach to a maximum value?

These questions can be addressed with analysis of an equivalent circuit (Figure 5.10) that reflects the principal components contributing to the observed signal $V(t)$ in response to streaming potential $\phi_s(t)$ that is essentially a square wave with rise time on the order of milliseconds corresponding to the rise time of the motor and boundary layer on the disk. The circuit of Figure 5.10 assumes that the geometric capacitance of the sensor is infinitesimally small and the input resistance of the voltage measuring device is infinite, both of which are true for proper measurements. Inspection of this circuit reveals two crucial facts: First, whatever the values of the resistance to flow of current to the sensor, R_Ω , the electrochemical capacitance and resistance of the sensor's interface C_{SE} and R_{SE} respectively, and the voltmeter's capacitance C_M , the observed voltage $V(t)$ becomes equal to the streaming potential $\phi_s(t)$ as the frequency of the on/off cycle

decreases. Second, one or more of the RC time constants associated with the circuit of Figure 5.10 govern the transition by exponential functions of time.

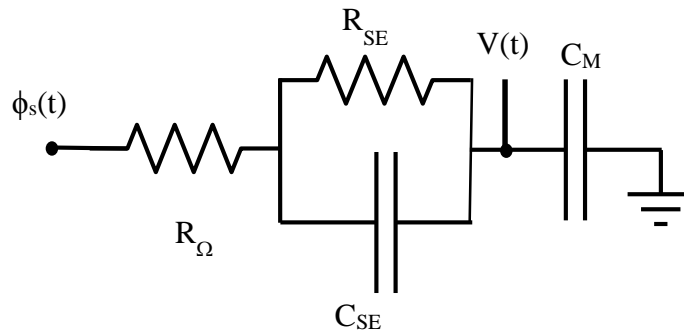


Figure 5.10. A schematic of the equivalent electrokinetic and measurement circuits. The input impedance R_M must be much greater than the sum of R_{SE} , R_s and R_{EK} to guarantee that a steady measured potential f_1 is the streaming potential when the disk is rotating. There are two important time constants: $R_s C_m$ (short time) and $R_{SE} C_{SE}$ (long time). f_1 rises quickly, on the order of ms. Sensing current then flows through R_s and C_{SE} , limited by time constant $R_s C_m$ when C_{SE} is large. The large capacitance C_{SE} short circuits R_{SE} during this period.

The circuit of Figure 5.10 and the facts cited in the previous paragraph provide answers to the two questions posed. Irreversible electrodes (as opposed to ideally polarizable) can be used to determine the streaming potential if the period between on/off transitions is sufficiently long and if the component values of the circuit in Figure 5.10 are both finite and constant. The measured voltage $V(t)$ becomes equal to the streaming potential quickly for small resistances such as found in aqueous systems with reversible couples like Ag/AgCl where the time constants are all less than 10 milliseconds. Thus the transition time in Figure 5.2 is much faster than the data acquisition time, which means that $V(t) = \phi(t)$ at all times. In nonpolar systems, however, the resistances are large, making the RC

time constants much longer than the 20 ms between the sequential voltage measurements; this difference explains why the transitions in Figure 5.5 appear to be exponential decays with respect to their asymptotic values.

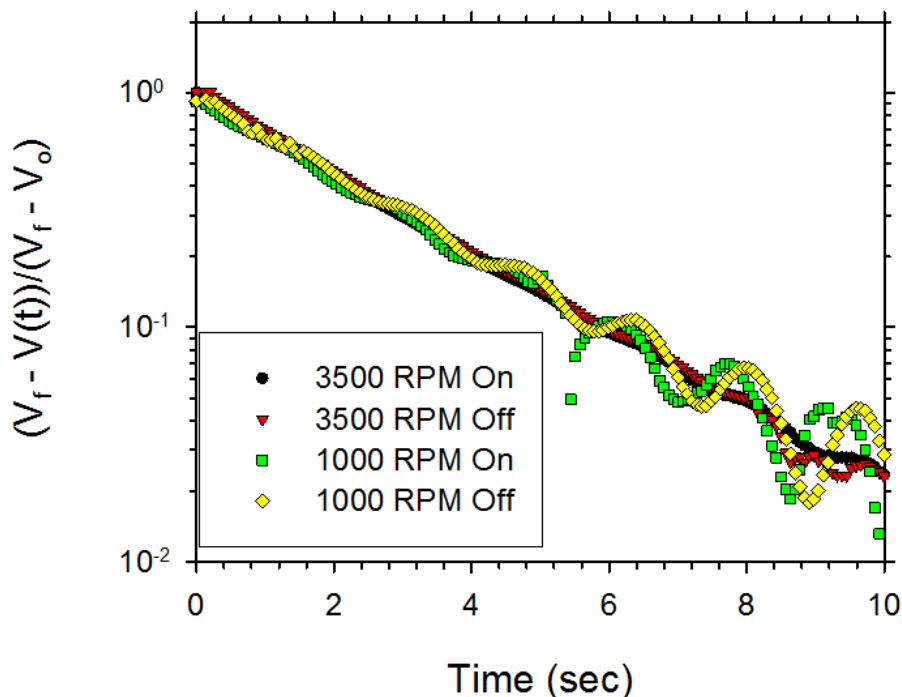


Figure 5.11. The fraction of change remaining in the potential versus time is shown on a semilog-y plot for mica surface in 1.5% wt AOT[®] in dodecane. The rate of change in the potential is independent of the rotation being turned on or off and independent of the rotation rate.

We applied this logic to the decay-like dependences found from experiments related to Figure 5.5 and Figure 5.6. Figure 5.11 shows semi-log decay plots from rotating mica in 1.5% wt. AOT[®] in dodecane. In each case the logarithm of the unaccomplished change of potential was linear as a function of time and had a negative slope. The fractional (normalized) decay was independent of the rotation rate, as expected. Furthermore, the reciprocal of the decay constants should be proportional either to the conductivity or its square root because both $R\Omega$ and R_{SE}

are inversely proportional to the concentration of surfactant, C_{SE} is directly proportional to the square root of this concentration, and C_M is independent of this concentration. A plot of the reciprocal decay constant for two different surfactants appears in Figure 5.12 as a function of the conductivity of the two solutions. The coincidence of the data suggests that the Ohmic resistance of the solution is the primary resistive contributor to the relaxation time after an on/off transition.

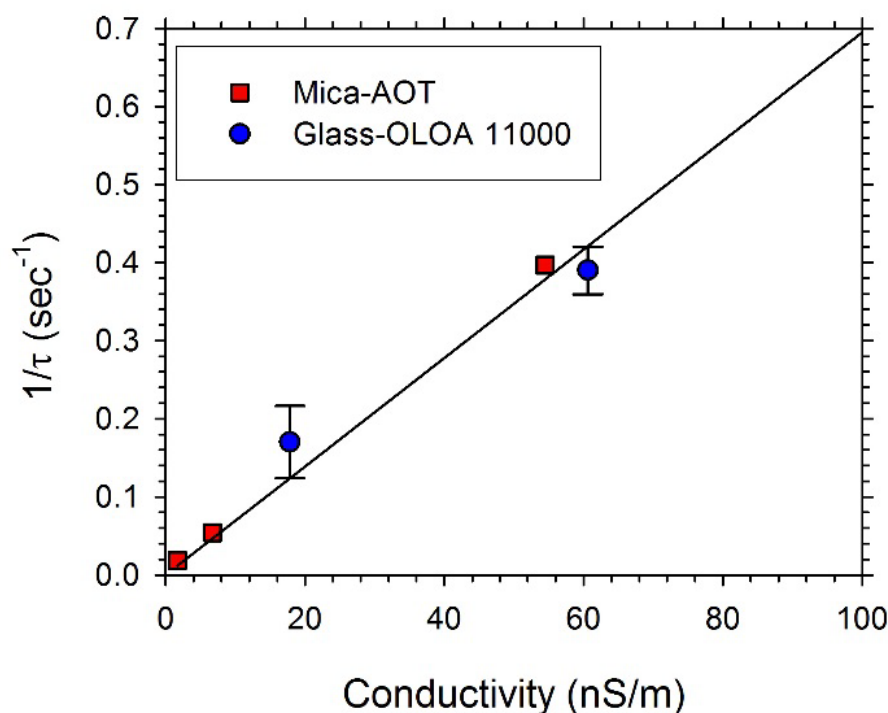


Figure 5.12. This plot compiles the time constants for different concentrations of Mica in AOT-dodecane solutions and glass in OLOA 11000-dodecane solutions. The straight line was fit to the data and has a slope of $7.0 \times 10^6 \Omega\text{m/sec}$.

5.4.3 Zeta potential of silica particles and fused silica

The measured streaming potential values found from the rotation “on” and “off” steady-state potentials was converted to zeta potentials for a fused silica surface in solutions of dodecane with various concentrations of OLOA 11000®

using equation (5.1). The measured zeta potentials appear in Figure 5.13 as a function of the zeta potential of silica particles determined from electrophoretic mobility measurements on a Malvern ZetaSizer Nano. The zeta potential was calculated from the mobility measurements using Henry's law and the Debye lengths for OLOA 11000[®] in dodecane previously measured with impedance spectroscopy.[22] The near linear relationship suggests agreement in the sign and magnitude of the zeta potential between the macroscopic surface measurements and the particle electrophoresis measurements. Additionally, the negative zeta potentials of the fused silica surface also agree with published measurements of silica particles in Isopar-L doped with OLOA 11000. [13, 15]

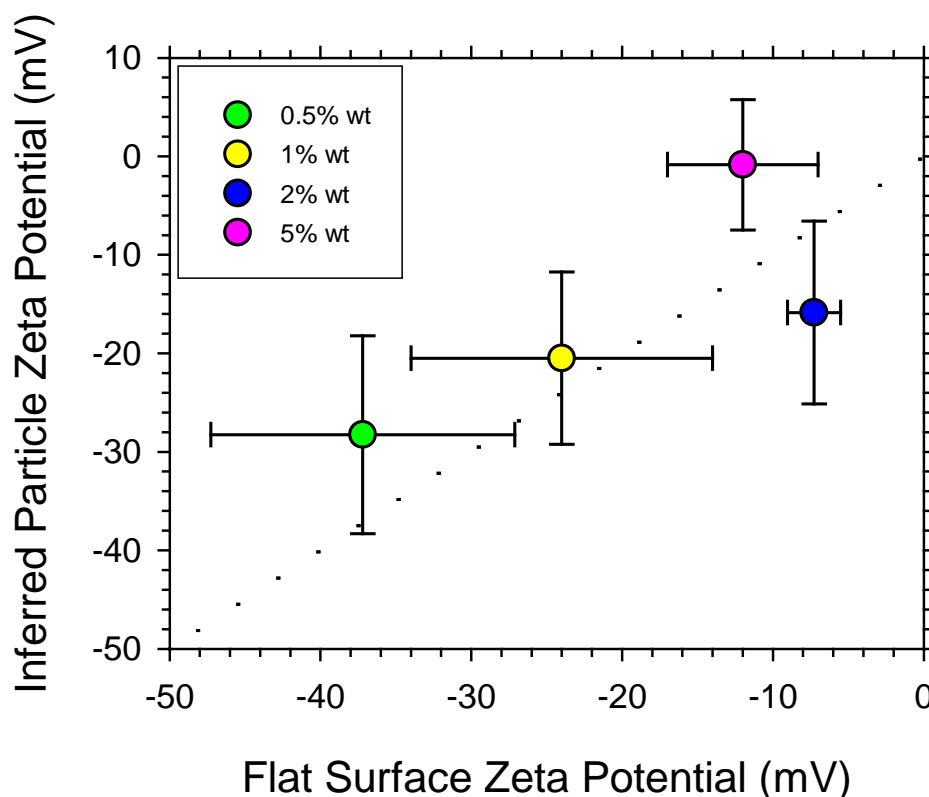


Figure 5.13. The flat surface zeta potential measurements for silica is plotted on the x axis versus the inferred particle zeta potential found from electrophoresis and converting using Henry's law. The different colors represent different concentrations of OLOA 11000.

5.4.4 Zeta potentials of tested samples and surfactants

Having established that the apparatus and method are yielding the streaming potential that is intended in equation (5.1) and in agreement with particle mobility measurements of similar surfaces, we determined the zeta potentials of a surface of glass coated with a conductive layer of Indium Tin Oxide (ITO). Figure 5.14 contains the measured zeta potentials of ITO in dodecane with different concentrations of Span 20[®] and OLOA 11000. The findings show that OLOA 11000[®] produces a weak negative charge on the ITO surface, while Span 20[®]

gives a weak positive charge. The actual values of the measured zeta potentials are shown in Table 5.1. The low magnitudes of the zeta potential of the ITO surface confirm the accuracy of previously made assumptions of small zeta potentials less than the thermal voltage ($< 25\text{mV}$) on ITO coated glass slides in order to calculate the double layer capacitance of surfactant doped dodecane solutions.[22, 23]

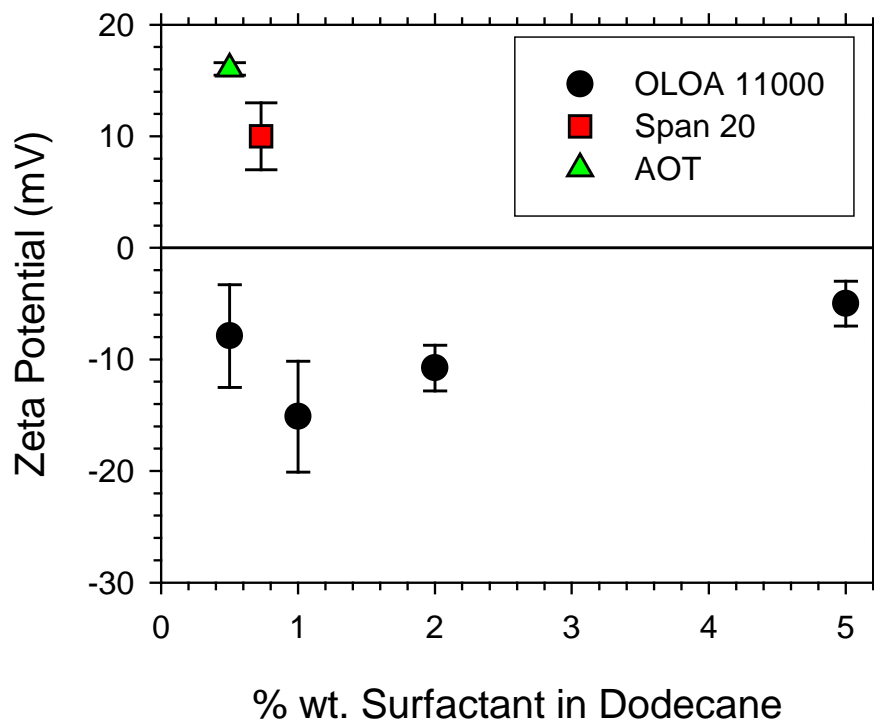


Figure 5.14. Zeta potential of glass coated with a conductive ITO layer in solutions of OLOA 11000[®] (black circles), Span (red squares), and AOT[®] (green triangles) in dodecane.

Table 5.1. Zeta potential of ITO coated glass surface in dodecane doped with different surfactants

Surfactant	Concentration	Zeta Potential
OLOA 11000	0.5%	-8 ± 5
OLOA 11000	1%	-15 ± 5
OLOA 11000	2%	-11 ± 2
OLOA 11000	5%-	-5 ± 2
Span 20	0.73%	10 ± 3
AOT	0.5%	16.0 ± 0.6

5.5 Conclusions

We conclude from this investigation that determination of the zeta potential of macroscopic samples in nonpolar liquids is possible on the basis of a streaming potential measurement. The rotating disk approach is advantageous for these measurements because it is essentially immune to surface conductivity. The crucial elements of the approach that distinguish it from experiments in aqueous environments are the use of glassy carbon electrodes as sensors and an electrometer as the voltage measuring device. The measured voltage undergoes transitions on the time scale of seconds when the rotation is switched on and off. Analysis and experiments indicated that the timescale of the transition reflected the charging of the electrometer's input capacitance through the Ohmic resistance

to flow of the very small sensing current to the glassy carbon sensors, which explained the shape of the curves.

5.6 Acknowledgement

The authors gratefully acknowledge a grant from Dow Chemical Corporation in support of this investigation. The authors would also like to thank the work of Xi Chen for performing many of the zeta potential measurements of the fused silica surface.

5.7 References

1. Hunter, R.J., *Foundations of Colloid Science*. Vol. 1. 1987, Oxford: Clarendon Press.
2. Delgado, A.V., et al., *Measurement and interpretation of electrokinetic phenomena*. Journal of Colloid and Interface Science, 2007. **309**: p. 194-224.
3. O'Brien, R.W. and L.R. White, *Electrophoretic Mobility of a Spherical Colloidal Particle*. Journal of the Chemical Society, Faraday Transactions 2: Molecular and Chemical Physics 1978. **74**: p. 1607-1626.
4. Sides, P.J., et al., Calculation of the Streaming Potential near a Rotating Disk. Langmuir, 2006. **22**: p. 9765-9769.
5. Sides, P.J. and D.C. Prieve, Surface Conductivity and the Streaming Potential near a Rotating Disk-Shaped Sample. 2013. **29**: p. 13427-13432.
6. Hoggard, J.D., P.J. Sides, and D.C. Prieve, Measurement of the Streaming Potential and Streaming Current near a Rotating Disk to Determine Its Zeta Potential. Langmuir, 2005. **21**: p. 7433-7438.
7. Prieve, D.C. and P.J. Sides, *Streaming Potential near a Rotating Porous Disk*. Langmuir, 2014. **30**: p. 11197-11203.

8. Parreira, H.C., Electrophoresis of Carbon Black in Liquids in Liquids of Low Dielectric Coefficient. Effect of the Metallic Element of the Adsorbate. *Journal of Electroanalytical Chemistry*, 1970. **25**: p. 69-78.
9. Morrison, I.D., *Electrical charges in nonaqueous media*. Colloids and Surfaces A: Physicochemical and Engineering Aspects, 1993. **71**: p. 1-37.
10. Lyklema, J., *Principles of interactions in non-aqueous electrolyte solutions*. *Current Opinion in Colloid & Interface Science*, 2013. **18**: p. 116-128.
11. Gacek, M., G. Brooks, and J.C. Berg, *Characterization of Mineral Oxide Charging in Apolar Media*. *Langmuir*, 2012. **28**: p. 3032-3036.
12. Gacek, M.M. and J.C. Berg, Effect of surfactant hydrophile-lipophile balance (HLB) value on mineral oxide charging in apolar media. *J Colloid Interface Sci*, 2015. **449**: p. 192-197.
13. Gacek, M.M. and J.C. Berg, Investigation of Surfactant Mediated Acid-Base Charging of Mineral Oxide Particles Dispersed in Apolar Systems. *Langmuir*, 2012. **28**: p. 17841-17845.
14. Gacek, M.M. and J.C. Berg, *The role of acid-base effects on particle charging in apolar media*. *Advances in Colloid and Interface Science*, 2015. **220**: p. 108-123.
15. Poovarodom, S. and J.C. Berg, Effect of particle and surfactant acid-base properties on charging of colloids in apolar media. *J Colloid Interface Sci*, 2010. **346**(2): p. 370-7.
16. Espinosa, C.E., et al., Particle charging and charge screening in nonpolar dispersions with nonionic surfactants. *Langmuir*, 2010. **26**(22): p. 16941-8.
17. Lee, J., et al., Mechanisms of Particle Charging by Surfactants in Nonpolar Dispersions. *Langmuir*, 2015. **31**: p. 11989-11999.
18. Guo, Q., et al., *Surfactant mediated charging of polymer particles in a nonpolar liquid*. *Journal of Colloid and Interface Science*, 2013. **392**: p. 83-89.
19. Kitahara, A., S. Karasawa, and H. Yamada, *The Effect of Water on Electrokinetic Potential and Stability of Suspensions in Nonpolar Media*. *Journal of Electroanalytical Chemistry*, 1967. **25**: p. 490-495.

20. Kitahara, A., et al., The concentration effect of surfactants on zeta-potential in non-aqueous dispersions. *Colloid and Polymer Science*, 1977. **255**(11): p. 1118-1121.
21. Kitahara, A., T. Fujii, and S. Katano, Dependence of Zeta-Potential upon Particle Size and Capillary radius at Streaming Potential Study in Nonaqueous Media. *Bulletin of the Chemical Society of Japan*, 1971. **44**: p. 3242-3245.
22. Yezer, B.A., et al., Use of electrochemical impedance spectroscopy to determine double-layer capacitance in doped nonpolar liquids. *Journal of Colloid and Interface Science*, 2015. **449**: p. 2-12.
23. Yezer, B.A., et al., Determination of charge carrier concentration in doped nonpolar liquids by impedance spectroscopy in the presence of charge adsorption. *Journal of Colloid and Interface Science*, 2016. **469**: p. 325-337.

Chapter 6 Conclusions and future directions

6.1 Conclusions

Since the 1950's the nature of charges in nonpolar liquids with surfactants has been an active research area.[1, 2] The development of new display applications has recently promoted work focused on electrostatically stabilizing particles in nonpolar liquids.[3] The mechanisms controlling the formation of charge in solution and how charge is acquired by solid surfaces must be understood to design stable suspensions. Many gaps still exist in this field concerning the origin of the charged species, the size of the charge carriers, and symmetry of the charge carriers in solution. Additionally the interactions of surfactants at surfaces give rise to surface charge, but the mechanisms of the interactions leading to charge seem to differ on a case by case basis.[4-6]. The work presented in the previous chapters provides simple experimental techniques for the characterization of charge in solution and at surfaces. Additionally, the measurements presented in this thesis obtained from impedance spectroscopy and streaming potential measurements have resulted in insights on the behavior of charges in nonpolar liquids. These techniques can be applied generally in future work to study any number of surfactant structures, solvents, and surface chemistries.

In chapter 2 the diffusivity of charge carriers was inferred by independently measuring the conductivity and Debye length of OLOA 11000 in dodecane with impedance spectroscopy. The size of the charge carriers was found to be larger than the average micelle size measured with phase analysis light scattering. This observation is in agreement with conclusions made in other studies that independently measure the Debye length.[7] Previously, researchers have neglected to measure the Debye length and assumed that the charge carrier diffusivity is equal to the micelle diffusivity [8-10] which results in an overestimate of the diffusivity of charge carriers and an underestimate in the charge carrier concentration. The largest micelles in solution have a higher probability of sequestering a charge.

The use of impedance spectroscopy to characterize charge is expanded in chapter 3 by measuring the impedance of Span 85, Span 80, and Span 20 in dodecane. The impedance at low frequency suggests that all three solutions showed evidence of charge adsorption and desorption at the electrode-liquid interface. The adsorption model used to fit the impedance measurements also qualitatively predicts the long-lived current shown in the literature [11, 12] to arise in response to a constant applied DC voltage bias across a similar fluid cell with solutions of the same surfactants in dodecane.

The charge adsorption phenomena may be important in understanding the origins of surface charge. Many questions concerning the appropriate model for

charge adsorption remain that can be further studied in future work. Possible future directions include a systematic study of the adsorbed layer of surfactant surfaces in nonpolar liquids. Additionally changes in this adsorbed layer in response to an applied field may be used to identify how charges are carried to and from surfaces. The charge adsorption model used in chapter 3 also assumes that the kinetic parameters for adsorption and desorption are equal for both positive and negative charge. This assumption can be tested by fabricating an insulating film on one of the electrodes and apply a DC voltage to the fluid cell. The insulating film should hinder charge adsorption at that electrode, while adsorption and desorption occurs on the bare electrode. Differences between the sign of the applied charge and the measured “long lived” current response of the cell would indicate that the adsorption and desorption kinetics are not equal for charges of opposite sign.

Additionally, the charge adsorption phenomena described in chapter 3 can cause problems with the measurements of Debye length. The impedance response of a solution becomes “diffusion limited” if the rate of charge adsorption of a particular surfactant solution is fast compared to the diffusion rate of the charge carriers across the length of the fluid cell. When charge diffusion is limited compared to surface adsorption the double capacitance of the cell cannot be observed in the impedance response. In order to properly measure the Debye length of a solution the cell must be “adsorption limited” and the rate of charge

diffusion across the cell must be greater than the rate of charge adsorption. This problem may be overcome in future work by coating the ITO electrodes with a thin insulating film to decrease the rate of charge absorption.

Further insights into the nature of charge formation are presented in chapter 4. The relation between the charge carriers in a micelle solution and the size of the micelles was found with impedance spectroscopy and phase analysis light scattering for commonly used surfactants AOT[®], OLOA 11000[®], Span 85[®], Span 80[®], and Span 20[®]. An exponential relationship was found between the molar conductivity of the solution and the estimated diameter of the polar core of the micelles. The diameter of the polar core of the micelles was estimated using the tail lengths of the surfactants. Additionally the ratio of the charge concentration to the surfactant concentration for a particular surfactant also increases exponentially with the diameter of the polar core of the micelles. The charge fluctuation model used to describe the conductivity of micro-emulsion droplets accurately predicted the observed result that diameter of the polar core of the micelle is the most important factor in increasing the conductivity of nonpolar liquids. The relationship between micelle size and charge concentration observed in chapter 4 suggests that the surfactant structure surprisingly has no effect on the charge concentration other than the effects of the structure on micelle size.

There are many opportunities to further understand and test the relationship between micelle size and charge carrier concentration in nonpolar liquids. The

effects of water content on micelle size and charge concentration should also follow the charge fluctuation model and can be varied systematically. Additionally, the observed relationship can be tested with other oil-soluble surfactants and different nonpolar solvents. An ideal project would be to measure the conductivity and charge concentration of a homologous series of surfactants varying slightly in either head group or tail group structure and observe if surfactant structures have any effect on the properties of charge carriers other than by affecting the size and shape of micelle. The estimation of the size of the micelle polar core can also be measured much more accurately with the use of X-ray scattering rather than light scattering.

Chapter 5 introduces a method to determine the zeta potential of macroscopic samples in nonpolar liquids by measuring the streaming potential arising next to a rotating disk. This method may be used in future experiments to provide insight to the mechanisms that determine surface charge in nonpolar liquids. The flat disk geometry is ideal for studying a homologous series of surfaces with varying chemical functionality and observing how surface properties effect the zeta potential in surfactant doped nonpolar liquids. Ultimately, the methods and insights presented in this thesis can be used to improve the understanding of the nature of charge in nonpolar liquids.

6.2 References

1. Electrostatics in the Petroleum Industry: The Prevention of Explosion Hazards. . 1958: Elsevier.
2. Dukhin, A.S., Properties of electrolytic solutions: Dissociation, fluctuation and disproportionation models for ionization of surfactant solutions in low- and non-polar liquids. JCIS manuscript, 2012.
3. Parent, M.E., et al., Influence of surfactant structure on reverse micelle size and charge for nonpolar electrophoretic inks. *Langmuir*, 2011. 27(19): p. 11845-51.
4. Gacek, M.M. and J.C. Berg, The role of acid-base effects on particle charging in apolar media. *Advances in Colloid and Interface Science*, 2015. 220: p. 108-123.
5. Lee, J., et al., Mechanisms of Particle Charging by Surfactants in Nonpolar Dispersions. *Langmuir*, 2015. 31: p. 11989-11999.
6. Electrical Phenomena at Interfaces: Fundamentals, Measurements, and Applications. Surfactant Science Series, ed. M.J. Schick and F.M. Fowkes. 1984, New York, NY: Marcel Dekker.
7. Prieve, D.C., et al., Two Independent Measurements of Debye Lengths in Doped Nonpolar Liquids. *Langmuir* 2008. 24: p. 1120-1132.
8. Guo, Q., V. Singh, and S.H. Behrens, Electric charging in nonpolar liquids because of nonionizable surfactants. *Langmuir*, 2010. 26(5): p. 3203-7.
9. Gacek, M., et al., Effects of trace water on charging of silica particles dispersed in a nonpolar medium. *Langmuir*, 2012. 28(31): p. 11633-8.
10. Schmidt, J., et al., Conductivity in nonpolar media: experimental and numerical studies on sodium AOT-hexadecane, lecithin-hexadecane and aluminum(III)-3,5-diisopropyl salicylate-hexadecane systems. *J Colloid Interface Sci*, 2012. 386(1): p. 240-51.
11. Strubbe, F., et al., Generation current of charged micelles in nonaqueous liquids: measurements and simulations. *Journal of Colloid and Interface Science*, 2006. 300(1): p. 396-403.

12. Beunis, F., et al., Electric charging of inverse micelles in a nonpolar liquid with surfactant. *Colloids and Surfaces A: Physicochemical and Engineering Aspects*, 2014. 440: p. 10-19.